TIME-DOMAIN NUMERICAL SIMULATION OF THE MOTION OF SMALL FLOATING BODIES DRIFTING IN WAVES

MOMEN ABDEL-MAGID WISHAHY

TIME-DOMAIN NUMERICAL SIMULATION OF THE MOTION OF SMALL FLOATING BODIES DRIFTING IN WAVES

by

Momen Abdel-Magid Wishahy, B.Sc.(Hon.), M.Eng.

A thesis submitted to the School of Graduate Studies in
partial fulfillment of the requirements for the degree of

Doctor of Philosophy

Faculty of Engineering and Applied Science
Memorial University of Newfoundland

May, 1988

ABSTRACT

Theoretical and experimental investigations have been conducted to examine the behaviour of small icebergs and bergy bits in unidirectional regular waves. A nonlinear time-domain method based on the equivalent motion concept and a corresponding computational algorithm are presented for predicting the motion and trajectory of small ice masses drifting in an open seaway and near a gravity base platform. The general equations of motion of a rigid body are applied, and the wave forces are determined as the sum of the resultant of wave-induced pressures integrated over the instantaneous wetted surface of the body (the Froude-Krylov forces) and the flow disturbance induced by the presence of the body as determined by the equivalent motion method. The algorithm is used to predict the motion and trajectories of free drifting and towed spherical models in small and large amplitude waves. The computed values are found to be in good qualitative and quantitative agreement with the experimental measurements outside the heave resonance range where the motions are over-predicted. The motions of the ice mass are also simulated near a cylindrical gravity platform taking into account the effect of the waves diffracted by the structure. Large heave motions are predicted in close vicinity of the platform. In addition to instances where collisions were predicted, the ice drifted around or maintained a stationary position in front of the structure. It is concluded that the method can be applied to provide predictions of the kinematic parameters of motion of small bodies drifting in waves.

To God

and

To my family

ACKNOWLEDGEMENTS

I would like to express my sincere gratitude to my supervisory committee: Dr. D. B. Muggeridge, who has given me continuous help, encouragement and inspiring guidance throughout the project; Dr. J. S. Pawlowski, who has strongly influenced my work by his novel ideas, constant guidance and motivating personality; and to Dr. J. H. Lever, for his helpful suggestions, discussion and enthusiastic support.

I gratefully acknowledge the support of Dr. G.R. Peters, Dean of the Faculty of Engineering and Applied Science, and Dr. F.A. Aldrich, former Dean of the School of Graduate Studies, and the partial financial support offered by Memorial University of Newfoundland throughout my Ph.D. program.

The study was carried out as a part of the Institute for Marine Dynamics (IMD), National Research Council of Canada, and NORDCO Limited research programs. In this connection, I would like to thank Mr. N. Jeffrey, Director, Mr. D.G. Murdey, Assistant Director, and J.S. Pawlowski, Leader of the Offshore Research Group, all of IMD, for their sustained interest and support. Similar thanks are due the

management of NORDCO Limited especially Mr. F. Smith, President.

Thanks are due to many others who have helped during the project: Mr. B. Gamberg and Mr. K. Jones, both from IMD, for their assistance in the use of the computer; Ms. J. Tillotson and Mrs. A. Sanger from the CISTI Library; Mr. W. Carroll from NORDCO Limited for his assistance in the experimental program; and Mrs. M. Brown of the Ocean Engineering Research Group at Memorial University for careful typing of the thesis.

Finally, I would like to express my deep gratitude to my family, who patiently tolerated the ups and downs of a research student during the course of his work, for their continued support and encouragement throughout all these years.

TABLE OF CONTENTS

LIST OF TABLES

LIST OF FIGURES

1.0 INTRODUCTION

The discovery of the Hibernia oil field has increased navigation and offshore operations in the ice infested waters off the east coast of Newfoundland. Ships and offshore platforms are increasingly exposed to hazards of potential collisions with growlers, bergy bits (10-10^3 tonnes) and small icebergs (10^4-10^5 tonnes). Such small ice masses are hard to detect in stormy weather conditions; besides, they may attain high kinetic energy in response to large waves, which may lead to the possibility of severe structural damage resulting from a collision. In the vicinity of a large structure, the incident wave train is disturbed by the presence of the structure which affects the wave exciting forces acting on a drifting ice mass. In some cases, the iceberg stops before or deflects around the structure and no impact occurs. In other cases, the impact speed is varied from that of the open water condition. Therefore, knowledge of the kinematics of small (in comparison with wave length) ice masses in an open seaway and near offshore structures is necessary as an input to the design process.

In this dissertation, a nonlinear three-dimensional time-domain method is developed to predict the motions and trajectories of small ice masses of arbitrary shapes in response to regular waves of small and large steepness, in an open seaway and in proximity of offshore structures. Therein, the wave-induced (Froude-Krylov) forces are obtained by a direct integration of the pressures over the instantaneous submerged body surface. The scattering forces due to the disturbance of the wave flow by the presence of the body are estimated by the equivalent motion concept. Viscous forces are evaluated by the application of appropriate semi-empirical drag coefficients in conjunction with the equivalent motion velocity.

1.1 Literature Review

Estimation of the motion of ice masses drifting in open waters and in close vicinity to offshore structures has received limited attention. Literature on the response of stationary floating bodies to wave action is voluminous and has been reviewed extensively by Wehausen (1971), Hogben (1974), Garrison (1978), Mei (1978, 1983), Isaacson (1979), Sarpkaya and Isaacson (1981) and Yeung (1982). On the other hand, methods to predict the instantaneous iceberg velocity, resulting from the oscillatory as well as the drifting motion, are scarce. The validity of such models for predicting the motion of small ice masses in waves will be discussed. In addition, several special topics in hydrodynamics such as wave nonlinearity and viscous effect, large body motions, hydrodynamic forces on shallowly submerged bodies, complex body geometry, interference effects between bodies floating in near proximity, etc. pertain to the problem owing to its complexity. Hence, I will briefly outline some of these topics to furnish a general scope of the overall problem.

1.1.1 Long-Term Drift Models in Open Seaway

Models to describe the long term drift motion of icebergs (over periods of tens of hours) can broadly be classified as kinematic, dynamic or statistical models depending on the approach to the problem.

Kinematic models assume a linear relationship between the ice mass velocity and the strengths of the environmental factors such as winds and currents, e.g. Dempster (1974) and Cheema and Ahuja (1978). The actual forces imposed on the ice mass are ignored. Accordingly, the practical application of these models in examining the motion under wave actions of various ice mass sizes is limited.

Dynamic models predict iceberg trajectories (in the horizontal) by estimating the environmental forces on the ice mass and integrating the equation of motion. Forces resulting from the action of uniform and non-uniform currents, wind and added mass effects, as well as the Coriolis force and related to it effects of the pressure gradient due to sea surface slope are included in models proposed by Sodhi and El-Tahan (1980), El-Tahan (1980), Mountain (1980) and Smith and Banke (1981, 1982). The effect of wave drift forces, in addition to other environmental loads, on the trajectory is considered in the model developed by Hsiung and Aboul-Azm (1982) and Aboul-Azm (1982). They used linear diffraction theory to derive the average horizontal wave drift forces, ignoring the effect of the instantaneous oscillatory motions. Trajectory predictions using the dynamic approach is limited by the accuracy in finding the input data for wind, current and wave conditions and for the iceberg parameters such as underwater shape and added mass and drag coefficients.

Garrett (1984) developed a statistical model using the past iceberg position and velocity data to predict the future trajectory. Gaskill and Rochester (1984) estimated the input data to a dynamic model from the previous history of a berg's drift.

Long term drift prediction models have useful applications in warning drilling ships and platforms of approaching icebergs, thus allowing enough time for taking precautionary actions to prevent collisions. However, these models cannot be directly applied to predict the instantaneous velocity of small ice masses in waves for the apparent reason of neglecting the effect of waves altogether or at least ignoring the wave-induced oscillatory motions of the icebergs.

1.1.2 Drift Models Near A Structure

Very little work has been done on the motion of icebergs drifting in the vicinity of a structure. NORDCO Limited (1985) investigated the hydrodynamic interaction of an iceberg with a gravity based offshore structure. The wave-induced oscillatory motion of icebergs in an open seaway and near a gravity based cylindrical structure was predicted using linear diffraction theory. The structure-iceberg interaction effect was accounted for by assuming the total velocity potential to be a linear superposition of the incident potential, the diffracted and radiated potentials due to the iceberg and the diffracted potential due to the structure. It should be noted that the flow disturbances induced by the iceberg as well as those induced by the structure were estimated for an open seaway condition, i.e. independently of each other. The solution of the boundary integral equations was based on a three dimensional source technique using Green's function. Experiments were conducted at the Memorial University wave tank using a Froude scale of 1:100. The motions of four model tabular icebergs, weighed 460, 230, 130 and 115 thousand tonnes in full scale, were measured in regular waves. At model scale the water depth was 80 cm. The gravity based structure was modelled by a cylinder which was 114 cm in diameter and 100 cm high. The motions of the iceberg models were recorded using a SELSPOT system and video cameras while load cells were used to measure the impact forces on the fixed structure. It was concluded that the iceberg motions in surge, heave and pitch did not change at small separation distances in the range of 1.0 to 0.25 m from the structure. Meanwhile, both surge and heave motions of the model in close proximity of the structure were less than those observed in open water condition.

A short term (over trajectories of hundreds of meters) model of iceberg drift, which includes wave induced motions and the influence of the presence of a large fixed structure, has been developed by Isaacson (1985, 1986a,b,c) and Hay and Company Consultants Inc. (1986). In this model, the drift motion expressed by linear displacements (surge and sway) in the horizontal plane, is induced by the current and wave drift forces. The effects of wind, Coriolis force and sea-surface slope are ignored. The nonlinear interaction terms are assumed sufficiently small so that the wave and current fields are each treated separately. Moreover, the oscillatory motions of the ice mass and thus wave radiation are assumed to be not influenced by the superposed mean drift. Therefore, the problem of wave-induced oscillatory motions is treated by considering the ice mass to have a fixed equilibrium position for any one computation, and the added mass and damping characteristics of the iceberg are obtained by solving the linearized, stationary, two body diffraction problem in the frequency domain. The viscous damping coefficients are taken to be zero except for the heave, roll and pitch modes where the viscous effects are included through the use of empirical coefficients. Likewise, the wave drift forces are calculated using the mean, rather than the total (mean plus oscillatory) ice mass velocities. Nevertheless, the added mass effect and the disturbance of the uniform current velocity field by the fixed structure are included, both by means of linear diffraction theory. The drift trajectory is then solved by a time stepping procedure applied to the drift equations of motion which involve zero frequency added mass and drag forces both of which are independent of wave induced oscillatory motions of the ice mass. Wave-induced oscillatory motions in the six degrees of freedom are derived at a series of points along the drift trajectory, and the total iceberg response is determined by a linear superposition of the drift and oscillatory motions.

This approach is most suitable for application in the range of wave length to ice mass diameter λ/D between approximately 5 and 0.5, where wave diffraction and radiation by the iceberg are significant, providing the waves are of small steepness and therefore the amplitudes of motions of the ice mass are relatively small. From a practical point of view, the ice mass within this range can be classified as either a medium or a large iceberg. For very large icebergs, corresponding to a ratio λ/D less than 0.5, the ice mass oscillatory motions become negligible. Nevertheless, the wave drift forces can still be computed using the prescribed method. However, for smaller ice masses having a ratio of λ/D greater than 5, in steep waves, the linear diffraction theory is expected to yield poor agreement with the experimental results for the reasons stated below. Also treating the drift and oscillatory motions independent of each other may lead to significant errors in the estimation of the actual ice mass kinetic energy.

The application of linear diffraction theory to the evaluation of wave-induced oscillatory motions of ice masses necessitates the assumption of small motion amplitudes with respect to the characteristic dimensions of the body and small wave steepness. Such assumptions cannot be adopted for a wide range of practically important situations especially when growlers, bergy bits and small icebergs are driven by large waves. Under these conditions, the ice masses exhibit large motions thus violating the two assumptions. Furthermore, the theory overpredicts the heave, pitch and roll motions near the resonance range due to neglect of viscous and nonlinear interaction forces. Moreover, small ice masses tend to have round or spherical and conical shapes due to melting which result in large changes in the heave restoring forces corresponding to large amplitude of motion. The motion of such sloping side shapes are extremely nonlinear as reported by Andersson et al. (1986) in connection with the experimental findings of the behaviour of truncated cones shape and by Lever et al. (1988) for trapezoid and spherical models even within the range of small steepness (H/λ = 1/63 to 1/46) where H represents the wave height.

1.1.3 Wave-Induced Motion of Small Ice Masses

A qualitative analysis of the maximum instantaneous surge and drift velocities attained by ice masses in regular waves and regular wave groups was performed by Murray et al. (1983). They conducted laboratory experiments to determine the maximum wave-induced velocity of cylindrical, spherical and cubical models using a range of model beam to wave length ratios of .11 to .53 and wave slopes of less than 0.02. They concluded that in regular waves the models reached steady-state velocities approximately equal to the maximum wave particle velocities for model length to wave length ratios of less than 0.33.

Lever et al. (1984) also used a 54.74 m long, 4.57 m wide wave tank at Memorial University of Newfoundland to examine the wave-induced motion of small icebergs and bergy bits in storm waves typical of the Grand Banks region. The model tests covered the range of full scale masses from 10-10^5 tonnes. The models used were cubical, prismatic and spherical to represent different types of iceberg shapes. They concluded that for ratios of wave length to characteristic ice size, λ/D, greater than approximately 13, the models behaved essentially as particles of the fluid.

For 10 $\leq \lambda/D \leq$ 13, ice model shape had an influence on whether particle-like motion occurred. For $\lambda/D \leq$ 10, no ice models moved as a fluid particle. Bergy bits and small icebergs in storm waves could attain energies in the order of 10^6 - 10^9 joules.

McTaggart and Davenport (1984) conducted experiments of wind-induced iceberg drift in a wind/wave tank. Experimental results were used to evaluate the performance of a 1-dimensional numerical iceberg drift model. Forces contributing to iceberg drift were due to wind, wind-induced water currents and wind generated waves. They concluded that a purely deterministic numerical model was inadequate to describe the motions of model icebergs, even under idealized conditions. A high degree of variability among model iceberg drift paths was observed.

Salvalaggio and Rojansky (1986) conducted laboratory experiments in a wave tank, 7.3 m long by 4.3 m wide, to simulate the impact of different wave driven icebergs with a fixed caisson type structure. A numerical model for calculating impacts with different eccentricities was developed and used as the basis for a reliability evaluation. Environmental conditions similar to those prevailing on the Grand Banks were modelled. The tests covered the range of full scale wave periods from 10.2 to 20 seconds in 80 m water depth and 13.5 m wave height. Three cylindrical iceberg masses of 8 X 10^3 to 10^6 tonnes and two structures of 55 and 100 m in diameter were modelled using 1:287 scale. They concluded that, based on the laboratory observations, the wave driven icebergs may not impact a fixed caisson if the bergs were smaller than half the structure diameter. The validity of such a finding, in my opinion, is a little dubious for the following reasons: 1) the scale of the experiments was very small (1:287); 2) influence of wave heights was not included; 3) last and foremost the wave reflection from the beach and side walls in such a relatively short tank may have significant influence on the motion of the small ice masses.

Model tests have been carried out to study the risk for impacts from bergy bits to various sections of a semisubmersible by Andersson et al. (1986). In the first test series, the rig was moored with a conventional eight point all chain mooring system and towed to produce the current that drifts the bergy bits. Bergy bits were modelled by two joined truncated cones giving a hexagonal profile. Three different sizes of bergy bits having 1:50 scale and weighing 100, 500 and 1000 tonnes respectively at full scale, were tested in three different wave spectra. They observed that small growlers hit critical structural members in relatively small seas. The bracing induced more collisions by directing the growlers towards the columns. The bergy bits can be trapped and remain close to one column for some time. The second set of tests was carried out to study the motion of spherical and hexagonal ice masses in regular and irregular seas. The recorded motions of the icebergs in irregular waves were very irregular and did not follow any linear behaviour. Thus, they recommended a special consideration has to be paid to the strong nonlinear effects when mathematically describing the motions of bergy bits. In regular waves, again the motions were extremely nonlinear about the natural heave period. However, linear diffraction theory was applied to calculate the transfer functions of the ice masses with an approximation to the maximum vertical response at resonance frequencies. A qualitative assessment was made that the response amplification operator, RAO, in heave had a maximum value of 2. Comparison between the measured and calculated heave responses showed very poor agreement for both models in 1/30 and 1/20 wave steepness conditions which once more reflects the limitations of application of the linear diffraction theory. Assessments of the risk of impact and risk of structural damage were performed in ice conditions of masses up to 15000 tonnes and current velocity up to 1 m/sec. They concluded that conventional semisubmersibles were not suitable as the bracing structures were very sensitive to ice impacts. They also recommended that the columns, as well as the pontoons, should be adequately strengthened to the same level to safely resist bergy bit impacts.

Kobayashi and Frankenstein (1986 and 1987) reviewed previous studies on wave and ice interaction. The iceberg motions and mean wave drift forces were computed using linear diffraction theory. The available experimental data from Lever et al. (1984) were compared with the theoretical results and with the fluid particle motion. Large scattering of the data points relative to the theoretical curves was observed in the surge mode as well as in the heave direction especially at resonance.

Arunachalam et al. (1987) presented a theoretical and experimental study for the estimation of the first order wave-induced motions in surge and heave of a free floating iceberg in a regular wave field. The theoretical model was based on the linear diffraction theory employing a three-dimensional source distribution technique. The motions of two model icebergs, a cylinder with a diameter of 0.2 m and length of 0.2 m and a cube with sides of 0.2 m, were monitored by rotary potentiometers by means of a cable attached through their centres of gravity. The tests were carried out in the Memorial University wave tank at a water depth of 1.8 m, and the wave period ranged between 0.8 sec to 1.8 sec. Wave heights were varied from 2.7 cm to 5.2 cm. It was concluded that the computed results of the oscillatory motion of the icebergs in the surge mode agreed well with the measured values within the limits of experimental error. However, in the heave direction the agreement was only satisfactory. It was also indicated that the surge velocity of a model iceberg with a draft to water depth ratio of less than 0.1 can be greater than 0.8 times the water particle velocity when the iceberg horizontal dimension is less than 0.3 times the wave length. However, as the horizontal dimensions of the iceberg and draft to depth ratio were increased, the model iceberg no longer behaved like a water particle.

Recently, Lever et al. (1988) studied theoretically and experimentally the influence of the shape on the wave-induced motions of small icebergs and the applicability of predicting the iceberg motion in irregular seas from the product of linear response amplitude operators (RAOs) and the wave energy spectrum. The linear diffraction theory was used to compute the iceberg response. The shape of icebergs was modelled by cubes, a cylinder, a trapezoid and a sphere.

The motion of the models was measured in regular wave conditions of steepness $H/\lambda = 1/63$ to $1/46$ as well as in irregular waves. The models exhibited nonlinear behaviour in high seas, and a large variation between the predicted and measured motions was observed, especially in heave. The differences tended to be larger for the sloped side models, the trapezoid and the sphere. It was inferred that the trapezoidal and spherical models did not resonate in heave in the investigated steepness range and they were inclined to have lower RAO asymptotes for large steepness. It should be noted that a similar trend was observed from the experimental findings of the present investigation. Lever et al. concluded that the ice mass shape has a significant influence on the wave-induced motion in regular waves and that the linear theory is expected to yield poor agreement as wave steepness increases.

1.1.4 Special Topics

The problem of predicting the response of small ice masses to wave excitations, due to its intricacy, encompasses several perplexing subjects of a hydrodynamic nature. It is beyond the scope of the present review to describe the state of the art of such subjects but rather to highlight the difficulties surrounding the development of a general solution to the aforementioned problem. A review of the hydrodynamic forces on shallowly submerged bodies in waves will be followed by a review of the force due to viscous drag.

Small icebergs and bergy bits tend to have a small freeboard due to their shape and relatively high density. In response to the action of some steep waves they fully submerge. For a submerged body oscillating close to the free surface, the free-surface effect can significantly influence the added mass and wave-damping coefficient values as a function of the frequency and the direction of the oscillations. Several, but rather limited, theoretical and experimental investigations have been conducted to determine the forces on shallowly submerged bodies. The cylindrical shape has received special attention because of the frequent occurrence of such geometry in offshore structures. Chung (1977) studied experimentally the forces on submerged square and circular cross section cylinders oscillating near a free surface and compared the measured results with computations by a potential theory using Frank's (1967) approach. Comparisons of the experimental results with the computations showed reasonably good agreement. However, the measured coefficient values for the sway and heave oscillations of the circular cross section near the free surface were shifted in frequency. These shifts were not predicted by the theory. Nonlinear forces on a horizontal circular cylinder beneath waves was investigated experimentally and theoretically by Chaplin (1984). He concluded that the oscillatory loading on the cylinder may be as much as 50% less than that predicted by linear theory. Added mass and damping of two-dimensional rectangular bodies oscillating in heave motion close to the free surface have been studied by Newman et al. (1984). Negative added mass and sharp peaks in the damping and added mass coefficients have been found when the submergence is small and the width of the shallow region on top of the rectangle is large. A linear theory was developed to provide a relatively simple explanation of the occurrence of negative added mass for shallowly submerged bodies. The negative added mass and the rapid variation of the force coefficients were associated with the resonant motion of the free surface in the shallow region. There was relatively weak damping of the standing waves above the body, especially at high frequencies where the body effectively blocked energy radiation to the external portion of the free surface. As a result, the free surface motion in the shallow region was weakly damped and nearly resonant. The results of the theory were compared with numerical results of the Frank (1967) method. Hodges and Webster (1986) compared the force measurements for a slightly submerged rectangular cylinder undergoing vertical oscillations with the linear methods of Frank (1967) and Newman et al. (1984) and with the nonlinear theory by Yum (1985). Again it was found that all the theoretical methods deviated significantly from the experimental results in the low frequency range. Inoue and Kyozuka (1986) presented experimental results of the first and second-order wave forces acting on circular, semi-circular and rectangular, horizontally submerged cylinders. The results were compared with numerical calculations based on a regular perturbation theory. Through the study it was found that the calculation of both first and the second-order wave forces agreed with the experiments when the cylinders are submerged to a sufficient depth. However, in the case of shallow submergency and/or large wave amplitudes, significant discrepancies between the predicted and measured results were observed. A MAC-type finite-difference method based on the Navier-Stokes equations was developed and applied to the problem of wave-induced forces on submerged elliptic and circular cylinders by Miyata et al. (1986). The negative drifting force, which abruptly increased with the decrease of submergence but suddenly decreased and reached a maximum value of opposite sign when the body emerged, was predicted by the theory. This was in fair agreement with the experimental results. Such nonlinear components cannot be interpreted within the framework of a linear theory. Greenhow and Yanbao (1987) collected together some known analytical results concerning the added masses of cylinders near or penetrating fluid boundaries. It was noted that the variation in the added mass when the cylinder is near the free surface gives rise to effects in both the heave and sway modes of motion which may be as large as those due to viscous drag forces. The forces involved contribute a significant percentage of the buoyancy force on a totally submerged cylinder.

One can conclude from the quoted references that none of the analytical methods produced sufficiently accurate predictions of the forces on shallowly submerged bodies. Numerical solutions, despite the inherent cumbersomeness and numerical instability, may provide better approximation of the forces induced by nonlinear phenomena of wave-body interaction.

Estimation of the viscous drag forces is essential to calculate the drift motion. Owing to the complexity of the flow separation problem, viscous damping effects are normally accounted for empirically. Nonlinear forces due to viscous effects acting on two-dimensional cylinders oscillating in still water or otherwise fixed cylinders in an oscillating fluid were reviewed by Sarpkaya and Isaacson (1981). Stansby and Isaacson (1987) reviewed the recent advances in numerical simulation of separated flows. These studies have very limited applications in the present investigation. On the other hand, several experimental investigations were performed to measure the forces on a sphere accelerating in a viscous fluid. An elaborate experimental study was carried out by Odar and Hamilton (1964) in order to measure the added mass and the history coefficients for a sphere oscillating in a viscous liquid in the range of small Reynolds number, Re, less than 62. However, Schoneborn (1975) showed experimentally that in an oscillating flow the drag predicted by the empirical formula of Odar and Hamilton was too low when the frequency of the flow field was in the region of the natural frequency of vortex shedding. Lighthill (1954) and Houghton (1963) had anticipated theoretically this dependence of the flow around the sphere, and hence the drag, on the frequency of oscillation of the flow.

Karanfilian and Kotas (1978) investigated the resistance force acting on a sphere undergoing unsteady motion in a liquid at rest. The resistance was represented by means of an empirical coefficient which depended on the acceleration number, $\dot{U}D/U^2$, and the Reynolds number, UD/ν, where $\dot{U}$, U and D are the acceleration, velocity and diameter of the sphere respectively and ν is the kinematic viscosity of the liquid. The tests were conducted in a Reynolds number range of 10^2 to 10^4 and had acceleration number up to 10.5. The data correlated to the coefficient only with a large degree of scatter.

Restrained by the available information on the drag force experienced by three-dimensional bodies accelerating in fluids, the ice mass in the present study was modelled as a sphere and Kananfilian and Kotas' empirical formula, which lies in an appropriate range of Reynolds number, was modified and utilized to estimate the viscous forces.

1.2 Project Objectives and Scope

In the absence of a full solution of the nonlinear diffraction problem, many researchers have applied the linear diffraction theory, despite its deficiency to predict the motion of small ice masses in waves, as it is the principal method available at present. Hence, the basic objective of the research described herein is to develop a nonlinear theoretical and numerical model capable of predicting the motions of small ice masses under the influence of waves. The size of the ice masses of interest varies approximately between 10^2 to 10^5 tonnes, with the characteristic dimension between 5 to 60 m. The relevant range of wave lengths extends from 60 to 600 m and wave heights up to 35 m. The model should predict motions and trajectories of isolated ice masses floating in an open seaway or near small ships and offshore structures, where the disturbance of the wave field by the structure can be neglected, and in the proximity of a large offshore structure, thus making possible the determination of kinematic parameters of collisions and of the range of impact occurrences around the waterline. It follows that in such a model large motions with respect to the dimensions of the ice mass must be reckoned with and that the drift needs to be calculated as a resultant of a continuous asymmetric oscillatory motion, so that under certain conditions a similarity to a fluid particle motion could be achieved. Simultaneously, the diffraction effects must be adequately evaluated in order to maintain sufficient accuracy at heave resonance conditions and to avoid significant limitations of applicability with respect to the ratio of the characteristic dimension of the ice mass to the wave length. In broad terms the model must fill in the gap between the conditions appropriate for the application of Morison's formula and those suitable for the use of linear diffraction theory.

The evaluation of the computational method requires a sufficiently-extensive comparison of computed and measured motions of ice masses drifting in waves. Therefore a comparison is presented for an ice mass of the form of a smooth sphere for which parameters of motion were obtained from an especially conducted small scale experiment. The choice of the spherical shape was dictated by the availability of experimentally-determined drag coefficients (Karanfilian and Kotas, 1978), and by the resulting simplification of the experimental procedures and the computational algorithm.

In Chapter 2, the theoretical formulation used to calculate the wave forces imposed on a free floating body is presented. The scattering potential is analyzed by the application of the equivalent motion concept. Wave interference effects between a fixed surface-piercing cylindrical structure and the body are treated. Especially conducted experiments to determine the motion of free drifting small spherical ice mass model and the forces on a towed model in waves are described in Chapter 3. In Chapter 4, a comparison between the experimental results and the numerical predictions is considered. A study was performed to investigate the relative importance of various wave fields, the structure size and the eccentricity of the ice mass location on the impact parameters. Chapter 5 summarizes the important aspects of the present study. Detailed derivations of the shape functions, the integration schemes, the incident wave pattern and the diffraction potential due to large vertical cylinder are given in the appendices.

1.3 Significance of the Study

A theoretical and experimental investigation to examine the nonlinear response of small ice masses to a wide range of wave excitations has been conducted. A nonlinear three-dimensional time-domain computer program was developed to predict the motions and trajectories of isolated ice masses in open water and in the vicinity of a large offshore structure. Such motions can be sufficiently well modelled numerically by the proposed method. The equivalent motion concept was applied to estimate the scattering wave forces. The comparison of computed and measured surge forces indicated that the components of hydrodynamic forces were correctly represented in the model. Examples for the motion of small ice masses near a large cylindrical offshore platform have been given. The proposed model can be used to study the kinematic parameters of impact between drifting ice masses with ships and offshore structures.

2.0 THEORETICAL FORMULATION

2.1 Introduction

In this chapter, the theoretical formulation is described for a nonlinear three-dimensional time-domain method for predicting the motion in waves of a small (with respect to wave length) floating body of arbitrary shape. Therein, the body surface is represented by eight-node two-dimensional isoparametric panels. The general equations of motion of a rigid body are applied and the wave forces induced by the undisturbed wave field (Froude-Krylov forces) are computed by a direct integration of pressures over the instantaneous wetted surface of the body. The Froude-Krylov, viscous drag and scattering hydrodynamic forces due to the disturbance of the wave flow by the body are determined for the instantaneous submergence of the body at each time step. The scattering forces are estimated by the equivalent motion concept (Pawlowski, 1982, 1987). The concept makes possible an approximation of the disturbance of an incident potential flow, due to the presence of an impermeable body, by a finite number of predetermined "distortion mode" potentials and their "equivalent" speed amplitudes in such a way that a best fit to the impermeability condition on the body surface is obtained. Viscous forces are estimated by the application of appropriate semi-empirical drag coefficients with respect to the equivalent motion velocity.

At first, the problem of a body floating in open water waves will be formulated and followed by the necessary modifications to account for the presence of a cylindrical structure presented in Section 2.5.

2.2 Systems of Reference

An isolated ice mass is represented by a rigid body of uniform specific density and of a form determined by its external, impermeable surface S of piecewise continuous normals. The motion of the body is observed in a right-handed inertial frame of reference which is fixed in space (Fig. 2.1). The versors (unit base vectors) of the coordinate system are denoted by $\tilde{e}_{oi}$, i=1,2,3 and the corresponding coordinates by x_o, y_o, z_o. The axes x_o and y_o are placed on the undisturbed free surface and the z_o axis is directed upwards. In the free floating reference configuration, body fixed axes (x, y, z) are taken, and remain, parallel to the inertial frame of reference with the origin O located at the body centre of gravity (CG). The radii vectors of the points P of the body are denoted by $\bar{X}$

and the unit normal vectors at the body surface (pointing into the fluid) are signified by $\bar{N}$. Instantaneous configurations of the body are defined by the translated and rotated body fixed system of axes (x', y', z'). The (x, y, z) system is related to the primed system by:

$$\bar{X}' = \bar{\bar{R}} \, . \, \bar{X} \qquad (2.1.a)$$

$$\bar{N}' = \bar{\bar{R}} \, . \, \bar{N} \qquad (2.1.b)$$

where $\bar{X}'$ and $\bar{N}'$ denote respectively the instantaneous radii of the points of the body with respect to CG, and the instantaneous normals at the body surface, while $\bar{\bar{R}}$ is the second order tensor of rotation defined by the matrix:

$$\bar{\bar{R}} = \begin{bmatrix} C_2 C_3 - S_1 S_2 S_3 & - C_1 S_3 & S_2 C_3 + S_1 C_2 S_3 \\ C_2 S_3 + S_1 S_2 C_3 & C_1 S_3 & S_2 S_3 - S_1 C_2 C_3 \\ -C_1 S_2 & S_1 & C_1 C_2 \end{bmatrix} \qquad (2.2)$$

where

$C_i = \cos \eta_i$

$S_i = \sin \eta_i$

and η_i, i = 1, 2, 3 are the rotations of the primed system of axes relative to the reference system (x, y, z) as well as the inertial frame of reference. The matrix represents a rotation η_3 about z axis followed by a rotation η_1 about the new x' axis then by a rotation η_2 about the new y' axis. An instantaneous configuration of the body and the velocity field of its particles are therefore given by the formulas:

$$\bar{x}_o = \bar{x}_{CG} + \bar{X}' \qquad (2.3.a)$$

$$\dot{\bar{x}}_o = \dot{\bar{x}}_{CG} + \bar{\omega} \wedge \bar{X}' \qquad (2.3.b)$$

with $\bar{x}_o$ $(\bar{X}, t)$ representing the instantaneous radius vector of the point $P(\bar{X})$ in the inertial frame, the dots denoting derivatives with respect to time t, and $\bar{\omega}$ indicating the angular velocity (of the rotational motion about the centre of gravity) of the body, defined by:

$$\bar{\omega} \wedge \bar{\bar{I}} = \dot{\bar{\bar{R}}} \cdot \bar{\bar{R}}^T \qquad (2.3.c)$$

where $\bar{\bar{I}}$ represents the unit second order tensor, superscript T denotes transposition and $\wedge$ indicates vector cross-multiplication.

2.3 Hydrodynamic Formulation

The fluid around the body is assumed to be inviscid and incompressible. The flow is considered irrotational and thus can be described by a single-valued velocity potential ϕ. Viscous effects are afterwards taken into account using an appropriate semi-empirical formula based on experimentally determined drag coefficients, no lift effects are considered. The potential is assumed to result from the superposition of an incident flow potential ϕ_I and a scattering potential ϕ_S due to the disturbance of the ambient wave field by the presence of the body:

$$\phi = \phi_I + \phi_S \tag{2.4}$$

The two potentials separately satisfy the Laplace equation:

$$\nabla^2\phi = 0 \ ; \tag{2.5}$$

within the fluid region. This is subject to the bottom boundary condition

$$\partial\phi/\partial z_o = 0 \quad \text{at the sea floor} \ ; \tag{2.6}$$

and the impermeability condition on the wetted surface S_W:

$$\partial\phi/\partial n = v_n \quad \text{on } S_W \tag{2.7}$$

with v_n denoting the normal speed of the body. In addition ϕ_S satisfies the linearized free surface boundary condition

$$(\partial^2\phi_S/\partial t^2) + g(\partial\phi_S/\partial z_o) = 0 \quad \text{at } z_o=0 \ ; \tag{2.8}$$

where g denotes the gravitational acceleration. Furthermore ϕ_S satisfies the radiation condition which states (in polar coordinates)

$$\lim_{r\to\infty} r_o^{1/2} \left[(\partial\phi_S/\partial r_o) - ik\phi_S\right] = 0 \tag{2.9}$$

with $r_o = (x_0^2 + y_0^2)^{1/2}$;

$i = (-1)^{1/2}$

and k representing the wave number

2.3.1 Incident Potential

The incident velocity potential ϕ_I is represented by the potential of second-order wave of finite amplitude (Wiegel 1964) so that:

$$\phi_I = \frac{H\lambda}{2T} \frac{\cosh k\ (z_o + d)}{\sinh kd} \sin\ \theta \ + \frac{3\pi H^2}{16\ T} \frac{\cosh\ 2k\ (z_o + d)}{\sinh^4 kd} \sin 2\ \theta \tag{2.10}$$

with $\theta = kx_o \cos \alpha + ky_o \sin \alpha - \omega t$;

$k = 2\pi/\lambda$

and $\lambda = \dfrac{gT^2}{2\pi} \tanh \dfrac{2\pi d}{\lambda}$

where H, λ, T, k, ω denote the wave height, wave length, wave period, wave number and wave circular frequency respectively, whereas d represents the water depth and α signifies the angle between the direction of the incident wave and the positive x_o axis.

The wave elevation η_I, wave induced pressure p_I and particle velocities are given in Appendix (A).

2.3.2 Scattering Potential

In order to explain in a simple way the advantages of using the equivalent motion concept in calculating the hydrodynamic wave forces, let us examine the inertia forces imposed on a moving body, firstly in a uniform flow and secondly in waves. The total fluid inertia forces F_m imposed on a body moving in a uniformly accelerating flow are:

$$F_m = \rho V\dot{U} + C_I \rho\ V(\dot{U} - \dot{U}_o)$$

where C_I is the added mass factor, ρ is the fluid density, V is the body submerged volume and $\dot{U}$ and $\dot{U}_o$ are the ambient fluid acceleration and the body acceleration, respectively. C_I is a function of body shape which can be measured or calculated. Working values of C_I are known for some standard geometrical shapes; for instance the theoretical value for spheres is 0.5.

The conventional added mass calculated in the way mentioned above takes no account for either the additional disturbances which result from the free surface effects if the incident velocity field is induced by a progressing wave or the variation of the acceleration terms over the body surface. When the body is reasonably small with respect to the wave length, i.e. $D/\lambda < 0.2$, these effects may be neglected, and the total wave force can be estimated by Morison's equation which includes measured values of the drag and the added mass coefficients C_d and C_I. However, there is not a unique method of evaluation of the force coefficients and their meaning then depends on the used method of evaluation (for detailed discussion on this subject refer to Sarpkaya and Isaacson (1981)). Larger bodies, $D/\lambda > 0.2$, however, cause a significant scattering of the incident wave. In this case, the inertia force must include an extra contribution due to the scattered wave and take into account the nonuniformity of the flow which implies that it is no longer valid to characterize the motion in terms of a single reference acceleration since $\dot{U}$ varies over the body surface. The scattering forces can generally be calculated by linear diffraction theory which essentially provides a solution to the boundary value problem with the linearized free surface condition and appropriate body and boundary conditions, (Eqns. 2.6 to 2.9) assuming small amplitudes of body motions in waves. Because of the linearity of the problem, the total potential can be represented by a sum of the incident wave potential, the diffracted potential from an otherwise fixed body and the radiated potential from a body oscillating in otherwise still water. The total scattering force which includes the force due to diffraction cannot directly be computed by using C_I and a fluid particle velocity especially when the body is not entirely small in comparison with the wave length and/or when it performs relatively large motions. It should be mentioned that for large motion C_I cannot be used in conjunction with the linear acceleration of the body to obtain radiation forces.

In order to describe in a simple way the concept of equivalent motion, let us again examine the case of a body moving in waves. If the body was completely permeable, there would be a net flow of fluid through the wetted surface of the body resulting from the differences between the body velocity and the fluid particle velocities. Now, if we set the body to move with a fictitious velocity so that this velocity will minimize the net flow through the body surface, even though there is partial flow penetrating the body surface at different locations, we shall call this fictitious velocity as the equivalent velocity. Thus, to obtain an estimation of the scattering forces, in the mean time, satisfying the impermeability condition on the body wetted surface, the equivalent accelerations are computed by differentiating the equivalent speeds with respect to time, bearing in mind that the equivalent speeds minimize the net flow through S_W with the scattering potential approximated by a finite series of radiation potentials. In addition, the present model estimates the drag forces and therefore fills in the gap between the conditions appropriate for the application of Morison's equation and those suitable for the use of linear diffraction theory.

Following the equivalent motion method, the potential ϕ_S is expressed in terms of an approximating finite series:

$$\phi_s = \phi_u + \sum_{i=1}^{6} p_i \cdot \phi_i \tag{2.11}$$

where ϕ_u satisfies the impermeability condition on the body wetted surface S_w corresponding to the steady motion of the body, ϕ_i represent the modal velocity potentials corresponding to unit amplitude distortion modes of the body surface which satisfy the linear free surface condition, p_i denote the equivalent speed amplitudes of the modal potentials, where i=1, 2, 3 correspond to surge, sway and heave modes of translation and i=4, 5, 6 correspond to roll, pitch and yaw modes of rotation. In the present formulation, the potential ϕ_u represents the potential flow due to steady drift of the body and is assumed to have sufficiently small influence upon the motion of the body to be neglected.

According to the equivalent motion approach, the impermeability condition on the wetted surface S_w of the body is imposed upon the velocity potential ϕ in the integral form considering:

$$L = \int_{S_w} (\partial\phi/\partial n - v_n)^2 \ dS = 0 \tag{2.12.a}$$

where $\partial\phi/\partial n$ is defined as the normal derivative of ϕ:

$$\partial\phi/\partial n = \bar{N}' \,.\, (\partial\phi/\partial\bar{x}_o) \qquad (2.12.b)$$

with $\partial/\partial\bar{x}_o$ signifying the gradient operator and v_n denoting the normal speed of the surface of the body taken as:

$$\begin{aligned} v_n &= (\dot{\bar{x}}_o + \bar{\omega}\wedge\bar{X}') \,.\, \bar{N}' \\ &= (\dot{\bar{x}}_o + \bar{\omega}\wedge\bar{X}') \,.\, \bar{\bar{R}} \,.\, \bar{N} \qquad (2.12.c) \end{aligned}$$

To determine p_i, $i=1,2,\ldots,6$, the minimization conditions are applied yielding:

$$\partial L/\,\partial p_i = 2 \int_{S_w} (\partial\phi/\partial n - v_n)\,(\partial\phi_i/\partial n)\, dS = 0 \qquad (2.13)$$

with the resulting normal equations

$$\sum_{j=1}^{6} p_j \int_{S_w} (\partial\phi_j/\partial n)(\partial\phi_i/\partial n)\,dS = \int_{S_w} (v_n - \partial\phi_I/\partial n)(\partial\phi_i/\partial n)\,dS$$

$$i = 1,2,\ \ldots,\ 6 \qquad (2.14.a)$$

or

$$p_j\, A_{ji} = B_i \qquad i,j = 1,2,\ \ldots,\ 6 \qquad (2.14.b)$$

where

$$A_{ji} = \int_{S_W} (\partial\phi_j/\partial n)\ (\partial\phi_i/\partial n)\ dS; \qquad (2.14.c)$$

$$B_i = \int_{S_W} (v_n - (\partial\phi_I/\partial n))\ (\partial\phi_i/\partial n)\ dS \qquad (2.14.d)$$

The normal equations (2.14) determine speed amplitudes p_i at every instant of time, providing the quantities $(\partial\phi_i/\partial n)$, which define the distortion modes on S_W are given and are linearly independent (Pawlowski, 1982, 1987). The distortion modes are chosen to correspond to rigid body displacements parallel to x,y,z system of reference and to rotations about point CF, which in free floating condition coincides with the body centre of floatation. Therefore:

$$\partial\phi_i/\partial n = \bar{e}_i \cdot \bar{N}' \qquad i=1,2,3$$
$$\partial\phi_i/\partial n = [\bar{e}_i \wedge (\bar{x} - \bar{x}_{CF})] \cdot \bar{N}' \quad i=4,5,6 \qquad (2.15)$$

Thus, p_i can be determined at every instant, and the corresponding scattering force can be evaluated as shown below. It should be inferred that this simplified ϕ_S need not be restricted to rigid body motions in six degrees of freedom but it can also satisfy higher modes of motion such as, for example, the deformation of the body surface. For more details refer to Pawlowski (1987).

2.4 Forces

The generalized hydrodynamic forces are obtained by the summation of the pressure forces resulting from the potential flow described by potential ϕ and forces due to viscous effect. Lift effects are neglected. In the present application the pressure forces are expressed as a sum of Froude-Krylov forces corresponding to ϕ_I and scattering forces corresponding to ϕ_S.

2.4.1 Froude-Krylov Forces

The Froude-Krylov forces $\bar{F}_{FK}$ are obtained by a direct integration of pressure p_T over the instantaneous wetted surface of the body using:

$$\bar{F}_{FK} = -\int_{S_W} p_T \, \bar{N}' \, dS \qquad (2.16.a)$$

and, the moments $\bar{\Gamma}_{FK}$ are given by:

$$\bar{\Gamma}_{FK} = -\int_{S_W} p_T \, (\bar{X}' \wedge \bar{N}') dS \qquad (2.16.b)$$

For the open water case or even when there is a small diffracting structure, p_T represents only the pressure due to incident waves p_I as defined in Appendix (A). At any instantaneous configuration of the body, the intersection of the free surface profile η_T with the body surface gives the wetted surface S_w.

In order to compute the Froude-Krylov forces, the body surface is discretized into quadrilateral isoparametric elements of the second order (Appendix B). For each element the surface integration becomes a double integration. This is carried out using Gauss-Legendre quadrature numerical integration with three sampling points in each direction (Appendix B). For this purpose, the instantaneous free surface elevation is defined by the wave elevation η_T, where η_T in an open seaway is represented by the incident wave elevation η_I defined in Appendix (A).

2.4.2 Scattering Forces

Apart from neglecting the effects of the potential ϕ_u resulting from the steady velocity of the body, a major simplification is introduced here in the evaluation of the scattering forces. The nonlinear contribution of the pressure with respect to the modal potentials ϕ_i is discarded, and the modal potentials are represented by the corresponding radiation potentials for the body oscillating at its free floating configuration. The added mass coefficients a_{kj} and damping coefficients b_{kj} are determined by a standard panel method algorithm (Murray 1987) at the frequency of encounter, which partly compensates for the negligence of ϕ_u. The frequency of encounter ω_e is defined by:

$$\omega_e = \omega - \omega^2 U_{av}/g$$

where U_{av} denotes the average drift speed and g signifies the gravitational acceleration. The average drift velocity can be computed iteratively and in the first approximation can be taken as equal to the drift of a fluid particle in finite amplitude waves. The effect of possible large displacements of the body is taken into account by considering the added mass and damping coefficients to be proportional to the volume of the body submerged below the still water level V' for wave frequencies equal to or higher than the heave resonance frequency of the body. For wave frequencies below resonance, the added mass and damping coefficients are assumed to be proportional to the instantaneous wetted volume of the body V' below the wave elevation.

The added mass and damping coefficients are calculated using the standard expressions of linear diffraction theory:

$$a_{kj} = -\rho \; R \; \{ \int_{S_o} \phi_k \, n_j \, ds) \} \qquad (2.17.a)$$

$$b_{kj} = -\rho\omega_e \; Im \; \{ \int_{S_o} \phi_k \, n_j \, ds \} \qquad (2.17.b)$$

for k, j = 1,2, ..., 6, where R and Im refer to the real and imaginary components respectively, S_o is the submerged body surface at equilibrium in still water and n_j is given by:

$n_1 = n_x$

$n_2 = ny$

$n_3 = n_z$

$n_4 = y \, n_z - z \, ny$

$n_5 = z \, n_x - x \, nz$

$n_6 = x \, n_y - y \, n_x$

where n_x, n_y and n_z denote the direction cosines of $\bar{N}$ in the x,y,z directions. Results of added-mass and damping coefficients and the response amplitude operator calculated by linear diffraction theory in the surge and the heave modes are shown in Figs. 2.2 and 2.3 respectively. The results are obtained for the particular shape of a sphere of density 0.9 t/m^3.

The scattering forces $\bar{F}_s$ are then determined by:

$$(\bar{F}_s)_k = -\sum_{j=1}^{6} [d/dt\ (p_j\ a'_{kj}) + p_j\ b'_{kj}] \quad k=1,2,\ldots,6 \quad (2.19.a)$$

where for k=1,2 and 3, $(\bar{F}_s)_k$ denote force components in directions $\bar{e}_k$ respectively and for k=4,5 and 6, $(\bar{F}_s)_k$ signify moment components with respect to point CF about direction $\bar{e}_{k-3}$. The instantaneous added mass and damping coefficients a'_{kj} and b'_{kj} are defined by:

$$a'_{kj} = a_{kj}\ V'/V \quad k,j=1,2,\ldots,6 \quad (2.19.b)$$

and

$$b'_{kj} = b_{kj}\ V'/V \quad k,j=1,2,\ldots,6 \quad (2.19.c)$$

where V denotes the volume of the displaced water in the free floating condition, i.e. the body is at rest in calm water. This approximation of the instantaneous added mass damping coefficients in equation (2.19) was used to reduce the computational time required to calculate the actual values of the coefficients for the instantaneous submerged volume of the body. Therefore, the terms describing the rate of change of momentum in (2.19.a) take the form:

$$d/dt\ (p_j a'_{kj}) = \dot{p}_j\ a'_{kj} + p_j a_{kj}\ \dot{V}'/V \qquad (2.20)$$

In order to compensate further for the neglected contribution of potential ϕ_u, p_i with i=1,2 in formula (2.19.a) is taken in the form:

$$p_i = p_i^* - (U_{av})_i \qquad (2.21)$$

where $p_i^* = p_i$ when $(U_{av})_i = 0$

and where $(U_{av})_1$ and $(U_{av})_2$ are the average drift speeds in x_o and y_o directions respectively.

Taking into account the symmetry of the spherical form, rotations of the body about CG leave the form of the body surface unchanged. Therefore, $\bar{\bar{R}} = \bar{\bar{I}}$ can be inserted into Eqns. (2.1) and (2.3), and the rotational modes of motion do not contribute to the r.h.s. of Eqn. (2.12). Consequently, the description of the body motion can be reduced to linear displacements and velocities of the CG in the plane of wave propagation. This, however, does not eliminate the rotational distortion modes $p_{4,5,6}$ in equations (2.11), (2.12), (2.15) and (2.19).

2.4.3 Viscous Drag Forces

For the linear displacement modes of motion, the viscous drag forces $\bar{F}_{dr}$ are determined by applying a modified version of the formula proposed by Karanfilian and Kotas (1978) in connection with the fluid resistance forces acting on accelerating deeply submerged spheres. The fluid resistance forces according to Karanfilian are represented by:

$$F_{vk} = 0.5\ C\rho\ |\dot{x}|\dot{x} \cdot (\pi D^2/4) \qquad (2.22.a)$$

where ρ is the fluid density, D and $\dot{x}$ are the sphere diameter and velocity respectively and C is the unsteady-motion drag coefficient calculated from

$$C = (A_n + 1)^{\beta}\ C_d \qquad (2.22.b)$$

while β is given by:

$\beta = 1.2 \pm .03$;

The acceleration number A_n is given by:

$$A_n = |\ddot{x}|D/(\dot{x})^2 \; ; \qquad (2.22.c)$$

and C_d is the steady-motion drag coefficient which is a function of the Reynolds number, Re, and it is approximated in the range of $10^{-2} \leq \mathrm{Re} \leq 10^5$ by the seventh-degree polynomial in Log Re identified in Karanfilion and Kotas (1978) by:

$$\mathrm{Log}\, C_d = \alpha_o + \alpha_1 \log \mathrm{Re} + \alpha_2 (\log \mathrm{Re})^2 + \ldots + \alpha_7 (\log \mathrm{Re})^7$$

where

$\alpha_o = 1.429$, $\alpha_1 = -.8856$, $\alpha_2 = 8.081 \times 10^{-2}$

$\alpha_3 = 1.085 \times 10^{-2}$, $\alpha_4 = -3.9 \times 10^{-3}$

$\alpha_5 = 4.31 \times 10^{-4}$, $\alpha_6 = 2.55 \times 10^{-4}$

$\alpha_7 = -4.63 \times 10^{-5}$

In the range of $10^5 < \mathrm{Re} < \infty$, C_d is approximated (Chow, 1979) by:

$$\begin{aligned} C_d &= 0.5 \quad \text{for } 10^5 < \mathrm{Re} < 3 \times 10^5 \\ &= .08 \quad \text{for } \mathrm{Re} = 3 \times 10^5 \\ &= 3.66 \times 10^{-4} (\mathrm{Re})^{0.4275} \quad \text{for } 3 \times 10^5 < \mathrm{Re} \leq 2 \times 10^6 \\ &= .18 \quad \text{for } \mathrm{Re} > 2 \times 10^6 \end{aligned}$$

where $\mathrm{Re} = |\dot{x}|D/\nu$ (2.22.d) and ν represents the kinematic viscosity of the fluid.

Although Karanfilian and Kotas derived the semi-empirical formula (2.22) from experimental data in the range of Reynolds number of $10^2 \leq Re \leq 10^4$ and acceleration number of $A_n \leq 10.5$, here the formula is assumed to be valid for all values of Re beyond the specified range of application. However, to correct for the inertia force included in the formula and a partial submergency of the sphere, the following modified expression is used to determine the drag forces:

$$(\bar{F}_{dr})_k = -[0.5C\rho \ (\pi \frac{D^2}{4})|U|U_k - 0.5 \ M \ \dot{U}_k]S_w/S \quad k=1,2,3 \qquad (2.23)$$

in the range of Renolds number $10^{-2} \leq R \leq \infty$ where U_k and $\dot{U}_k$ signify respectively the equivalent velocities and accelerations, M represents the body mass and S_w and S denote the instantaneous wetted surface and the total surface area of the sphere respectively. It should be noted that the theoretical value of the added mass coefficient 0.5 of a sphere oscillating linearly with small amplitudes in a fluid was used to estimate the inertia resistance. In this case Re and A_n are defined as:

$$Re = |U|D/\nu$$

with $U = \left(\sum_{k=1}^{3} U_k^2\right)^{0.5}$

and $A_n = |\dot{U}|D/U^2$ for $A_n \leq 10.5$

with $\dot{U} = \left(\sum_{k=1}^{3} \dot{U}_k^2\right)^{0.5}$

It should be noted that the velocity in x and y directions U_1, U_2 is a combination of the equivalent velocities p_1, p_2 and p_4, p_5 so that:

$$U_1 = p_1 + (z_{CF}-z_{CG}) \cdot p_5 \tag{2.24.a}$$

$$U_2 = p_2 - (z_{CF}-z_{CG}) \cdot p_4 \tag{2.24.b}$$

where z_{CF} and z_{CG} is the vertical coordinate of points CF and CG respectively, while the velocity in z direction U_3 is given by:

$$U_3 = p_3 \tag{2.24.c}$$

2.5 Motion Near Cylindrical Structure

The effect of the presence of a surface piercing cylindrical structure of radius a on the wave exciting forces is taken into account by assuming the total potential ϕ as:

$$\phi = \phi_I + \phi_d + \phi_s$$

where ϕ_I and ϕ_s are as previously defined whereas ϕ_d is the first order wave potential diffracted from the structure (presented in a cylindrical coordinate system (r, γ, z) as indicated in Figure C.1, Appendix C) given by:

$$\phi_d = \frac{-igH}{2\omega} \frac{\cosh[k(z + d)]}{\cosh\ (kd)} \{ \sum_{m=0}^{\infty} \beta_m\ B_m H_m^{(1)}(kr) \cos(m\gamma) \} e^{-i\omega t}$$

$$\text{for } r \geq a$$

where H, ω, and k signify the wave height, wave frequency and wave number respectively, d represents the water depth, $H_m^{(1)}\ (kr)$ denotes the Hankel function of the first kind of order m and argument kr, with

$$\beta_m = 1 \text{ for } m = 0$$

$$= 2i^m \text{ for } m \geq 1$$

and $B_m = -J'_m(ka)/H_m^{(1)'}(ka)$

$$i=(-1)^{1/2}$$

where Jm (ka) represents Bessel function of the first kind of order m and argument ka. The prime denotes differentiation with respect to the argument. The term representing water particle velocity perpendicular to the body surface $\partial\phi_I/\partial n$ is therefore replaced by $\partial(\phi_I + \phi_d)/\partial n$ in Eqns. (2.12), (2.13) and (2.14). The wave elevation η_T and wave pressure p_T are accordingly defined to incorporate the effect of ϕ_d as:

$$\eta_T = \eta_I + \eta_d \tag{2.25}$$

$$p_T = p_I + p_d \tag{2.26}$$

where η_d and p_d are the wave elevation and pressure due to the diffracted wave, defined in Appendix C.

2.6 Equations of Motion

The equations of motion of a rigid body are expressed by:

$$M\ddot{\bar{x}} = \bar{F}$$

$$\bar{\bar{J}}\dot{\bar{\omega}} + \bar{\omega}\wedge\bar{\bar{J}}\cdot\bar{\omega} = \bar{\Gamma}'$$

where M is the body mass, $\bar{\bar{J}}$ is the inertia tensor relative to the body axes, $\bar{F}$ is the exciting force vector with components taken relative to the inertial frame, $\bar{\Gamma}'$ is the vector containing the moment of forces about the centre of gravity of the body with components taken relative to the body fixed axes, $\ddot{\bar{x}}$ is the linear acceleration of the body center of gravity taken relative to the space fixed axes, and $\bar{\omega}$ is the body angular acceleration with components taken relative to the body fixed axes.

The force vector $\bar{F}$ is obtained by summing the Froude-Krylov forces $\bar{F}_{FK}$, the scattering forces $\bar{F}_S$, the viscous drag forces $\bar{F}_{dr}$ and the gravity forces. Owing to the symmetry of the spherical shape, the moments $\bar{\Gamma}'$ are set equal to zero to eliminate the numerical instability in rotational motions. In order to compute the resulting body displacements, a version of the predictor-corrector method (Bass 1985) is used for the numerical integration of the equations of motion in time.

A numerical algorithm based on the theoretical formulation was developed and a flow chart of the computer program is presented in Fig. (2.4).

The computer program reads the body data, i.e. the coordinates of the nodal points on the body surface and the connectivity matrix that determines the 8-node isoparametric panels, the wave conditions, the structure diameter, the initial conditions of the body motion and the length of the simulation period. At the beginning of a computer run, the program senses the magnitude of the forces and the motion using very small time steps. Then, the time steps are increased to appropriate values to save computational time. A new body position is predicted by the motion program using past motion information. The hydrodynamic forces are calculated by first computing the wave field characteristics which define the instantaneous wetted body surface. The Froude-Krylov forces are then calculated by integrating the wave pressure over the body surface. The equivalent velocities and accelerations are determined and the corresponding scattering and drag forces are computed. The motions in six degrees of freedom and the body position are then calculated based on the evaluated forces. The calculated position is compared with the predicted one and if the errors are acceptable according to percentages specified by the user, the program proceeds to the next time step. Otherwise the step is halved and the loop is repeated until the desired accuracy is achieved. The numerical calculations continue to the end of simulation period or until impact with the structure (if any) occurs.

3.0 EXPERIMENTAL INVESTIGATION

3.1 Introduction

The purpose of the experimental investigation was to determine the response of small ice masses to regular wave action and to measure the forces in the surge direction imposed on a heaving model in waves, while being towed with the corresponding constant drift speed found from the free floating experiments. Comparisons between the measured motions of the freely drifting model and the corresponding theoretical predictions were to indicate the overall performance and limitations of the numerical simulation while the measured forces will make possible an accurate assessment of the theoretical approach used to compute the forces. Owing to the scarcity and deficiency of the available data on the measured motion parameters of models of spherical ice masses in waves, the following tests were carried out to provide a comprehensive set of data in a wide range of wave frequencies and wave heights.

3.2 Apparatus and Experimental Technique

The experiment was carried out in the wave/towing tank at Memorial University of Newfoundland (Fig. 3.1). The testing section of the tank is 4.37 m wide and 54.74 m long. A water depth of 1.80 m was maintained throughout the test series. Waves were generated by means of piston type wave board, while the towing carriage was used to simulate the average speed of the ice mass.

Two spherical models (Fig. 3.2) of diameter D equal to 0.3 m and density of 900 kg/m^3 were fabricated to model the bergy bit shape and mass based on Froude laws of similarity. The first model was cast of paraffin wax while the second was machined of wood with a wall thickness of .02 m. Two series of tests were conducted using regular wave trains of wave length λ ranging from .61 to 5.45 m ($D/\lambda=1/2$ to $1/18$) and wave height H from .02 to .3 m ($H/\lambda=1/100$ to $1/10$). Wave frequencies were accurately set by the wave board controller. Wave heights were measured by means of resistive type wave probes. The generated steepness, reported in the Tables (4.1 to 4.4), differed slightly from those targeted.

In the first test series, the wax model was set free floating. Wave-induced motions of the ice model parallel to a scaled grid were recorded by a video camera equipped with a digital clock (Figs. 3.1 and 3.3). The experimental setup was similar to that reported in Lever et al. (1984).The grid was parallel to the direction of wave propagation and caused virtually no disturbance to the incident wave field. Time was measured using a stop watch as the model drifted through two marked stations and the corresponding average drift velocity U_{av} was calculated. The video recordings thereafter were mapped using a monitor. Pictures were advanced frame by frame, the relative position of the sphere with respect to the grid and as dependent on measured time in centi-seconds was plotted. The average model velocities over approximately 0.1 second intervals were thus computed taking into consideration a correction factor applied to account for the position of the grid and the model relative to the camera. The actual velocity was calculated using the equation:

$$V_{actual} = V_{image} \cdot (3.94 - X)/3.94$$

where X is the distance from the model to the grid in meters and 3.94 m is the distance from the camera to the grid. The relative errors of the measurements of motion parameters were estimated at ± 15%.

In the second series of tests, the wooden sphere was attached to a dynamometer installed on the towing carriage by means of connecting rod, and was free to heave (Fig. 3.4). The model was ballasted so that the total arrangement (model + connecting rod + the moving part of the dynamometer + ballasting weight) had the desired modelled mass. A resistive type wave probe was installed on the carriage to measure the wave profile parallel to the body centre. The model was towed, in repeated wave conditions and at forward speeds equal to the corresponding speeds of free drift obtained from the first series of tests with a minimum of 3 cm/sec due to the limit of the carriage characteristics. Wave elevation, body heave motion and forces in the direction of surge were recorded on a Hewlett-Packard HP9825 desk top computer using a 20Hz sampling frequency. An eight-channel FM tape recorder was used as a backup recording system (Fig. 3.5). Test runs were about 30 cycles long to ensure sufficient record of steady state response and were terminated before significant wave energy reflected from the beach reached the test area. Data were transferred to a VAX-11/750 computer, and the small amplitude high frequency force content due to some vibrations of the towing system were filtered out. Forces and heave motions were then extracted, and spectral analysis of the raw and filtered data showed a reduction in the total energy of less than 3% due to filtering.

Samples of the measured forces, heave response and wave elevations at the body centre are presented in Figs. 3.6 to 3.9. It is shown in the figures that heave response was altered in small amplitude waves while regular patterns occurred in larger wave heights.

4.0 RESULTS AND DISCUSSION

A summary of the results for the towed body in waves and of the free drift test series are shown in Tables 4.1 to 4.4. The maximum body velocities in surge U_{max} and in heave V_{max} together with the heave heights $2Z_a$ were obtained from the analysis of the video tapes. The heave heights referenced here replaced the traditional heave amplitudes for the apparent reason that the amplitudes are not symmetric around the still position. For very small motions or for total submergence of the free drifting model, a reliable estimate of the motion parameters was not available (indicated in the table by symbol NA). In some other cases, only rough estimates were possible which are identified by an approximate equality sign $\approx$. To facilitate the comparison, the computed and observed results are presented in Figs. 4.1, 4.2 and 4.4 to 4.7 in a normalized form. Comparisons of the measured and computed motion parameters versus linear diffraction theory results are shown in Figs. 4.8 to 4.10 for different wave steepness. Computed results for a sphere moving in proximity of a large gravity structure are presented in Figs. 4.13 to 4.18. The effects of structure size, eccentricity of body position and wave conditions on the ice mass trajectory are demonstrated. Experimental investigation of such motions could not be performed due to the lack of a wave basin which does not suffer from width restrictions. The spherical surface of the ice mass was modelled using 56 eight-node isoparametric panels for all time-simulations. This discretization introduced less than 2% error in the volume of the body. The error could be attributed to the nature of curvature of the panels. The isoparametric panels had parabolic curvature unlike the actual body surface which is spherical. Nevertheless, such small errors implied that the body representation was sufficiently accurate. Used CPU time was 10 to 11 hours on VAX-11/750 computer for 28 wave cycle runs in close vicinity of the platforms while for the open sea conditions, runs of 18 wave cycles long were performed in range of CPU time between 45 to 90 minutes.

4.1 Towed Model

Table 4.1 shows good agreement between the measured force in surge direction and heave heights of the towed body in comparison with the computed values. Fig. 4.1 shows the computed and measured forces in the surge direction. It is clear from the figure that for steep waves ($H/\lambda=1/10$) the predicted and measured values are in good agreement. For smaller wave heights, the numerical method under-estimated the measured values, however as λ/D increased, the deviation decreased. It is seen from Fig. 4.1 that the numerical method in general gave good predictions of the horizontal force with the exception of waves of low steepness at $\lambda/D<6$. In Fig. 4.2, results for the heave motion are presented. Systematic overprediction of the heave height occurred in the short and medium waves, $\lambda/D\leq 8$, whereas better agreement is evident in longer waves.

It is inferred that friction and damping of the dynamometer altered the heave responses in small wave amplitudes. Also, a shift in the resonance frequency from $\lambda/D=10$ to $\lambda/D=13$, introduced by the dynamometer characteristics, can be perceived from Fig. 4.2. Although the connecting rod was sufficiently short and stiff, some inertial forces were generated by a small backlash in the moving part of the dynamometer. These factors may account for part of the discrepancies between the calculated and measured maximum forces and heave motions.

A time-history sample of the computed force components in the surge direction, i.e., Froude-Krylov, scattering and viscous drag forces is plotted in Fig. 4.3. Considerably high scattering forces which resulted from the restriction of body motions in the surge mode contribute a significant part to the total imposed wave forces. The nonuniform changes in viscous forces imply the limitations of the semi-empirical formula used to estimate the drag forces on an accelerating sphere in a fluid.

Table 4.2 shows the components of the computed forces for the towed model. The total force is usually less than the summation of all maximum forces due to the differences of phase angles. It is shown in the table that the scattering forces F_s are comparable to the Froude-Krylov forces throughout the whole range of waves as a result of the restriction on the motion in the surge mode. Thus, for towed icebergs, or ships, under similar conditions, one should expect rather high scattering forces. The viscous drag forces F_{dr} make smaller, but considerably important, contributions to the total force. The reported force values in the table tend to have little nonlinearity with respect to the wave heights.

4.2 Free Drifting Model

Table 4.3 summarizes the results of the free drift tests. It is of interest to examine the heave behaviour of the free floating body near resonance, i.e. for λ/D between 7 and 11. A heave amplification factor $2Z_a/H$ of 2 was measured at $\lambda/D=10.2$ and wave steepness of 1/88, whereas a heave amplification factor of 3.6 at heave resonance ($\lambda/D=7.8$) was reported in Lever (1984). However, as the wave amplitude increased, a noticable reduction in the amplification factor was observed. For example, a factor of 0.22 for $\lambda/D=10.2$ with 1/9 steepness, is calculated from Table 4.3. In this case total submergence of the body into the wave crest and large exposure at the wave trough occurred, therefore, the relative motion of the body with respect to the still water line remained relatively small. This finding is in contrast with the preconceived notion of the small ice masses "jumping" out of the water due to large excursions. It is also shown in the table that the body assumes the motion of water particles at the free surface at $\lambda/D \geq 13$. The computed wave particle velocities reported in the table are based on Stokes second order wave theory presented in Wiegel (1964).

It is seen from Table 4.3 that for $\lambda/D \leq 2$, the drift speed contributes a major part of the berg kinetic energy. In the range $5 \leq \lambda/D \leq 18$, the average drift velocity is about 20% of the maximum horizontal velocity. Consequently, to obtain an accurate estimate of the iceberg kinetic energy, even for long wave conditions, the instantaneous speed, which is a combination of drift and oscillatory velocities, should be considered.

Table 4.4 shows the computed force component in surge and heave modes for the free drifting model. The contribution of the scattering forces F_S decreases as the wave length increases. The influence of F_S on the motion cannot be neglected in short and medium wave range, $\lambda/D \leq 10$. However, the scattering and drag forces, even when they are small, influence the final body motion especially the drift speed throughout the entire range of the simulation.

The comparison is hampered by the uncertainty related to the experimental results where the relative errors of the motion parameters are estimated at ±15%. However, it is seen from Figs. 4.4 to 4.7 and Table 4.3 that a large number of the computed values are in good agreement with the corresponding experimental results. Fig. 4.4 shows the measured and calculated results of the average drift speed U_{av} in addition to the results of Lever (1984). Good agreement is evident throughout almost the entire range of the test except close to the heave resonance frequency at $\lambda/D=10.2$ and large steepness of $H/\lambda=1/9$ where an over-prediction of the velocity occurred. It is clear from Figs. 4.5, 4.6 and 4.7 that large over-predictions of the motion parameters, in particular of the heave height, occur in the heave resonance range λ/D between 7 and 11. This tendency is more pronounced in steep waves for $H/\lambda=1/10$. In spite of that, at resonance, the computed values in heave mode are more accurate than those produced by applying the linear diffraction theory. It appears from Fig. 4.5 that an 80% over-prediction of U_{max} takes place at short wave conditions $\lambda/D=2$ where the velocities are relatively small and accurate measurements are difficult to extract. However, the differences between the computed and measured motion parameters in the range $\lambda/D<7$ are quantitatively small and can be attributed to the difficulty in measuring the small motions of the body. In fact, if the average drift speeds were removed from the computed U_{max} in the range of $\lambda/D<7$, the results for the surge velocity will agree well with those predicted by the linear diffraction theory. However, better agreement is evident in longer waves. For example, the computed U_{max} agrees with the observed values within ±20% except for steep waves in the heave resonance range where the differences are larger. Fig. 4.6 indicates that the computed values of V_{max} are in good agreement with the experimental ones except in the range $\lambda/D=7.5$ where the measured heave motions are small. It is seen from Fig. 4.7 that the computed heave heights tend to be linearly proportional to wave heights for $\lambda/D>7$ and wave steepness $H/\lambda \leq 1/20$. Observed and predicted heave heights compared reasonably well in the range $5 > \lambda/D > 10.2$.

Accurate simulation of the body motion at heave resonance where it experiences shallow submergence in wave crests is a difficult task. As previously mentioned in the literature review, the body under such conditions will encounter large and abrupt changes in the wave drift forces as well as in the added mass and damping coefficients. These variations cannot be precisely predicted by the linear diffraction theory used here to determine the coefficients. Further investigation of the pertinent phenomena is advisable and improvements in the numerical model are possible.

Figs. 4.8, 4.9 and 4.10 show a comparison between the measured and the computed maximum surge and heave velocities versus the results obtained from the application of linear diffraction theory for wave steepness 1/10, 1/20 and 1/30 respectively. It is evident that the present method has produced, almost consistently, better agreement with the measured values than those predicted by linear diffraction theory especially in heave mode. One should bear in mind that linear diffraction theory does not account for the drift motion; therefore, it under-estimates U_{max} as shown in the figures. It is inferred from the figures that in waves of small steepness the drift velocity is reduced and the results of the present simulation as well as the linear theory agree well with the measured U_{max}.

Fig. 4.11 depicts the measured paths of the body in long and short waves and the corresponding water particle motion at the free surface in comparison with the calculated paths. It is obvious that for medium and short waves, the orbital motion of a particle is significantly different from that of the body, whereas the computed and observed trajectories match well. Samples of the computed force-time history are presented in Fig. 4.12. As expected, the scattering force influence diminishes as the wave length increases.

It appears that the systematic discrepancies between the computed and observed motion parameters and forces, especially at heave resonance range, reflect the limits of applicability of the algorithm in its current form. Nevertheless, further improvements to the method are expected by implementing the modifications suggested below.

4.3 Motion Near a Gravity Base Platform

A gravity base platform, represented here by a surface piercing circular cylinder, disturbs the incident wave train in the near field consequently affecting the motion of small ice masses in close vicinity. The simplified theoretical approach described in Chapter 2 to account for the effects of the diffracted waves generated by the structure, is used to calculate the results shown in Figs. 4.13 to 4.18. Simulations are performed using two structure diameters, 2a, of 120 and 60 cm, i.e., 4 to 2 times the body diameter.

From Fig. 4.13 it can be concluded that for 2a/D=4 and in short steep waves ($\lambda/D=3.3$ and $H/\lambda=1/10$) the motion of the body is marginally affected by the presence of the structure and collision occurred almost at the maximum horizontal velocity of the body. For longer waves ($\lambda/D \geq 10.2$, $H/\lambda \geq 1/20$) and large cylinder (2a/D=4) the body approached the structure to a minimum distance then drifted away and ultimately reached a stationary position in front of the platform, as shown in Figs. 4.14 and 4.15. Eventually, a small disturbance will deflect it away. The body also experiences large heave motions as it draws near the platform where the diffracted wave is most pronounced, which is a repeated phenomenon in all large cylinder and long steep wave conditions (Figs. 4.14 to 4.18). In Fig. 4.15, the body came near the structure and oscillated with a reduced horizontal velocity with a maximum of 40% of the corresponding U_{max} for the open water case. Fig. 4.16 demonstrates the effect of an eccentric body position with respect to the structure/ambient flow axis of symmetry. The ice mass deflected around the structure and no impact took place. Comparison between Figs. 4.15 and 4.18 shows the influence of structure size on the body motion. For conditions of $2a/D=4$, $D/\lambda=13.1$ and $H/\lambda=1/20$ in Fig. 4.15, no impact occurred. The body experienced a reduction, with respect to the computed open water values, in the maximum horizontal velocity and an increase in the heave height motion as well as in maximum vertical velocity. Meanwhile, for a smaller structure size, $2a/D=2$ in Fig. 4.18, the body impacted the platform with approximately 40% of its U_{max} and with full V_{max} moving downward.

These findings could not be compared with experiments or reliable data from the open literature; however, they appear to be reasonable and provide first insight into the behaviour of drifting ice masses in the vicinity of large fixed structures.

4.4 Improvements and Further Development

The predictions of the motion parameters can be improved by:

1. closer examination of the pertinent physical phenomena within the heave resonance range;
2. inclusion of time varying added mass and damping coefficients calculated by linear diffraction theory for different submergence of the sphere;
3. calculating the added mass and damping coefficients taking into account the presence of the gravity structure;
4. developing more accurate formula for calculating viscous drag forces on accelerating semi-submerged spheres in fluid;
5. accounting for the scattering potential effect on the free surface profile, when updating the instantaneous wetted body surface.

6. the method can be extended to account for second order scattering forces, irregular waves and current effects and also for the influence of an oscillating structure, e.g. a semisubmersible, on the body motion.

5.0 CONCLUSIONS

The results presented here show that the motions of bergy bits and growlers in waves should be considered as oscillatory and progressing so that the drift motion appears to be the resultant of horizontal displacements. In the range of short waves, $\lambda/D \leq 4$, the motions are dominated by drifting whereas a particle-like response to wave excitation is observed for $\lambda/D \geq 13$ which confirms the findings of Lever (1984). The motions can at present be sufficiently well modelled numerically, assuming that the ice mass is represented by a sphere of similar specific density and weight, although several improvements of the numerical method are possible and desirable.

Comparison between the computed and measured motion parameters showed that the developed method gives reliable estimates of average drift speeds practically over the entire range of relative wave length ratios $2 \leq \lambda/D \leq 18$. The maximum surge speeds are also fairly well-predicted within the whole range of λ/D for waves of steepness 1/30 and 1/20. For waves of steepness 1/10 the method closely predicts the observed surge speeds, but appears to over-predict the values in two cases, namely at heave resonance range and at $\lambda/D=2$ where the comparison is hampered by the inaccurate measurements. Nevertheless, at $\lambda/D=2$ the computed oscillatory surge velocity agrees well with the values predicted by the linear diffraction theory.

Good agreement between the predicted and measured values is also observed for heave maximum speeds outside the range $7 \le \lambda/D \le 9$ and for heave motion amplitude outside the range $5 \le \lambda/D \le 11$. The motion within the specified ranges is significantly affected by the flow phenomena due to the occurrence of body shallow submergence and overtaken by waves. These phenomena are not modelled adequately by the present method, which results in an over-prediction of the heave parameters. However, it should be noticed that the computed values are much better than those predicted by the linear diffraction theory in these ranges and at present no other adequate method to predict hydrodynamic forces under these conditions is known.

The comparison of computed and measured surge forces indicates that the components of hydrodynamic forces are correctly represented in the model. The equivalent motion concept can be used for predicting wave forces imposed on small drifting ice masses. However further improvements of the numerical model should be considered especially with respect to the phenomena pertinent to heave resonance and viscous damping.

The numerical approach can also be used to examine the motion of bergy bits and growlers in the near proximity of a gravity base structure. However, accuracy of the predicted results, though they look reasonable, cannot be assessed because of lack of experimental measurements and field data, and therefore further experimental investigation is required.

6.0 REFERENCES

Aboul-Azm, A.F., 1982, "Drift of Icebergs Affected by Wave Action", M.Eng. Thesis, Memorial University of Newfoundland, p. 58.

Andersson, L., Lindberg, K. and Ygge, A., 1986, "A Structural Safety of Semis in Sub-Arctic Waters", Proceedings of International Offshore and Navigation Conference, POLARTECH '86, Vol. 2, 1986, pp. 540-564.

Arunachalam, V.M., Murray, J.J. and Muggeridge, D.B., 1987, "Short Term Motion Analysis of Icebergs in Linear Waves", Cold Regions Science and Technology, No. 13, pp. 247-258.

Bass, D.W., 1985, "The Solution of the Equations of Motion for a Rigid Body", Institute for Marine Dynamics, National Research Council of Canada, Report MTB-167.

Chaplin, J.R., 1984, "Nonlinear Forces on a Horizontal Cylinder Beneath Waves", Journal of Fluid Mechanics, Vol. 147, pp. 449-464.

Cheema, P.S. and Ahuja, H.N., 1978, "Computer Simulation of Iceberg Drift", Proceedings of the Offshore Technology Conference, OTC '78, pp. 565-571.

Chow, Chuen-Yen, 1979, "An Introduction to Computational Fluid Mechanics", John Wiley and Sons, New York.

Chung, J.S., 1977, "Forces on Submerged Cylinders Oscillating near a Free Surface", Journal of Hydronautics, Vol. 11, No. 3, pp. 100-106.

Dempster, R.T., 1974, "The Measurement and Modelling of Iceberg Drift", Proceedings of the Oceans '74 Conference, Institute of Electrical and Electronic Engineers, pp. 125-129.

El-Tahan, M.S.S., 1980, "Modelling of Iceberg Drift", M.Eng. Thesis, Memorial University of Newfoundland, p. 72.

Frank, W., 1967, "Oscillation of a Cylinder in or below the Free Surface of Deep Fluids", Naval Ship Research and Development Center, Navy Department, Report No. 2357.

Garrett, C.J.R., 1984, "Statistical Prediction of Iceberg Drift", Iceberg Research, No. 7.

Garrison, C.J., 1978, "Hydrodynamic Loading of Large Offshore Structures, Three-Dimensional Source Distribution Methods", Numerical Methods in Offshore Engineering, Wiley, Chichester, England, pp. 79-140.

Gaskill, H.S. and Rochester, J., 1984, "A New Technique for Iceberg Drift Prediction", Cold Regions Science and Technology, Vol. 8, pp. 223-234.

Greenhow, M. and Yanbao, L., 1987, "Added Masses for Circular Cylinders Near or Penetrating Fluid Boundaries - Review, Extension and Application to Water-Entry,-Exit and Slamming", Journal of Ocean Engineering, Vol. 14, No. 4, pp. 325-348.

Hay and Company Consultants Inc., 1986, "Motion and Impact of Icebergs", Environment Studies Revolving Funds Report, No. 44, p. 135.

Hodges, S.B. and Webster, W.C., 1986, "Measurement of the Forces on a Slightly Submerged Cylinder", Proceedings of the Twenty-First American Towing Tank Conference, pp. 87-97.

Hogben, N., 1974, "Fluid Loading on Offshore Structures, A State-of-the-Art Appraisal Wave Loads", Maritime Tech. Monograph, No. 1, RINA.

Houghton, C., 1963, "The Behaviour of Particles in a Sinosoidal Velocity Field", Proceedings of the Royal Society, A272, pp. 33-43.

Hsiung, C.C. and Aboul-Azm, A.F., 1982, "Iceberg Drift Affected by Wave Action", Journal of Ocean Engineering, Vol. 9, No. 5, pp. 433-439.

Inoue, R. and Kyozuka, Y., 1986, "Nonlinear Wave Forces Acting on Submerged Horizontal Cylinders", Proceedings of the Fifth International Offshore Mechanics and Arctic Engineering Symposium, OMAE '86, Vol. 1, pp. 225-234.

Isaacson, M. de St. Q., 1979, "Wave-Induced Forces in the Diffraction Regime", Mechanics of Wave-Induced Forces on Cylinders, Pitman, London, pp. 68-89.

Isaacson, M., 1985, "Iceberg Interaction with Offshore Structures", Proceedings of the Conference Arctic '85, pp. 276-284.

Isaacson, M., 1986a, "Ice Mass Motions Near an Offshore Structure", Proceedings of the Fifth International Offshore Mechanics and Arctic Engineering Symposium, OMAE '86, Vol. 1, pp. 441-447.

Isaacson, M., 1986b, "Ice Mass Near a Large Offshore Structure", Proceedings of Ocean Structural Dynamics Symposium, pp. 262-276.

Isaacson, M. and Dello Stritto, F.J., 1986, "Motion of an Ice Mass Near a Large Offshore Structure", Proceedings of the Offshore Technology Conference, OTC '86, Vol. 1, pp. 21-27.

Karanfilian, S.K. and Kotas, T.J., 1978, "Drag on a Sphere in Unsteady Motion in a Liquid at Rest", Journal of Fluid Mechanics, Vol. 87, Part 1, pp. 85, 96.

Kobayashi, N. and Frankenstein, S., 1986, "Interaction of Waves with Ice Floes", Proceedings of the 8th. Symposium on Ice, International Association of Hydraulic Research, pp. 101-112.

Kobayashi, N. and Frankenstein, S., 1987, "Wave Drift Force on Ice Floe", Journal of Waterway, Port, Coastal and Ocean Engineering, American Society of Civil Engineering, Vol. 113, No. 5, pp. 476-492.

Lever, J.H., Reimer, E. and Diemand, D., 1984, "A Model Study of the Wave-Induced Motion of Small Icebergs and Bergy Bits", Proceedings of the Third International Offshore Mechanics and Arctic Engineering Symposium, OMAE '84, Vol. III, pp. 282-290.

Lever, J.H., Attwood, D. and Sen, D., 1988, "Factors Affecting the Prediction of Wave-Induced Iceberg Motion", Cold Regions Science and Technology, in press.

Lighthill, M.J., 1954, "The Response of Laminar Skin Friction and Heat Transfer to Fluctuations in the Stream Velocity", Proceedings of the Royal Society, A224, pp. 1-23.

MacCamy, R.C. and Fuchs, R.A., 1954, "Wave Forces on Piles: A Diffraction Theory", U.S. Army Corps of Engineers, Beach Erosion Board, Technical Memo No. 69.

McTaggert, K.A. and Davenport, A.C., 1986, "Wind/Wave Tank Tests of Drifting Iceberg Models", Proceedings of International Offshore and Navigation Conference, POLARTECH '86, Vol. 1, pp. 364-379.

Mei, C.C., 1978, "Numerical Methods in Water-Wave Diffraction and Radiation", Annual Reviews in Fluid Mechanics, Vol. 10, pp. 393-416.

Mei, C.C., 1983, "The Applied Dynamics of Ocean Surface Waves", John Wiley and Sons, New York.

Miyata, H., Kajitani, H., Katsumata, M. and Ishibashi, F., 1986, "Nonlinear Wave-Induced Forces on a Shallowly Submerged Body", Proceedings of the Fifth International Offshore Mechanics and Arctic Engineering Symposium, OMAE '86, Vol. 1, pp. 218-224.

Mountain, D.G., 1980, "On Predicting Iceberg Drift", Cold Regions Science and Technology, Vol. 1, pp. 273-282.

Murray, J.J., 1987, "A Computer Program to Calculate Hydrodynamic Loading and Response of Floating Bodies Using Green's Function Panel Method", Institute for Marine Dynamics, National Research Council of Canada, Report RR-HYD-02.

Murray, J.J., Guy, G.B. and Muggeridge, D.B., 1983, "Response of Modelled Ice Masses to Regular Waves and Regular Wave Groups", Proceedings of the Ocean '83 Conference, Institute of Electrical and Electronic Engineers, pp. 1048-1052.

Newman, J.N., Sortland, B. and Vinje, T., 1984, "Added Mass and Damping of Rectangular Bodies Close to the Free Surface", Journal of Ship Research, Vol. 28, No. 4, pp. 219-225.

NORDCO Limited, 1985, "An Investigation of the Hydrodynamic Interaction of an Iceberg with a Gravity Based Offshore Structure", Report to National Research Council of Canada.

Odar, F. and Hamilton, W.S., 1964, "Forces on a Sphere Accelerating in a Viscous Fluid", Journal of Fluid Mechanics, No. 18, pp. 302-314.

Pawlowski, J.S., 1982, "The Estimation of Diffraction Force Components from the Equivalent Motion Concept", International Shipbuilding Progress, Vol. 29, March, pp. 62, 73.

Pawlowski, J.S., 1987, "Time Domain Simulation of Ship Motion in Waves by the Equivalent Motion Method", Institute for Marine Dynamics, National Research Council of Canada, Report IMD-HYD-01.

Salvaggio, M.A. and Rojansky, M., 1986, "The Importance of Wave-Driven Icebergs Impacting an Offshore Structure", Proceedings of Offshore Technology Conference, OTC '86, Vol. 1, pp. 29-38.

Sarpkaya, T. and Isaacson, M., 1981, "Mechanics of Wave Forces on Offshore Structures", Van Nostrand Reinhold Limited, 651 p.

Schoneborn, P.R., 1975, "Bewegung einzelner Partikeln im instationaren Stromungsfeld", Chem. Ing. Tech. 47,305.

Smith, S.D. and Banke, E.G., 1981, "A Numerical Model of Iceberg Drift", Proceedings of the 6th. International Conference on Port and Ocean Engineering Under Arctic Conditions, POAC '81, Vol. II, pp. 1001-1011.

Smith, S.D. and Banke, E.G., 1982, "The Influence of Winds, Currents and Towing Forces on the Drift of Icebergs", Cold Regions Science and Technology, Vol. 6, pp. 241-255.

Sodhi, D.S. and El-Tahan, M., 1980, "Prediction of an Iceberg Drift Trajectory During a Storm", Annals of Glaciology, Vol. 1, pp. 77-82.

Stansby, P.K. and Isaacson, M., 1987, "Recent Development in Offshore Hydrodynamics: Workshop Repeort", Journal of Applied Ocean Research, Vol. 9, No. 3, pp. 118-127.

Wehausen, J.V., 1971, "The Motion of Floating Bodies", Annual Reviews in Fluid Mechanics, Vol. 3, pp. 237-268.

Wiegel, R.L., 1964, "Oceanographical Engineering", Prentice-Hall, Inc.

Yeung, R.W., 1982, "Numerical Methods in Free-Surface Flows", Annual Reviews in Fluid Mechanics, Vol. 14, pp. 395-442.

Yum, D.J., 1985, "Nonlinear Flow Around Slightly Submerged Two Dimensional Bodies", Ph.D. dissertation, University of California, Berkeley, Department of Naval Architecture and Offshore Engineering.

Table 2.1 Motion and Force Parameters Calculated by Linear Diffraction Theory

WAVE			SURGE									HEAVE				
T sec	λ cm	H/λ -	a_{11} kg	b_{11} kg/sec	a_{15} kg	b_{15} kg/sec	RAO -	U_{max} cm/sec	$F_{F.K}$ N	F_{DIF} N	F_x N	a_{33} kg	b_{33} kg/sec	RAO -	V_{max} cm/sec	$2Z_a$ cm
.625	61	1/24	1.33	62.5	-.12	-5.6	.31	3.9	10.1	7.1	12.3	5.1	6.7	.086	1.1	.23
.625	61	1/11	1.33	62.5	-.12	-5.6	.31	8.5	22	15.6	26.7	5.1	6.7	.086	2.4	.49
.8	100	1/28	7.85	73.6	-.7	-6.6	.54	7.6	14.2	15.7	27.3	5.1	1	.106	1.5	.38
.8	100	1/19	7.85	73.6	-.7	-6.6	.54	11.4	21.2	23.6	41	5.1	1	.106	2.25	.57
.8	100	1/10	7.85	73.6	-.7	-6.6	.54	20.7	38.7	42.9	74.6	5.1	1	.106	4.1	1.0
1.0	156	1/30	12	29.8	-1.1	-2.7	.67	10.9	16.9	18.2	35	4.8	.1	.095	1.55	.52
1.0	156	1/20	12	29.8	-1.1	-2.7	.67	16.2	25	26.9	51.9	4.8	.1	.095	2.3	.77
1.0	156	1/10	12	29.8	-1.1	-2.7	.67	31.9	49.2	53	102	4.8	.1	.095	4.5	1.5
1.2	225	1/30	11.3	9.7	-1	-.87	.75	14.7	19.4	18.1	38.2	4.6	1	4.84	95	36.4
1.2	225	1/19	11.3	9.7	-1	-.87	.75	24	31.3	29.4	61.7	4.6	1	4.84	154	58.9
1.2	225	1/10	11.3	9.7	-1	-.87	.75	43.6	57.1	53.6	113	4.6	1	4.84	282	108
1.4	305	1/30	10.4	3.5	-.94	-.32	.81	18.8	20.9	17.6	40	4.6	1.5	1.67	38	17.3
1.4	305	1/20	10.4	3.5	-.94	-.32	.81	30.4	34.2	21.1	64.2	4.6	1.5	1.67	62.6	27.9
1.4	305	1/9	10.4	3.5	-.94	-.32	.81	60	67.6	38.4	127	4.6	1.5	1.67	124	55.2
1.6	393	1/31	9.8	1.4	-.88	-.13	.86	21.2	20.9	16.5	28.3	4.7	1.7	1.22	30	15.4
1.6	393	1/20	9.8	1.4	-.88	-.13	.86	32.7	32.4	25.5	44	4.7	1.7	1.22	47	23.8
1.9	545	1/30	9.3	.45	-.83	-.04	.92	27.4	23	17	37.3	4.8	1.5	1.08	32	11.5
1.9	545	1/20	9.3	.45	-.83	-.04	.92	40.9	34.2	25.3	53.6	4.8	1.5	1.08	48	29

Body Total Mass = 12.7 kg

Table 4.1 Measured and Computed Motions and Forces for the Towed Model

WAVE			MEASURED		COMPUTED	
T Sec	λ cm	H/λ –	Fx N	2Za cm	Fx N	2Za cm
.625	61	1/24	11.8	≈0	10.8	.2
.625	61	1/11	27	≈0	21.4	.4
.8	100	1/28	28	≈0	18.5	.3
.8	100	1/19	38.6	.53	28.7	.7
.8	100	1/10	53.9	1.19	56	1.9
1.0	156	1/46	22.5	≈0	15.3	3
1.0	156	1/30	34.3	≈0	24.3	3.5
1.0	156	1/20	47	.61	36.4	4.9
1.0	156	1/10	74.7	2	74.7	10.9
1.2	225	1/61	21.3	≈0	13.2	5
1.2	225	1/30	37.7	1.65	29.1	8.5
1.2	225	1/19	56	2.37	46.5	12.5
1.2	225	1/10	75.5	7.55	91	24
1.4	305	1/88	13	4.9	9.2	4.1
1.4	305	1/50	23.9	10.1	16.8	7
1.4	305	1/30	39.2	9.8	31	11
1.4	305	1/20	52.9	11.5	50.7	17
1.4	305	1/9	77.9	23.7	98	33.3
1.6	393	1/49	27	9.8	17.6	8.5
1.6	393	1/31	45	17.5	29	13
1.6	393	1/20	55	28	51	21
1.9	545	1/85	15.7	7.2	10.3	6.3
1.9	545	1/50	27	12.5	18.8	11
1.9	545	1/30	46.6	22	35	18
1.9	545	1/20	72.2	31	59	27

Table 4.2 Computed Force Components of the Towed Model

WAVE			F_{FK}		F_S		F_{dr}		Total Force	
T	λ	H/λ	[N]		[N]		[N]		F_X [N]	
sec	cm		−	+	−	+	−	+	−	+
.625	61	1/24	4.8	4.6	2.3	2.9	1	.1	5.5	5.3
.625	61	1/11	10.4	9.8	3.5	7.2	3.5	−	11.4	10
.8	100	1/28	7	7	6.7	7	1.9	.2	9.2	9.3
.8	100	1/19	10.5	10.5	9.5	11.1	2.8	−	15.4	13.3
.8	100	1/10	18.8	18.5	17	20	6.4	2.2	31	25
1	156	1/46	5.1	5.5	4.2	4.1	1.9	.8	7.8	7.5
1	156	1/30	8	8.5	8.5	8	2.6	2	12.6	11.7
1	156	1/20	11.8	12.2	11.7	10.5	5	2.5	20.8	15.7
1	156	1/10	23	24	22	21	9	8	40.4	34.3
1.2	225	1/61	4.6	4.7	4.3	3.1	1.3	.4	7.5	5.7
1.2	225	1/30	9	10	9.7	5.2	3.8	1.5	16.7	12
1.2	225	1/19	14	16	15	6.8	6	3	27.5	19
1.2	225	1/10	20	29	33	18	16.8	11	50.5	40.5
1.4	305	1/88	3.4	3.6	2.5	2	1.1	.3	5.1	4.1
1.4	305	1/50	6.2	6.2	5.1	3.1	1.6	.3	9.8	7
1.4	305	1/30	10.1	10.4	9.4	4.8	3.2	1.1	18.5	12.5
1.4	305	1/20	15.5	17	16	7.5	6	5.7	30.5	20
1.4	305	1/9	24	32	35.5	12.3	11	10	58	40
1.6	393	1/49	6.7	6.7	4.4	4.4	2	.3	10	7.6
1.6	393	1/31	9.5	10.5	7.5	7.2	3.2	.5	16.4	12.6
1.6	393	1/20	15	16	12	13	5	3.5	25	26
1.9	545	1/85	4	4	2.6	2.5	1.2	.5	5.8	4.5
1.9	545	1/50	6.9	7	4.6	4.6	1.8	.4	9.8	9
1.9	545	1/30	10.7	11.2	8.3	8.1	3.1	2.4	18.2	16.8
1.9	545	1/20	15.3	17.2	13	15	7.7	5.7	28	31

Table 4.3 Comparison of Measured and Computed Motions for Free Drifting Model with Wave Particle Velocities

WAVE			Free Drifting								Stokes 2nd Order			
			EXPERIMENT				COMPUTED				Particle Velocity			Particle
T sec	λ cm	H/λ -	U_{av} cm/sec	U_{max} cm/sec	V_{max} cm/sec	$2Z_A$ cm	U_{av} cm/sec	U_{max} cm/sec	V_{max} cm/sec	$2Z_A$ cm	Uav cm/sec	Umax cm/sec	Vmax cm/sec	-Like Motion
.625	61	1/24	4.7	≈ 4.7	≈1	≈0	4.6	8.6	1	0.2	1.6	14.3	12.7	NO
.625	61	1/11	13.7	≈13.7	≈1	≈0	13.6	22	2	0.4	7.8	35.3	27.5	NO
.8	100	1/28	≈2.0	NA	≈0	≈0	2.4	9	1	0.3	1.6	15.7	14.1	NO
.8	100	1/19	6.0	NA	NA	≈1.0	5.8	16	2.5	0.7	3.6	24.9	21.2	NO
.8	100	1/10	11.4	27	NA	2.7	11.3	30	7.7	2	11.9	50.4	38.5	NO
1.0	156	1/30	2.5	NA	NA	≈1	2.1	12	13	3.8	1.7	18	16.3	NO
1.0	156	1/20	6.0	25	NA	1.3	4.5	19	17	4.6	3.8	28	24	NO
1.0	156	1/10	8.6	41	22	7.0	8.7	36	28	8	14.6	62.4	47.7	NO
1.2	225	1/30	3.6	15	NA	1.7	2.6	15.9	28.5	10.2	2.1	21.7	19.6	NO
1.2	225	1/19	6.5	30	10	5.6	4.6	27	44	16	4.6	33.9	29.3	NO
1.2	225	1/10	6.8	32	≈18	NA	9	47	63	21.7	18	76.2	58.2	NO
1.4	305	1/30	5.4	22	23	5.1	2.3	19.7	27.5	12.5	2.5	25.9	23.3	NO
1.4	305	1/20	5.7	NA	NA	NA	4.2	31	44	19.5	6.5	44	37.5	NO
1.4	305	1/9	7.9	NA	NA	≈7.1	14	63	69	35	25.2	99.4	74	NO
1.6	393	1/31	6.5	28	≈26	10.5	2.9	24	26	13	2.5	27.4	24.7	YES
1.6	393	1/20	6.8	47	39	14.8	6.4	39.2	40	20.5	6.0	44.6	38.3	YES
1.9	545	1/30	4.9	33	32	19.2	3	31	31	18.5	3.3	34.3	30	YES
1.9	545	1/20	9.6	50	50	30.4	8.3	48	46	28	7.1	53.4	44.5	YES

Table 4.4 Computed Force Components of the Free Drifting Model

WAVE			SURGE FORCES [N]								HEAVE FORCES [N]							
T	λ	H/λ	F_{FK}		F_S		F_{dr}		Total		F_{FK}		F_S		F_{dr}		Total	
sec	cm	–	–	+	–	+	–	+	–	+	–	+	–	+	–	+	–	+
.625	61	1/24	4.7	4.9	.4	1.1	.8	.04	4.7	4.9	1	1.1	.2	.16	.16	.2	.7	1.1
.625	61	1/11	10.4	10.5	4.9	5	3.2	–	9.9	8.9	1.2	2.1	.7	.65	.74	.67	1.7	2.1
.8	100	1/28	7	7.1	.9	1.1	.4	.12	6.7	6.4	1.1	.9	1.4	1.8	1.4	1.4	1.3	1.3
.8	100	1/19	10.5	10.6	1	2.5	1.2	.1	9.9	9.6	1	1.9	1.9	2.9	2.1	1.8	1.9	2.8
.8	100	1/10	18.8	18.8	2.2	3	4.4	.2	23.2	23.2	5.5	5.1	2.8	5.2	4	3.9	6	7.9
1	156	1/30	8	8.5	1	1	.6	.1	7.3	8	9.2	7.7	3.3	4.5	2.5	3.6	9.8	9
1	156	1/20	12	12.4	2.8	2.2	1.4	.1	10.8	11.4	11.7	10.4	3.8	6.6	4.7	5.2	13.2	11.5
1	156	1/10	23.3	23.9	3	2.6	2.6	.5	21.7	21.5	15.7	17.6	5.4	10.5	5.1	8.5	17.5	21.1
1.2	225	1/30	8.8	9.8	.8	.7	3.6	.1	9	9	19.1	16.3	4	5.5	3.4	4	20	18.3
1.2	225	1/19	13.4	15.5	2.2	1.8	1.1	.4	14.6	14.6	30.3	24.6	6.4	10	5.5	8.1	30	30
1.2	225	1/10	23.5	26.5	3.5	3	1.8	2.8	21.4	25.2	38	35.7	8.8	16	7.4	15	42	42
1.4	305	1/30	10.3	10.8	1	1.1	.35	.13	10.3	10.2	15.6	15	2.2	2.7	1.6	2.2	16.5	15.5
1.4	305	1/20	16.4	17.5	3	2.2	.6	.8	16.6	16.3	25.6	24.5	3.8	4.9	2.7	3.5	26.8	25
1.4	305	1/9	32.6	34.7	3.1	2.4	2	5	36	36	37.8	39	5.3	5.5	3.5	3.8	41	41
1.6	393	1/31	10.1	10.5	.3	.2	.22	.02	10.4	10.2	12.6	13.2	1.4	1.3	1.1	1.2	12.8	13.4
1.6	393	1/20	15.9	16.4	.54	.4	.4	.03	16.2	15.8	18.8	19.8	2.3	1.9	1.3	2	18.9	20.5
1.9	545	1/30	11.2	11.5	.2	.18	.11	.04	11.3	11.3	12.2	13.5	1.1	.86	.46	.66	12.1	13.5
1.9	545	1/20	16.9	17.2	.14	.34	.3	.06	17.3	17	17.6	19.3	1.5	1.1	.6	1	17.7	19.4

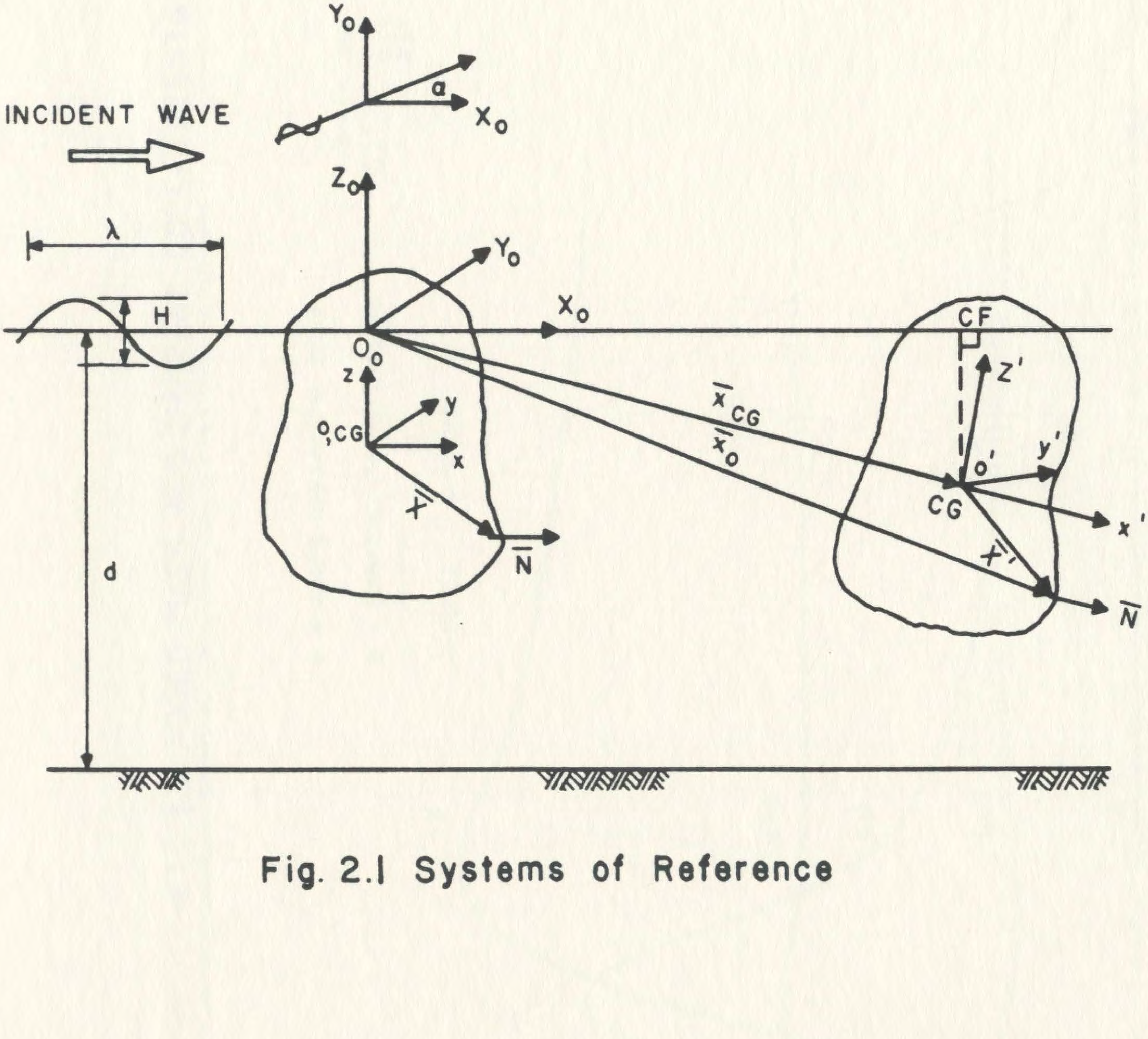

Fig. 2.1 Systems of Reference

FIG.2.2 ADDED MASS AND DAMPING COEFFICIENTS

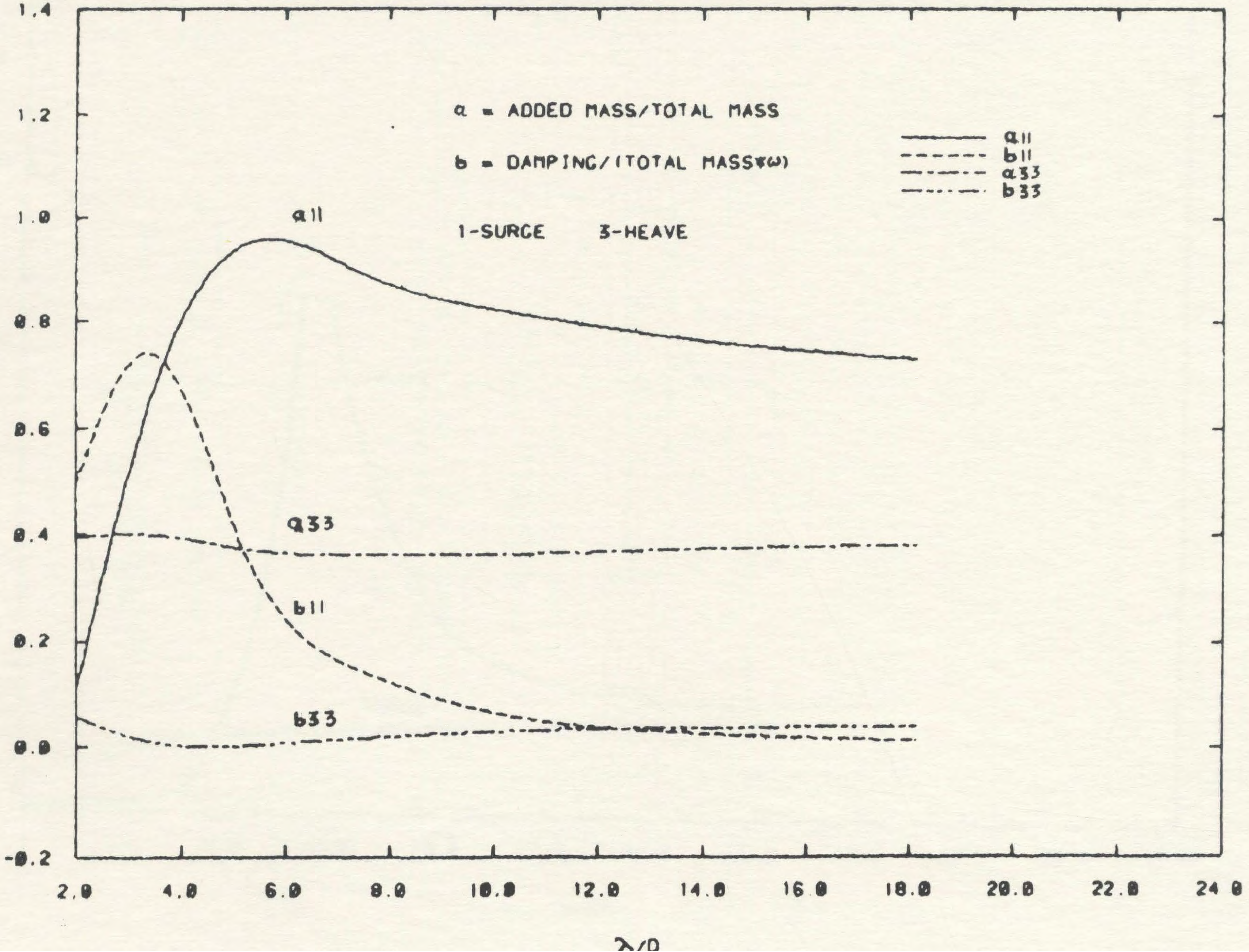

FIG.2.3 RESPONSE AMPLITUDE OPERATOR

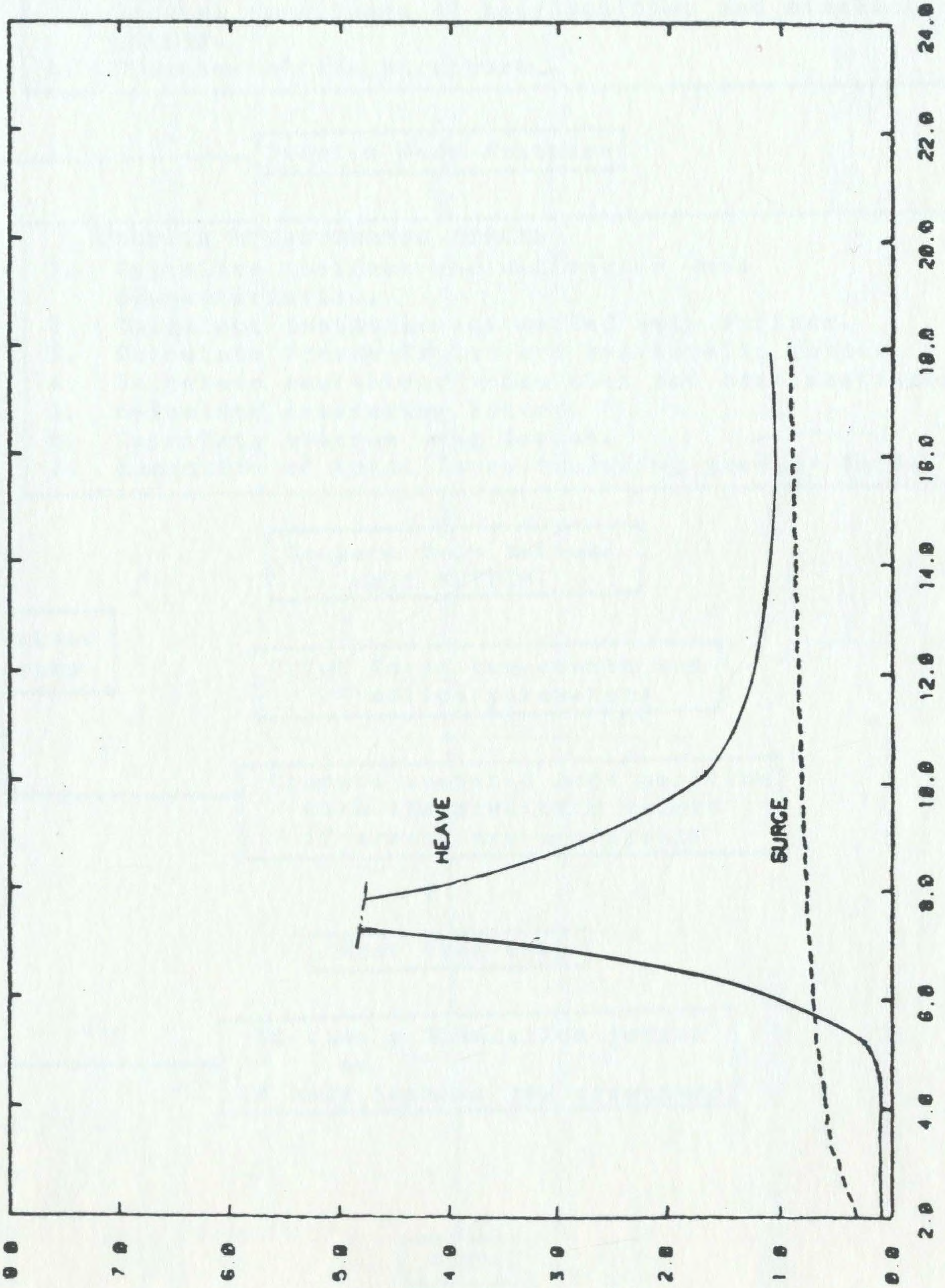

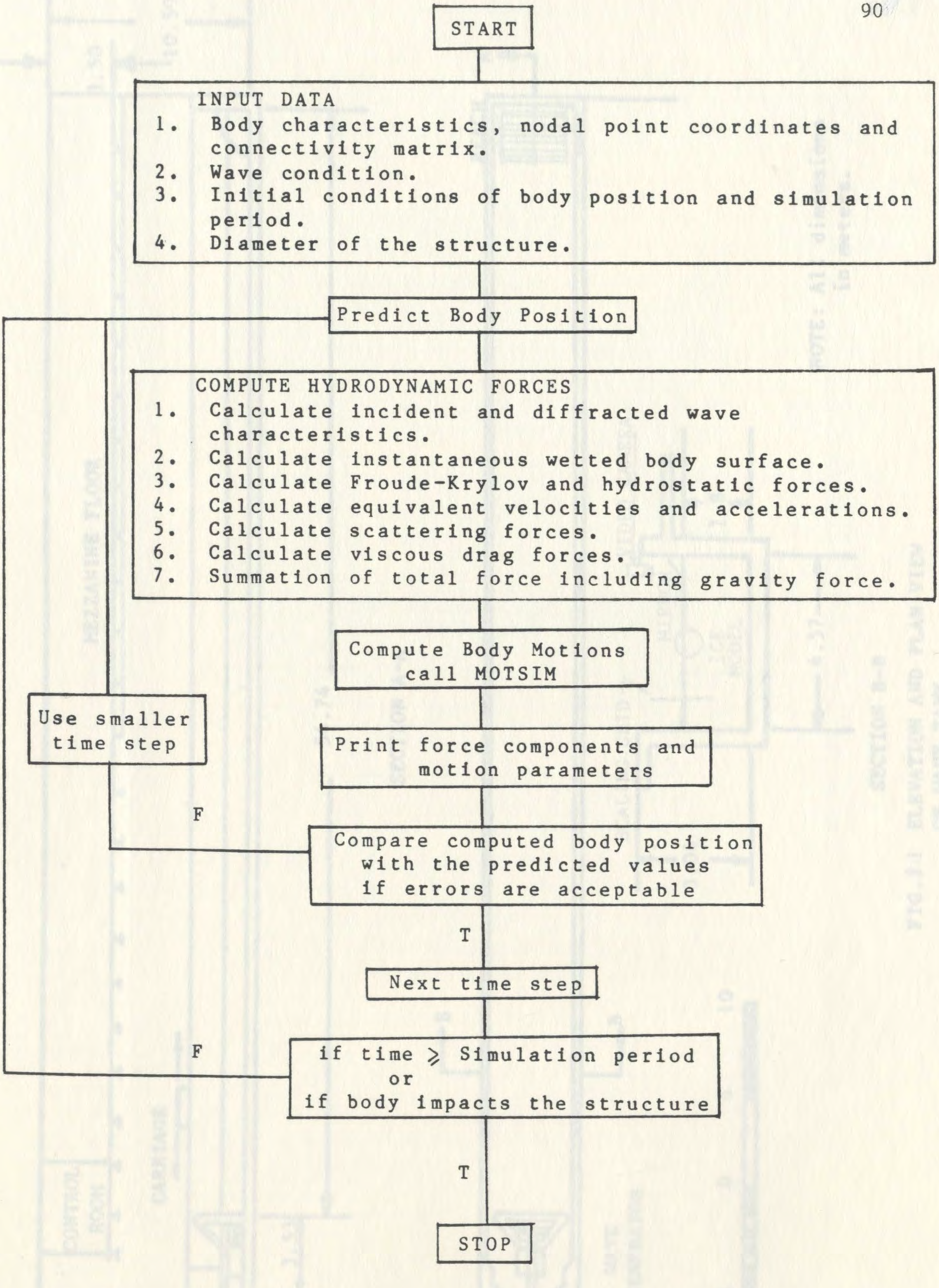

Figure 2.4 Flow Chart

SECTION A-A

SECTION B-B

NOTE: All dimensions in meters.

FIG.3.1 ELEVATION AND PLAN VIEW OF WAVE TANK

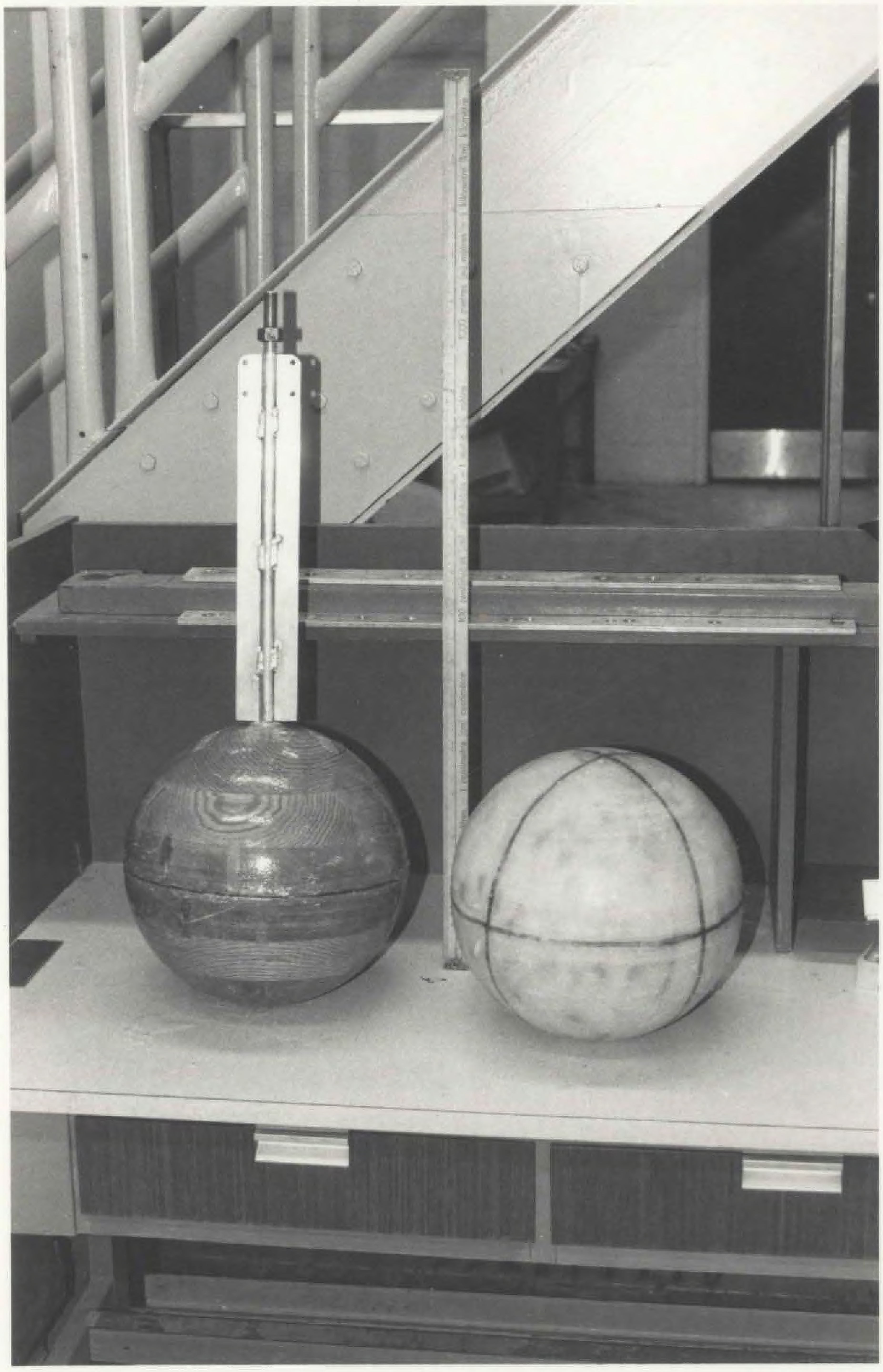

Figure 3.2 Ice Models

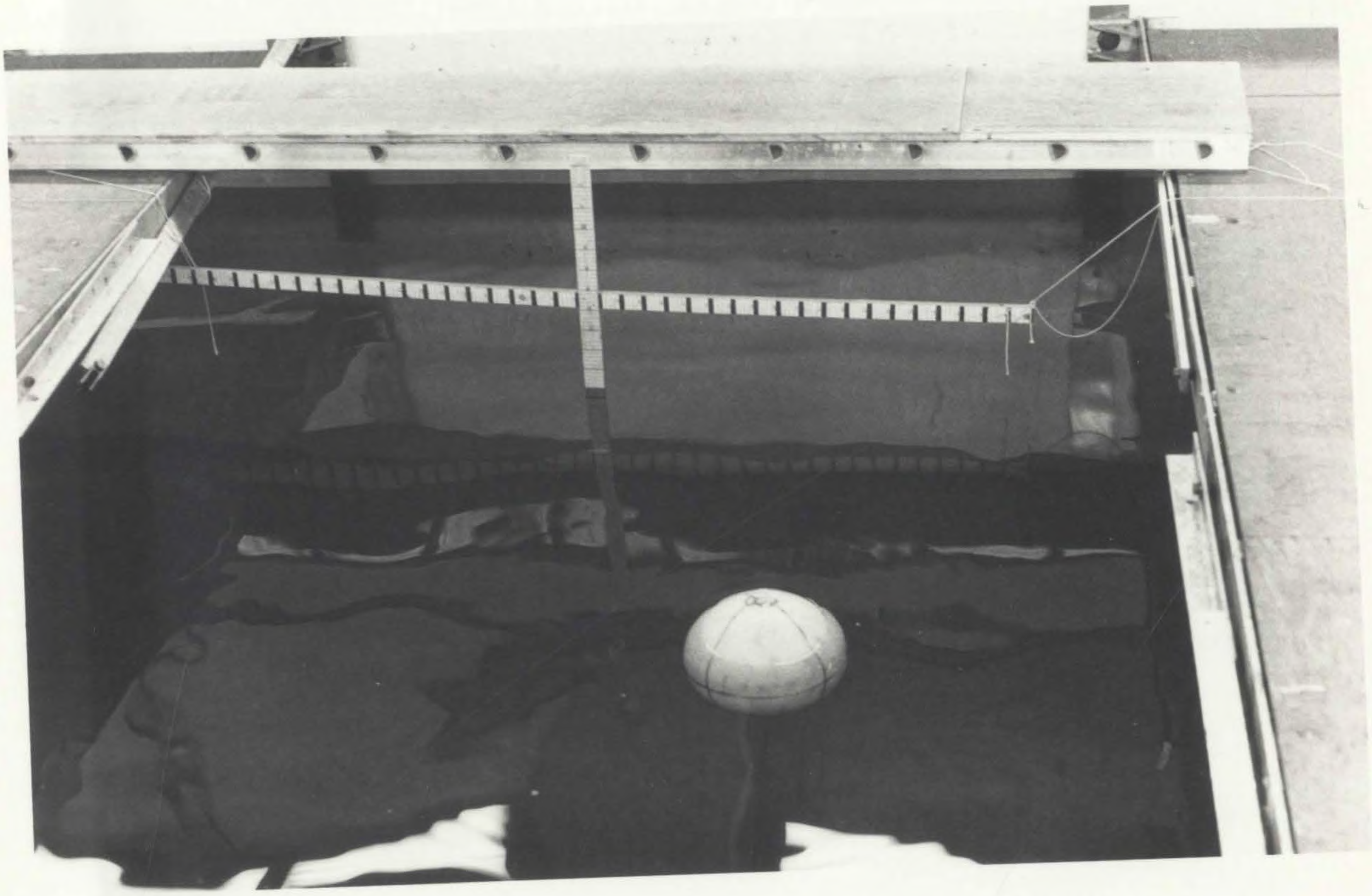

Figure 3.3 Free Drifting
Model Test

Figure 3.4 Towed Model Test

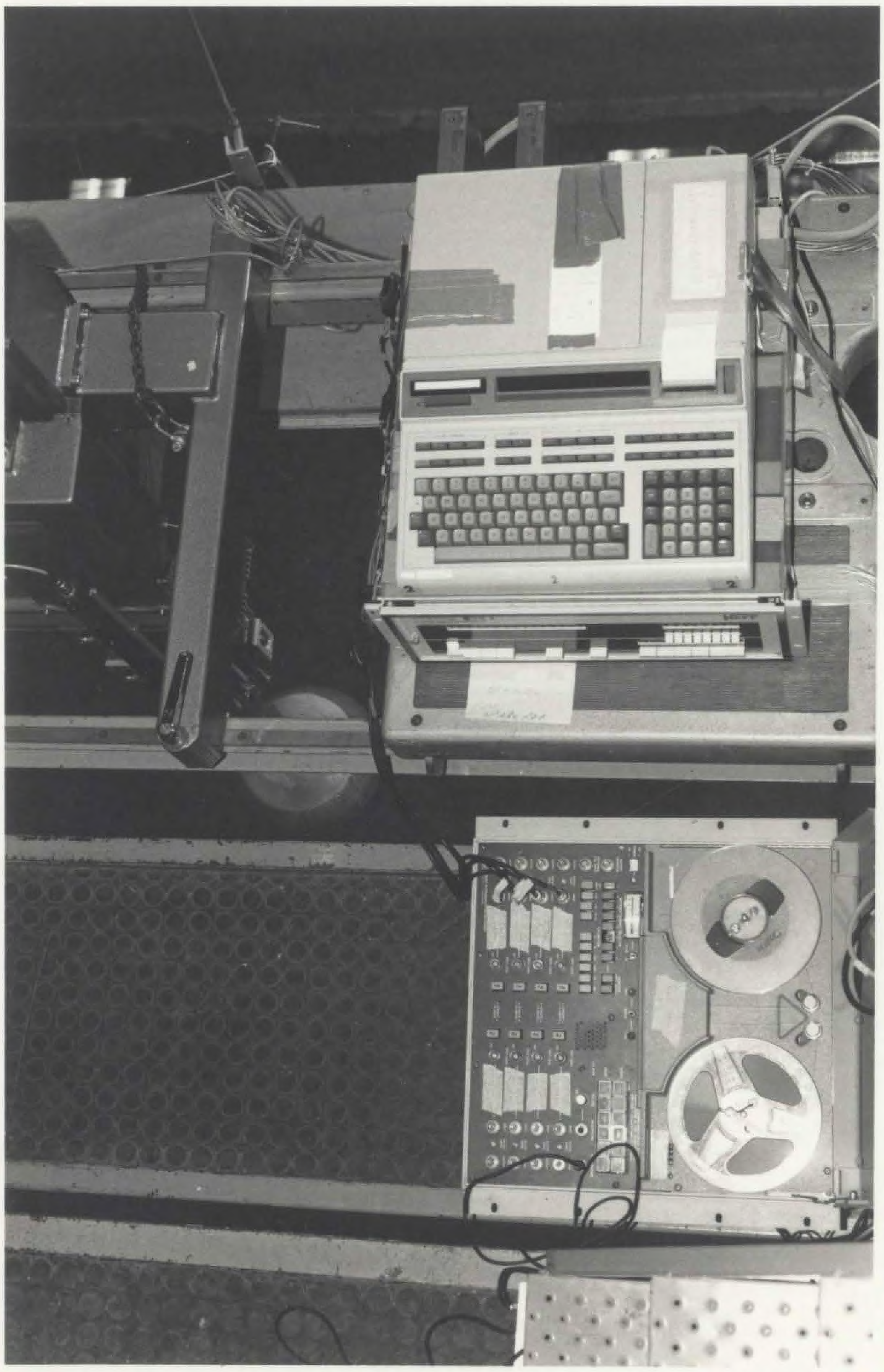

Figure 3.5 Data Acquisition System

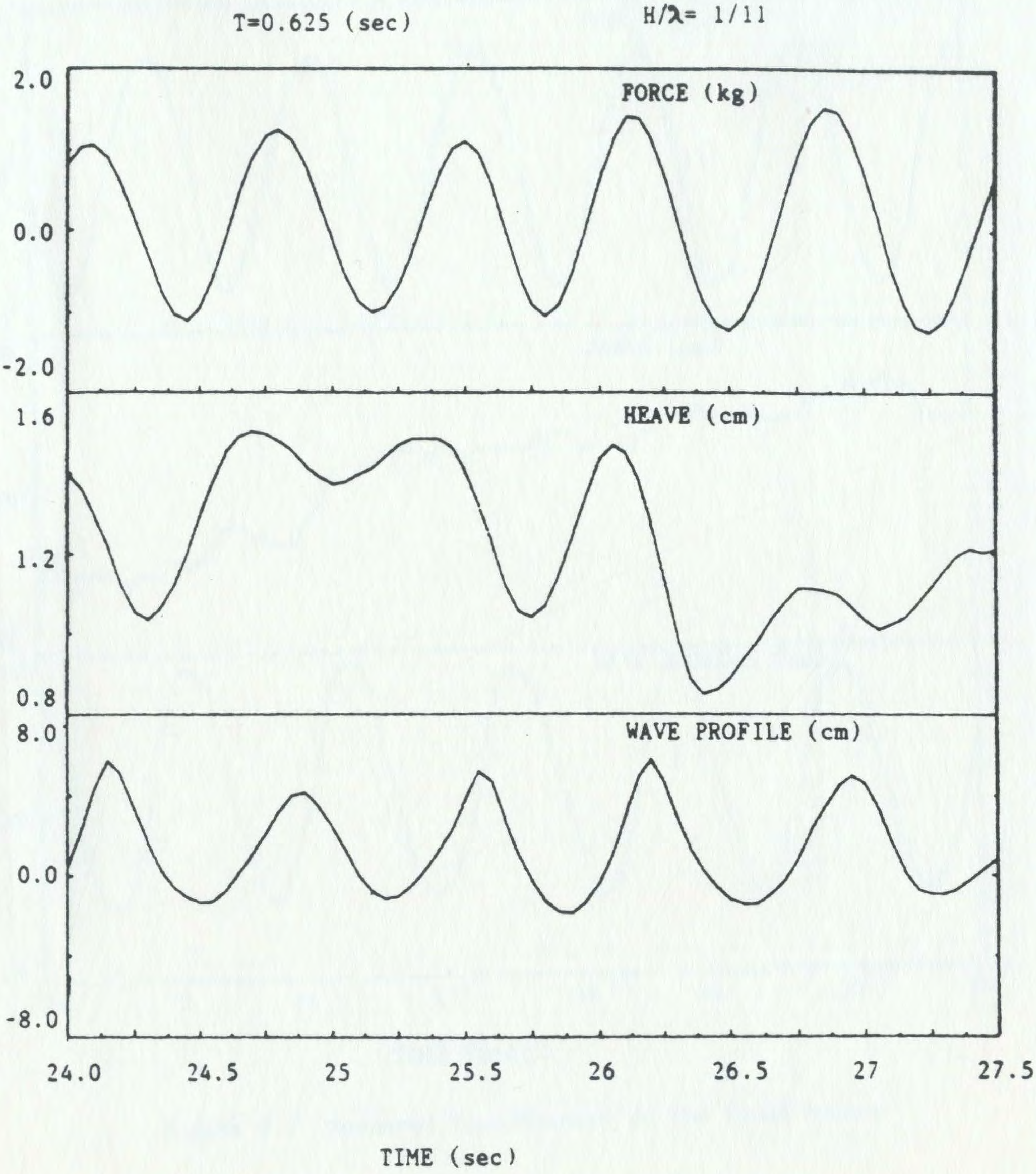

Figure 3.6 Measured Time-History of the Towed Sphere

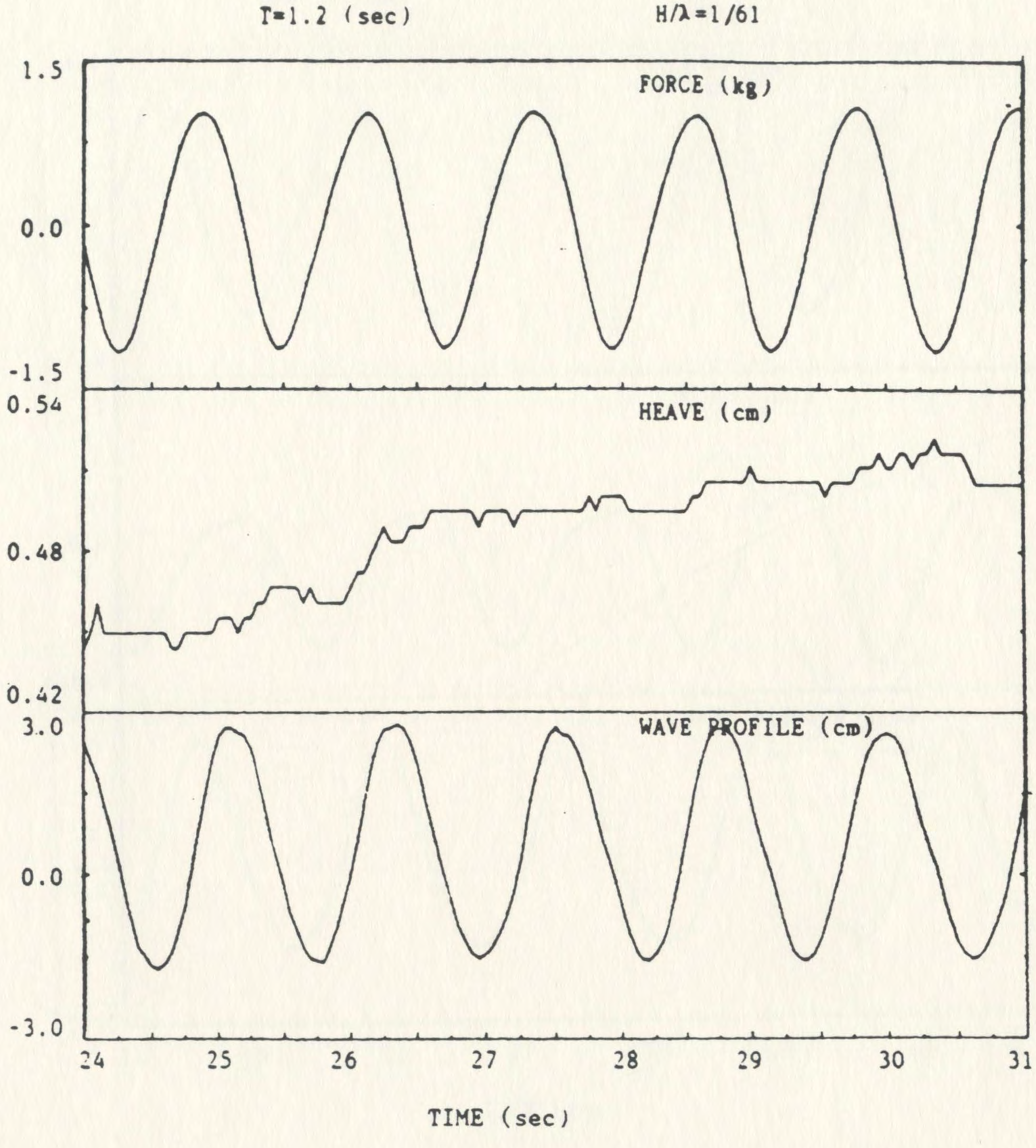

Figure 3.7 Measured Time-History of the Towed Sphere

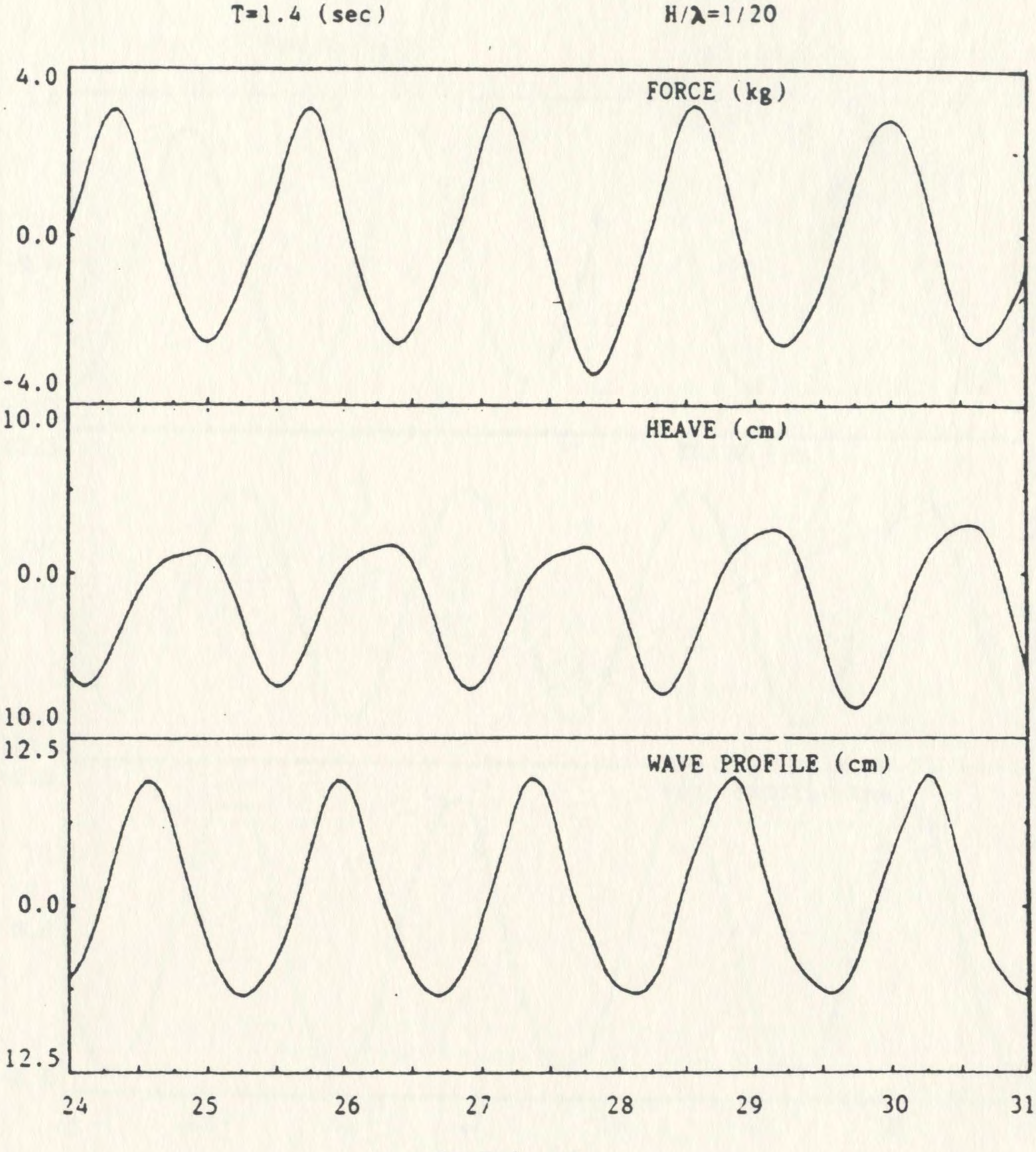

Figure 3.8 Measured Time-History of the Towed Sphere

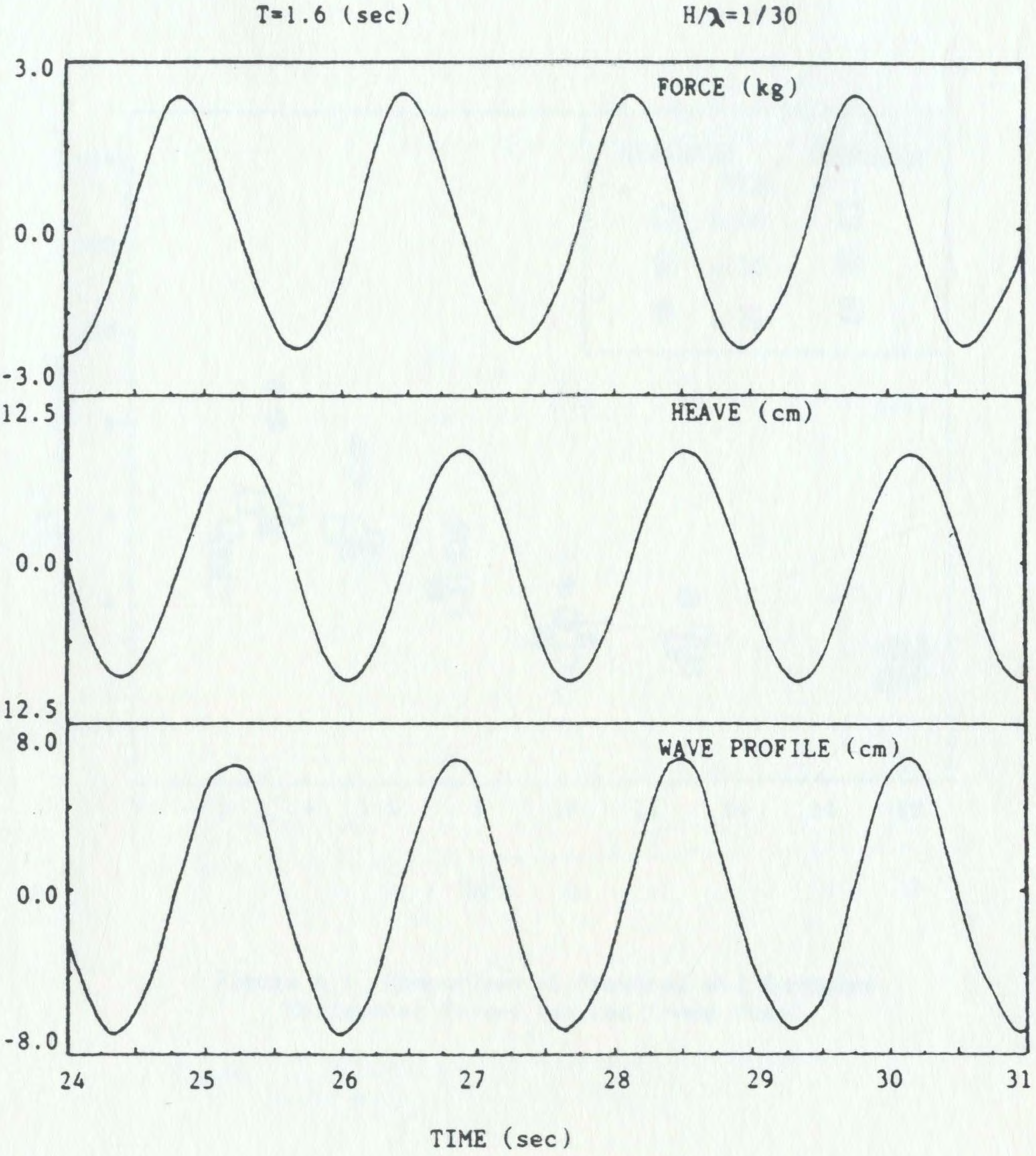

Figure 3.9 Measured Time-History of the Towed Sphere

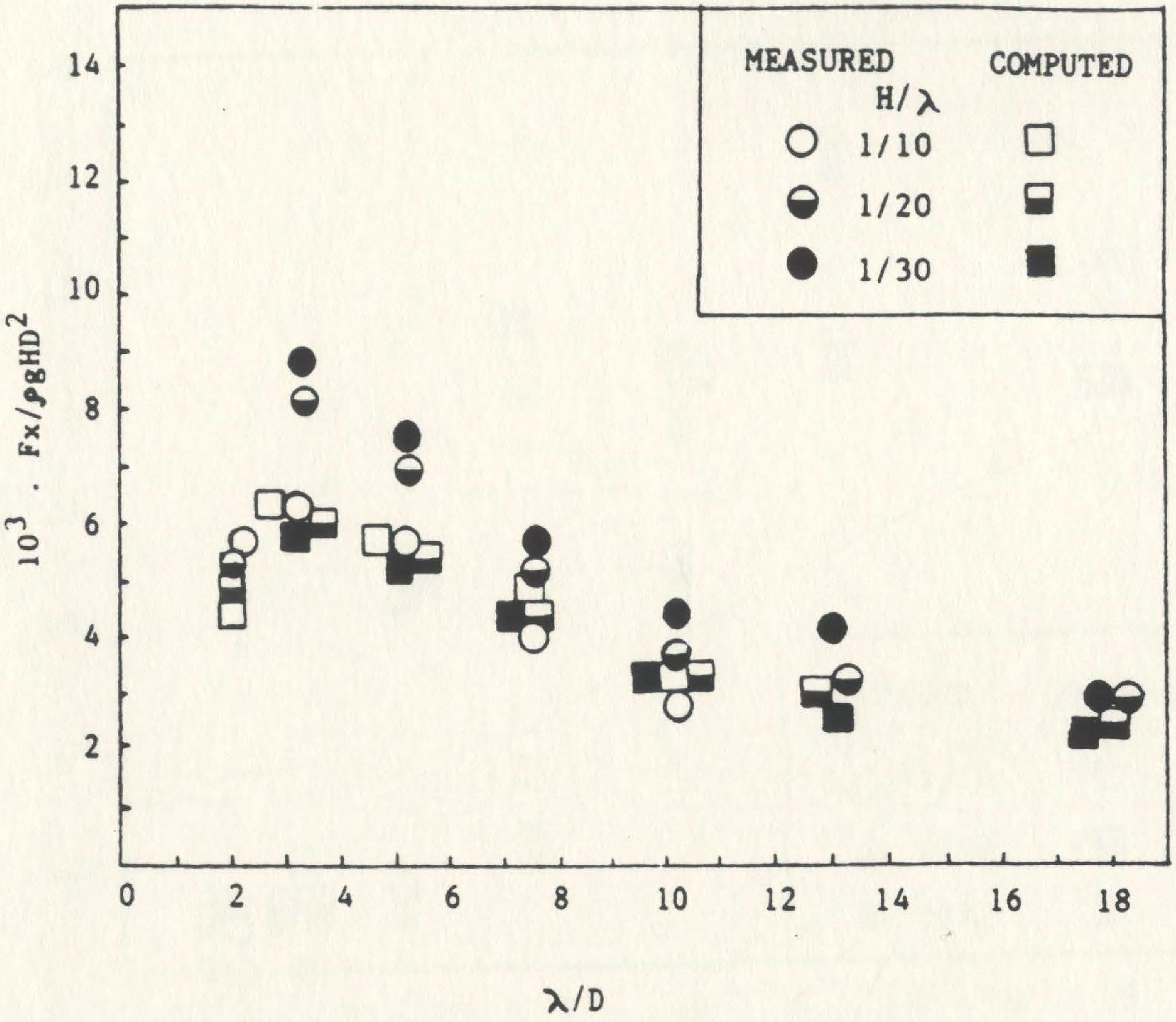

Figure 4.1 Comparison of Measured and Computed Horizontal Forces for the Towed Model

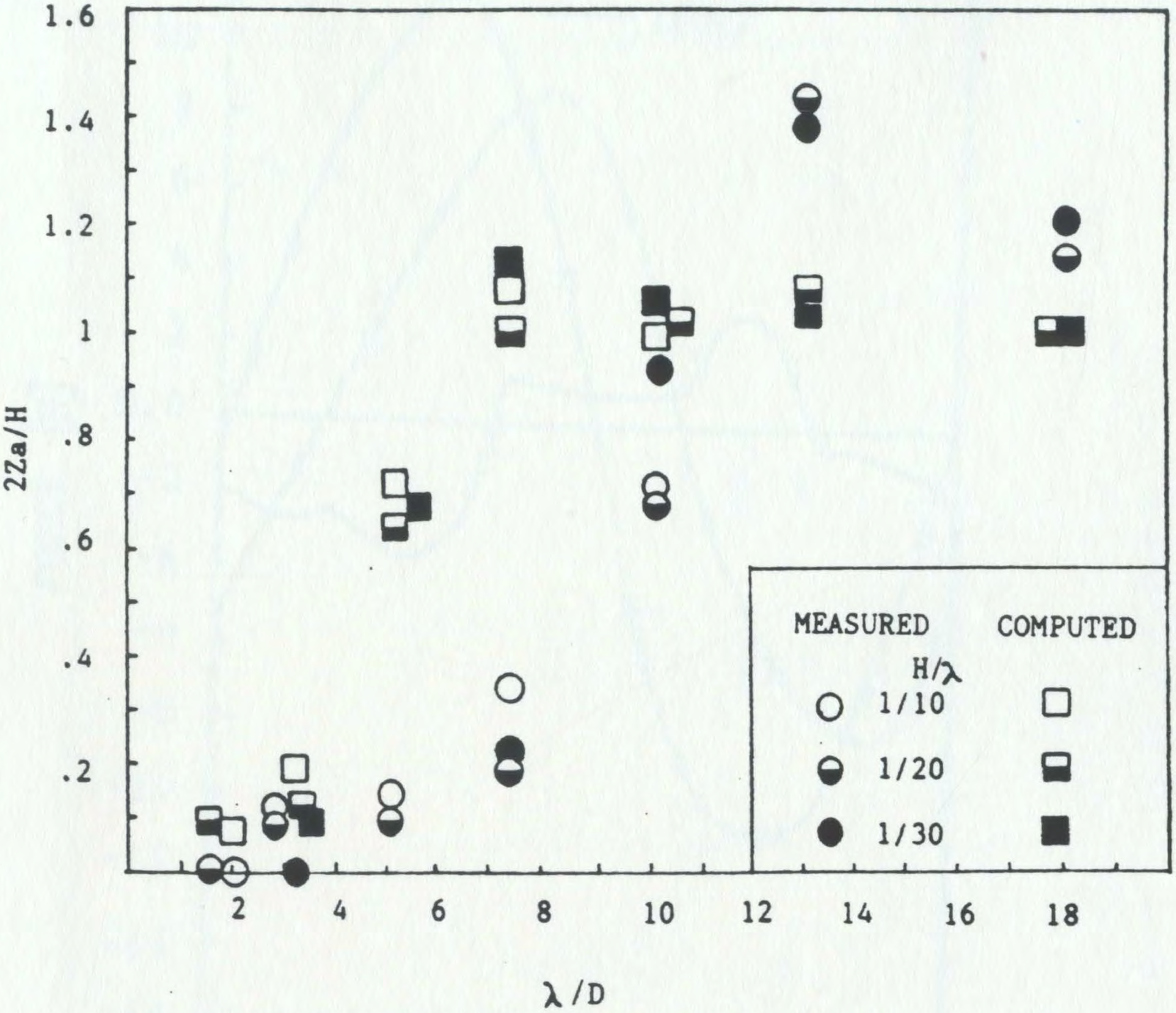

Figure 4.2 Comparison of Measured and Computed Heave Motions for the Towed Model

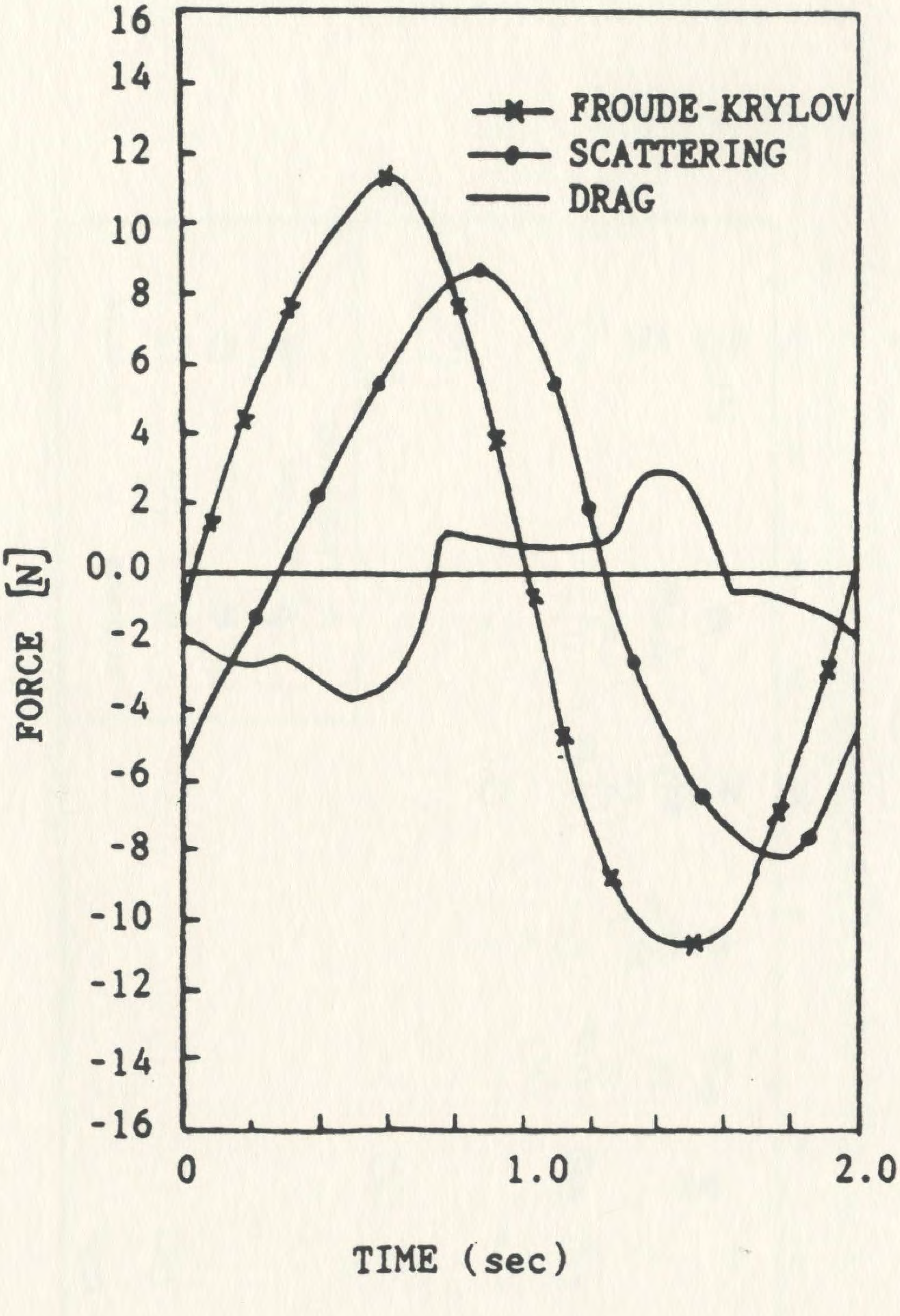

Figure 4.3 Time-History of the Computed Force Components in Surge Direction for the Towed Model

T = 1.9 sec , $H/\lambda = 1/30$

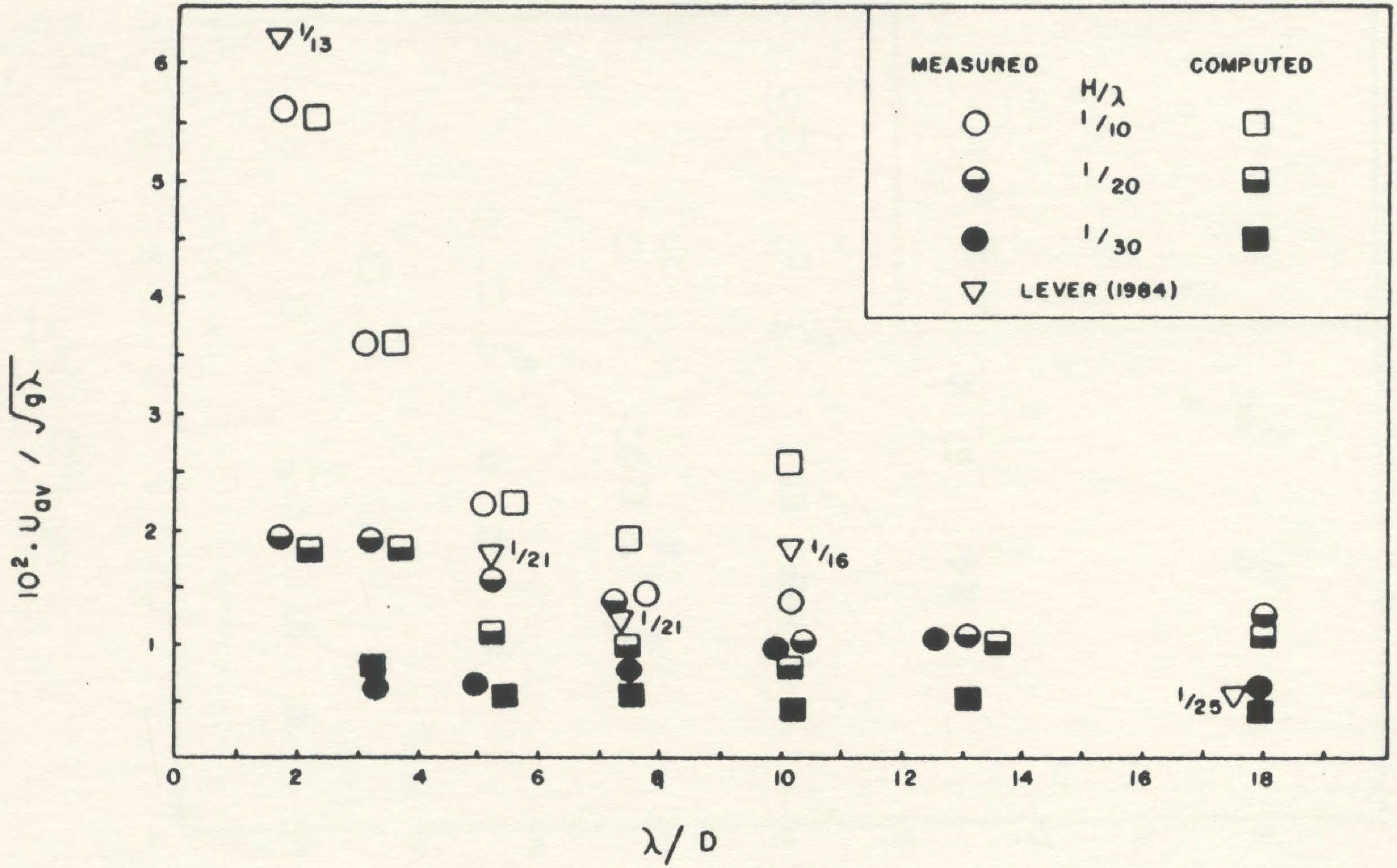

Figure 4.4 Comparison of Measured and Computed Average Drift Speed

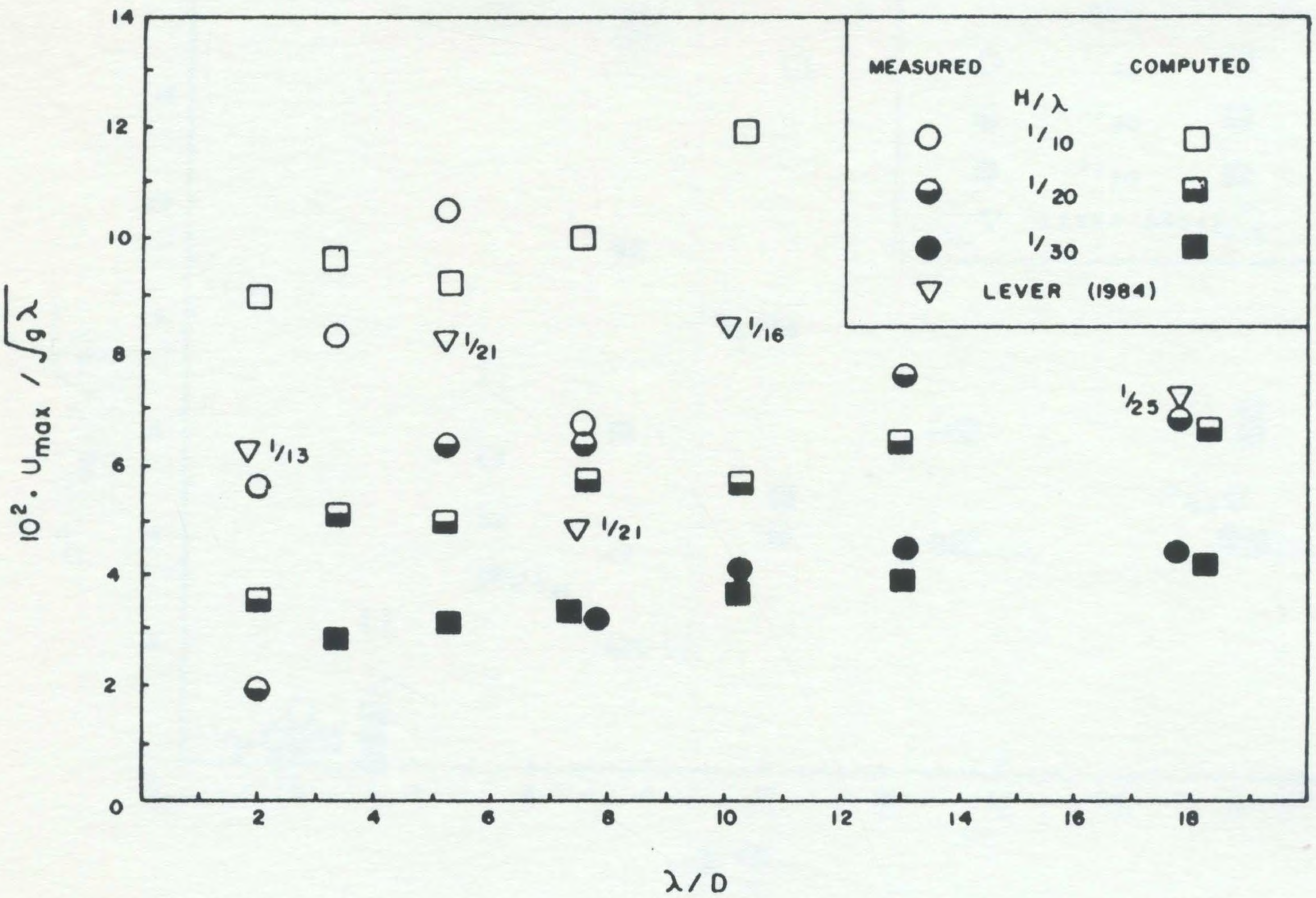

Figure 4.5 Comparison of Measured and Computed Maximum Velocity in Surge Mode

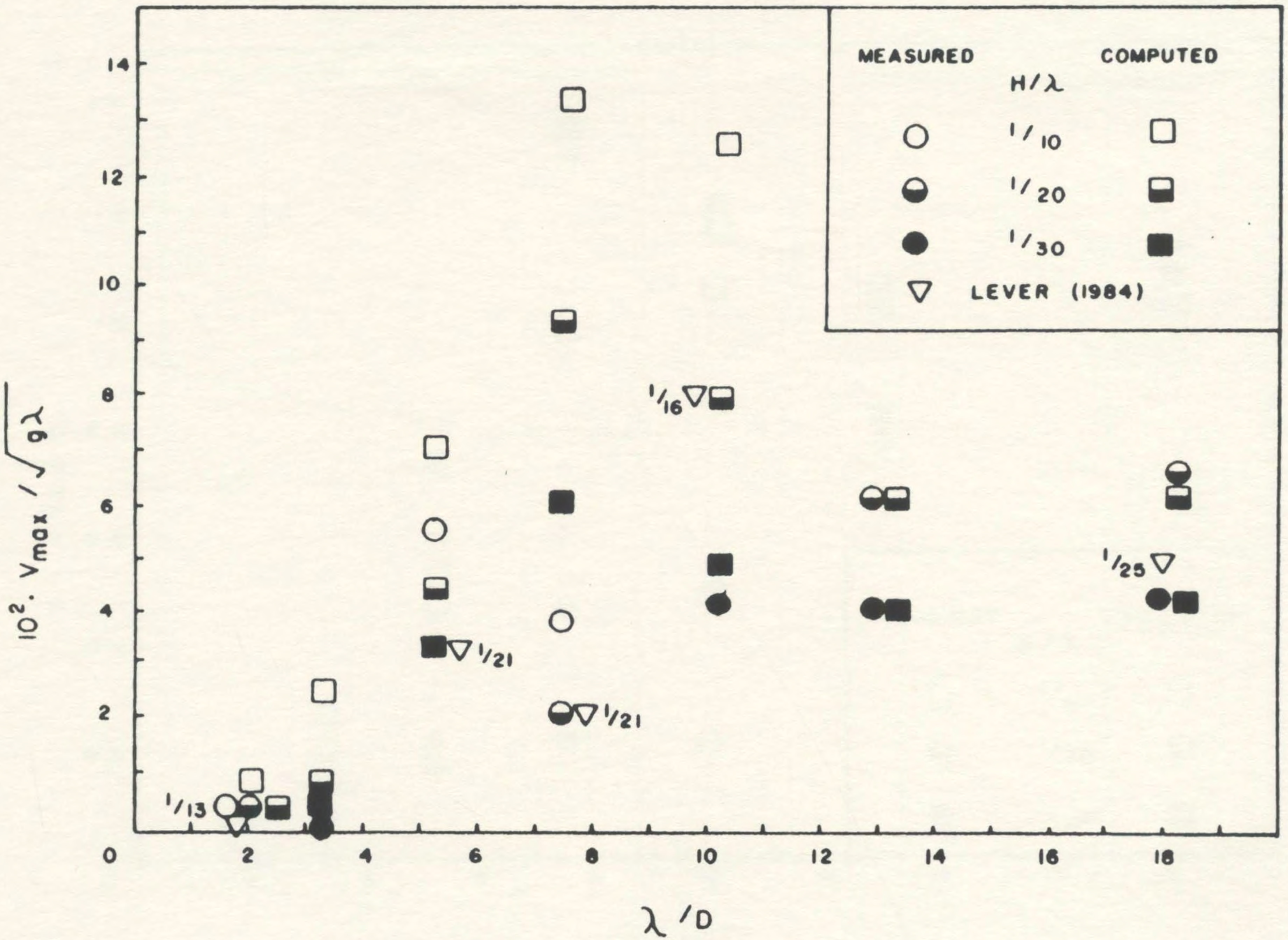

Figure 4.6 Comparison of Measured and Computed Maximum Velocity in Heave Mode

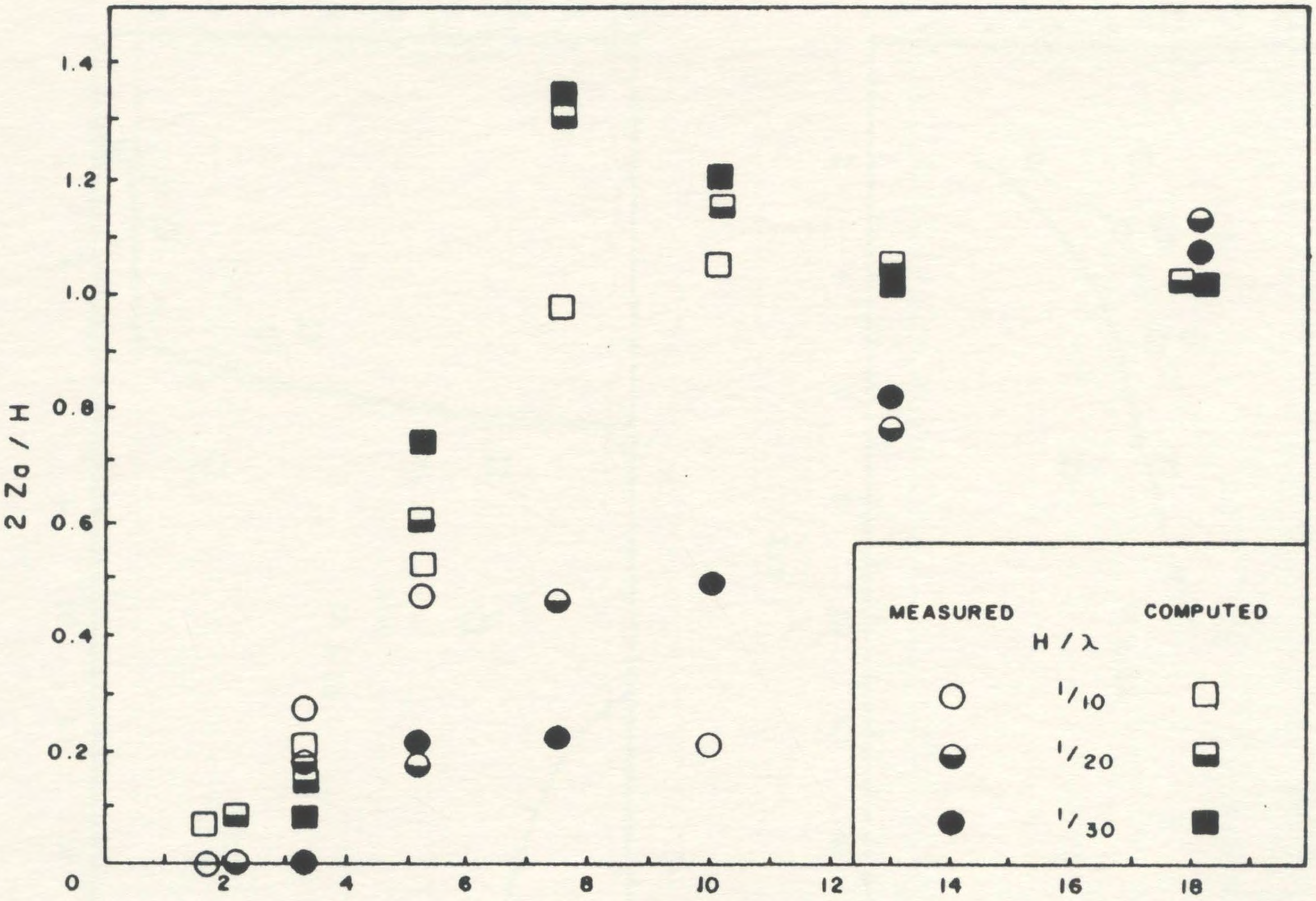

Figure 4.7 Comparison of Measured and Computed Heave Heights

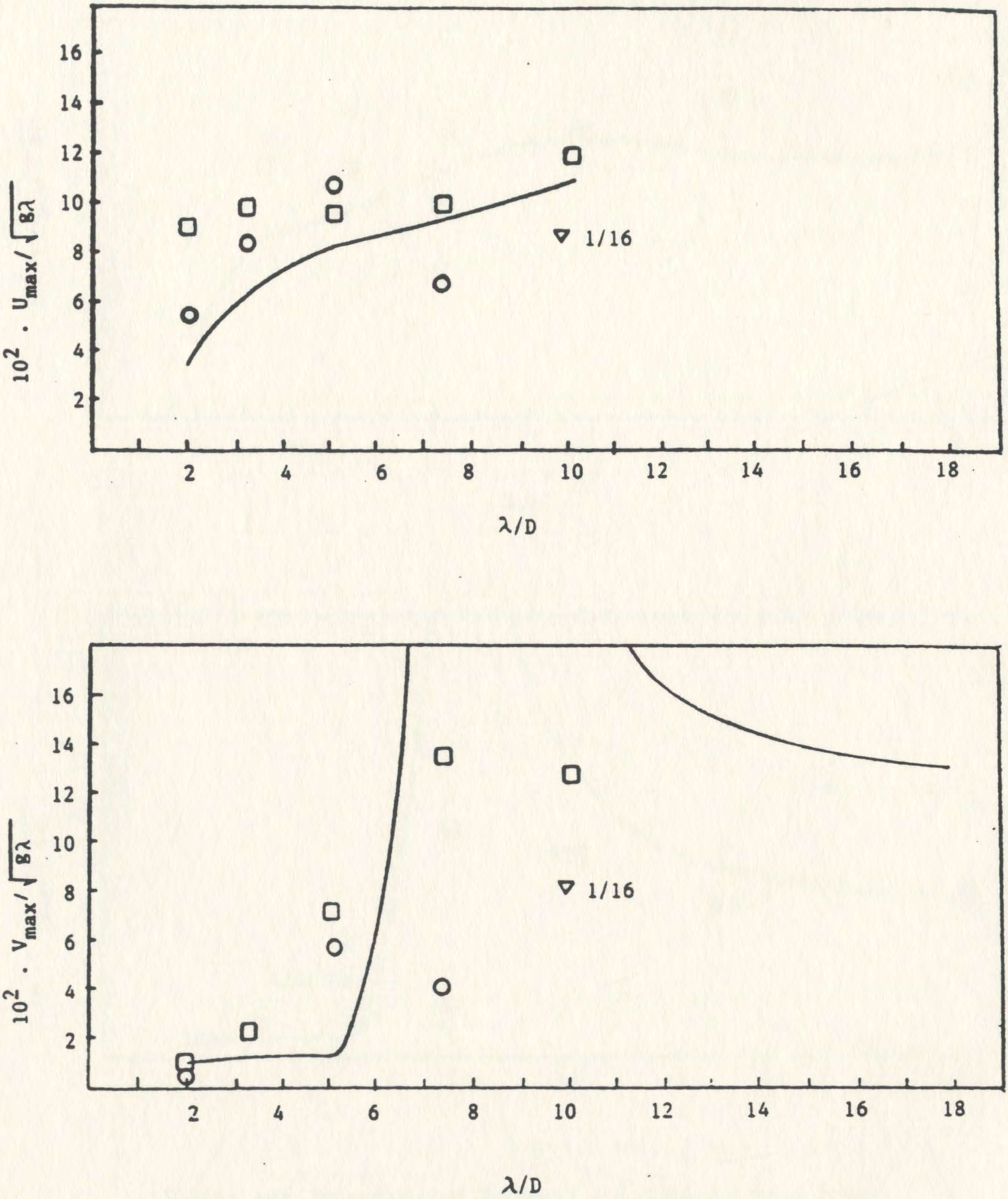

Figure 4.8 Comparison of Measured and Computed Velocities Versus Linear Diffraction Theory Results for $H/\lambda = 1/10$

○ Measured ☐ Present Computation

— Linear Diffraction Theory ▽ Lever (1984)

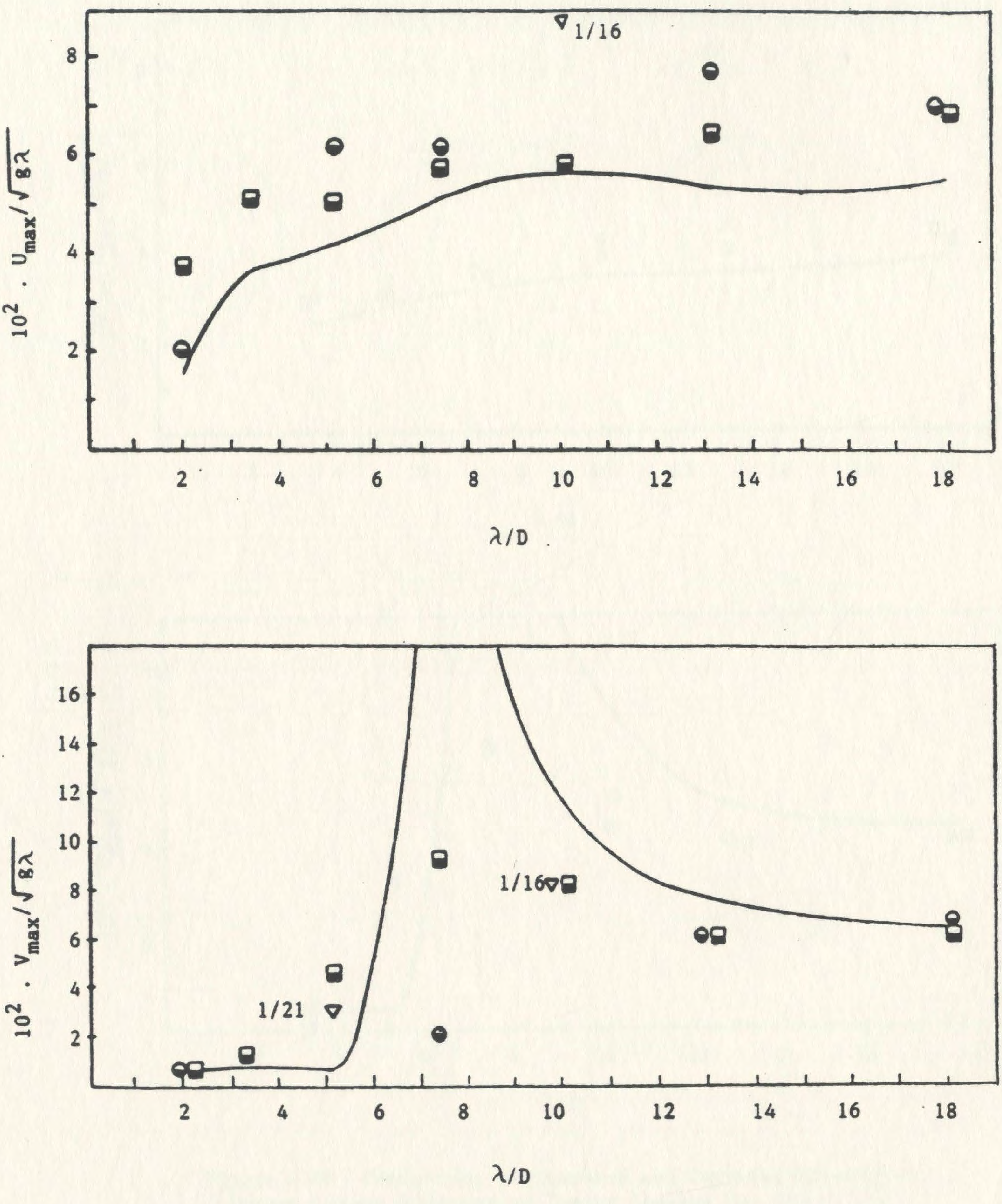

Figure 4.9 Comparison of Measured and Computed Velocities Versus Linear Diffraction Theory Results for $H/\lambda = 1/20$

◒ Measured

▣ Present Computation

— Linear Diffraction Theory

▽ Lever (1984)

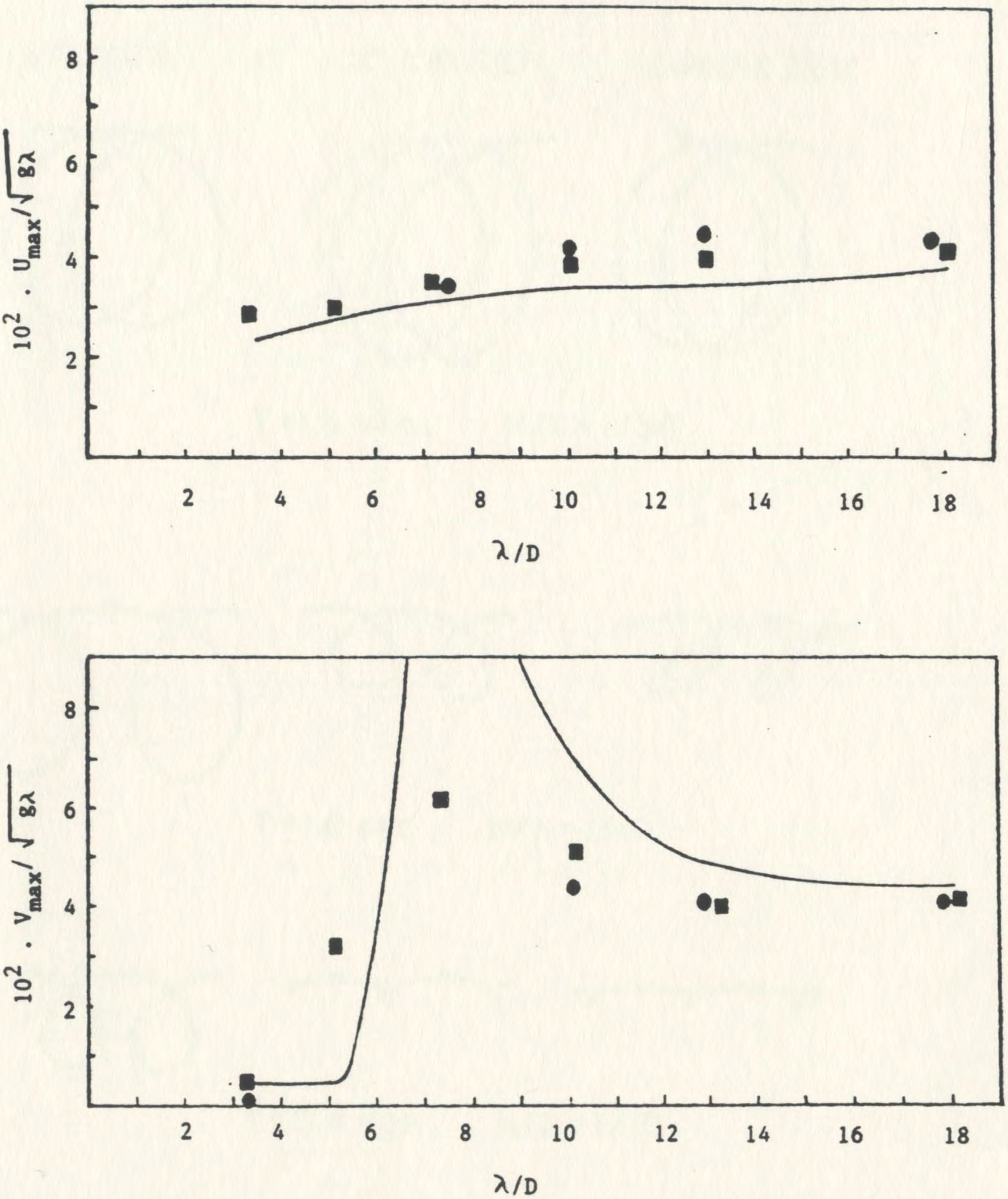

Figure 4.10 Comparison of Measured and Computed Velocities Versus Linear Diffraction Theory Results for $H/\lambda = 1/30$

● Measured

■ Present Computation

— Linear Diffraction Theory

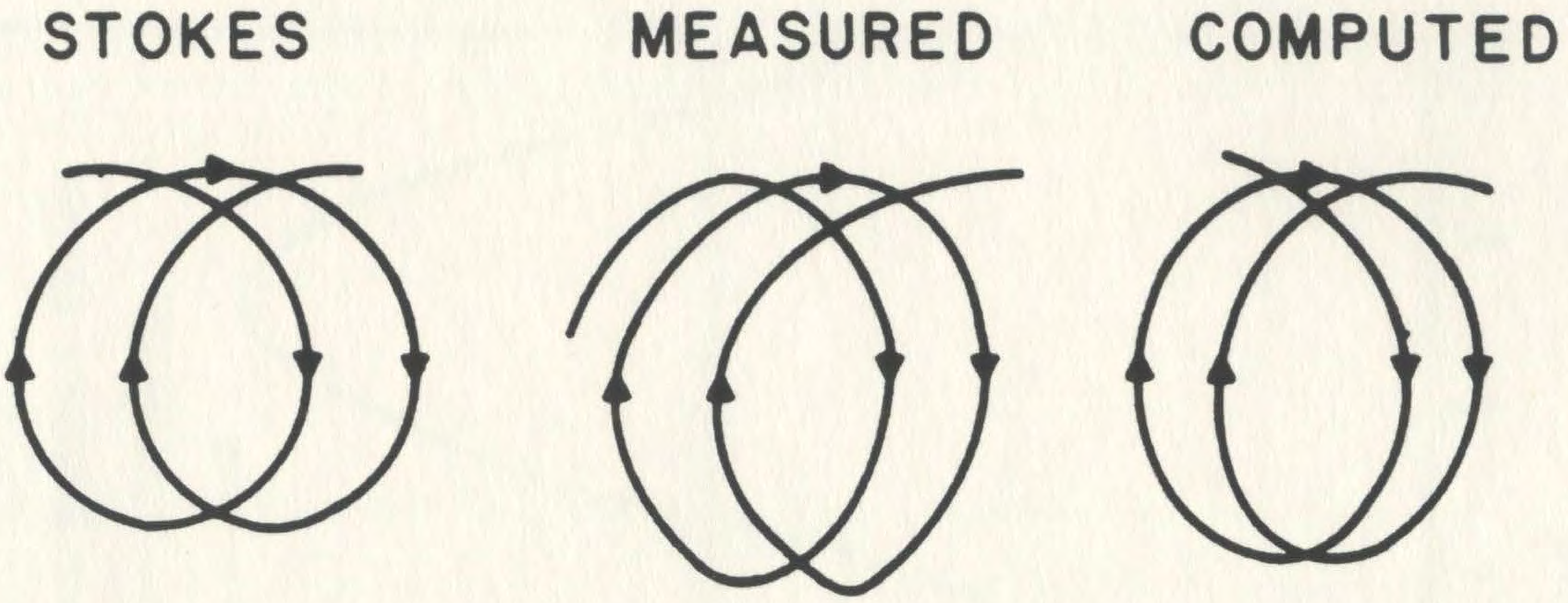

T=1.9 sec, H/λ=1/30

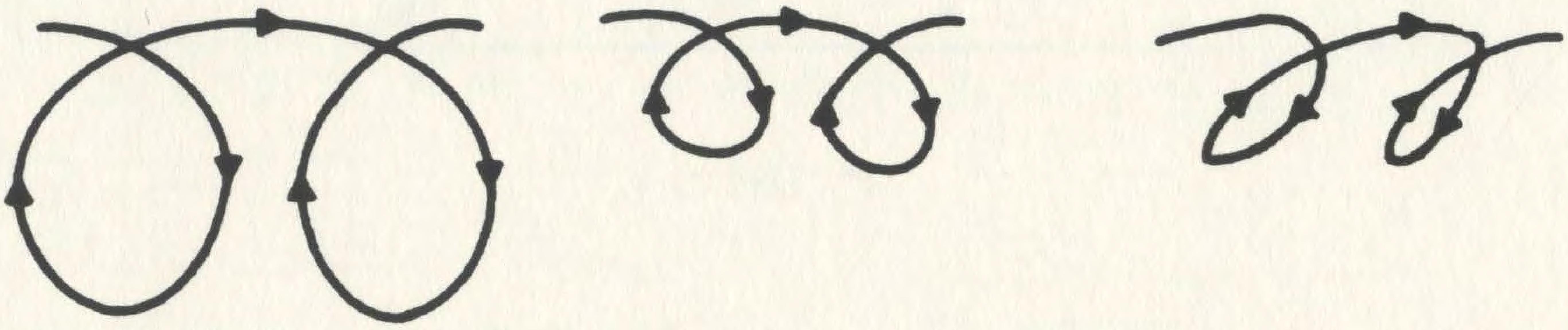

T=1.0 sec, H/λ=1/10

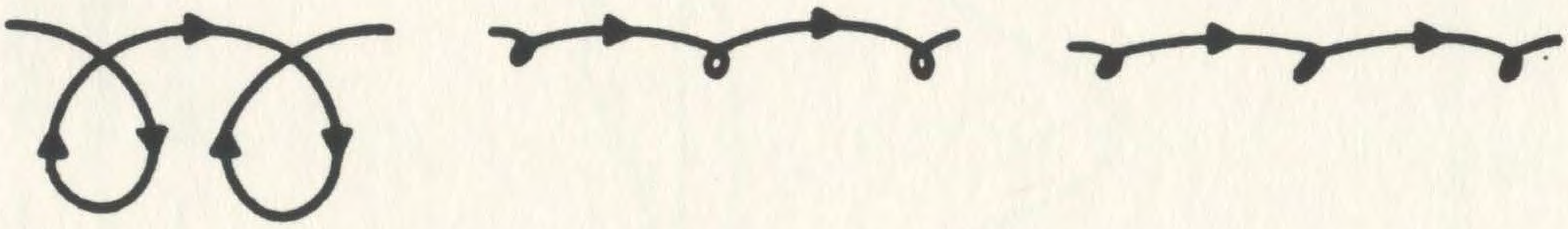

T=0.8 sec, H/λ=1/10

Fig. 4.11 Comparison of observed and computed motions of free floating sphere with the corresponding particle motions.

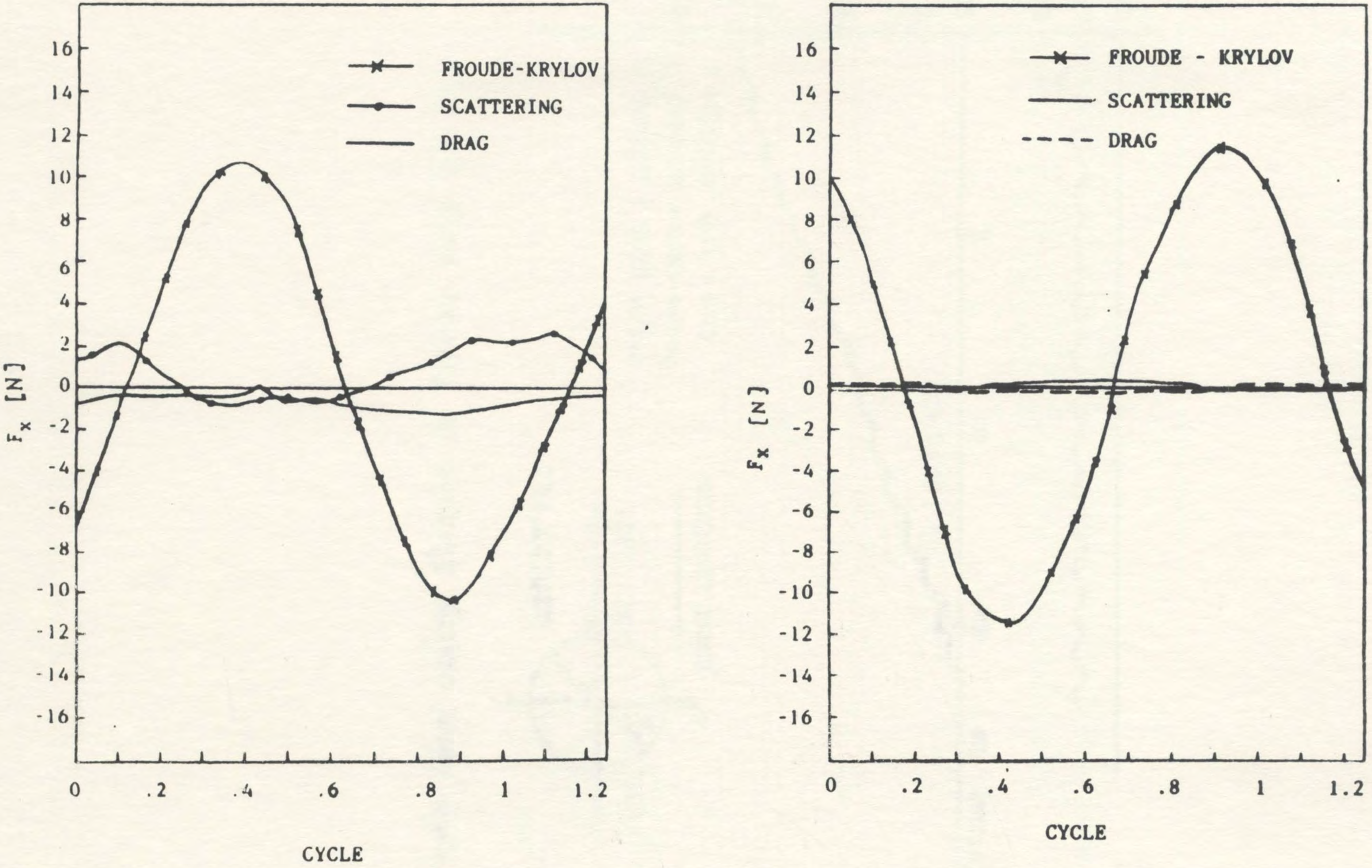

T = 0.8 sec $H/\lambda = 1/20$

T = 1.9 sec $H/\lambda = 1/30$

Figure 4.12 Time-History of the Computed Force Components in Surge Direction

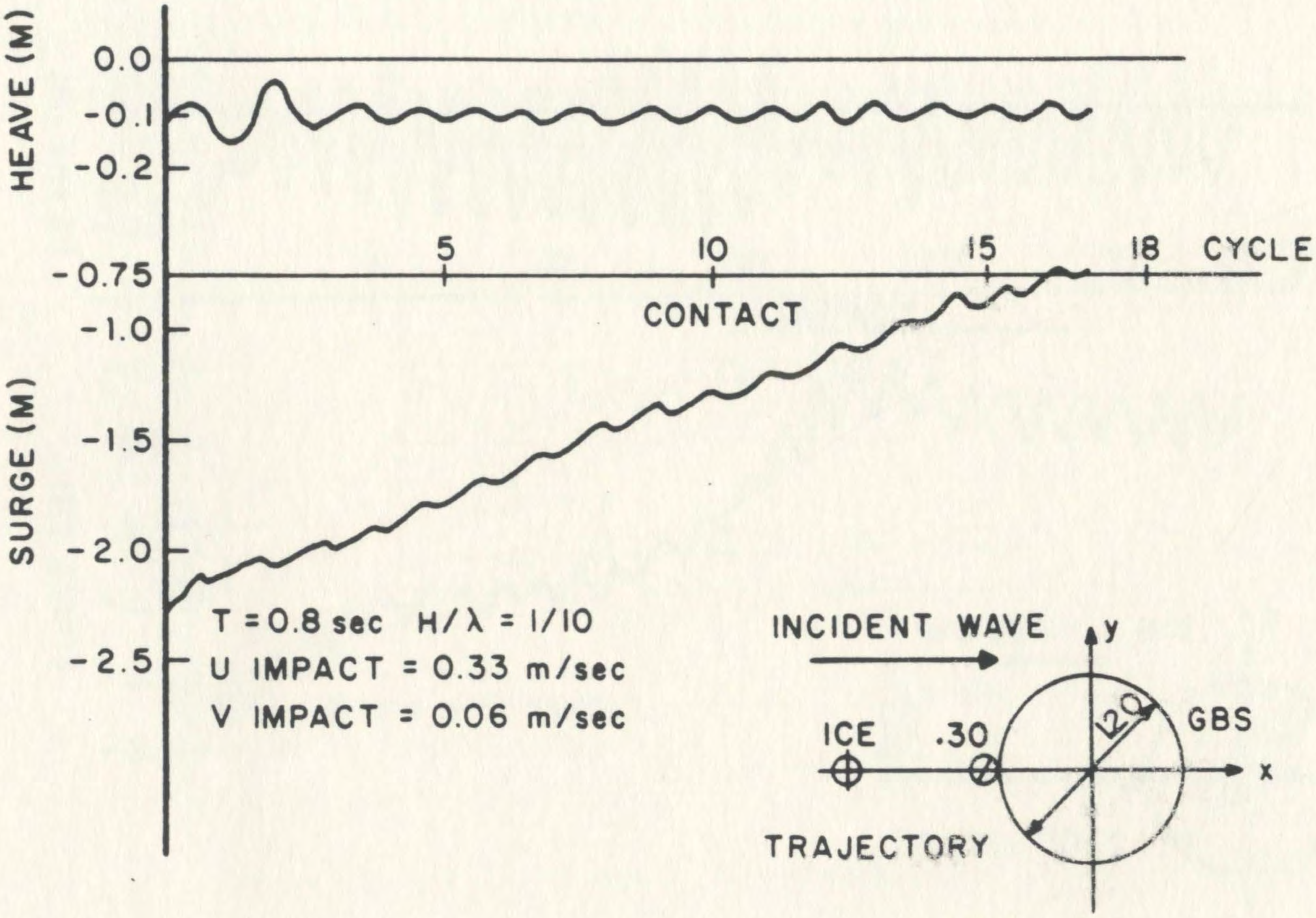

Fig. 4.13 Time-History of Iceberg Motion Near GBS.

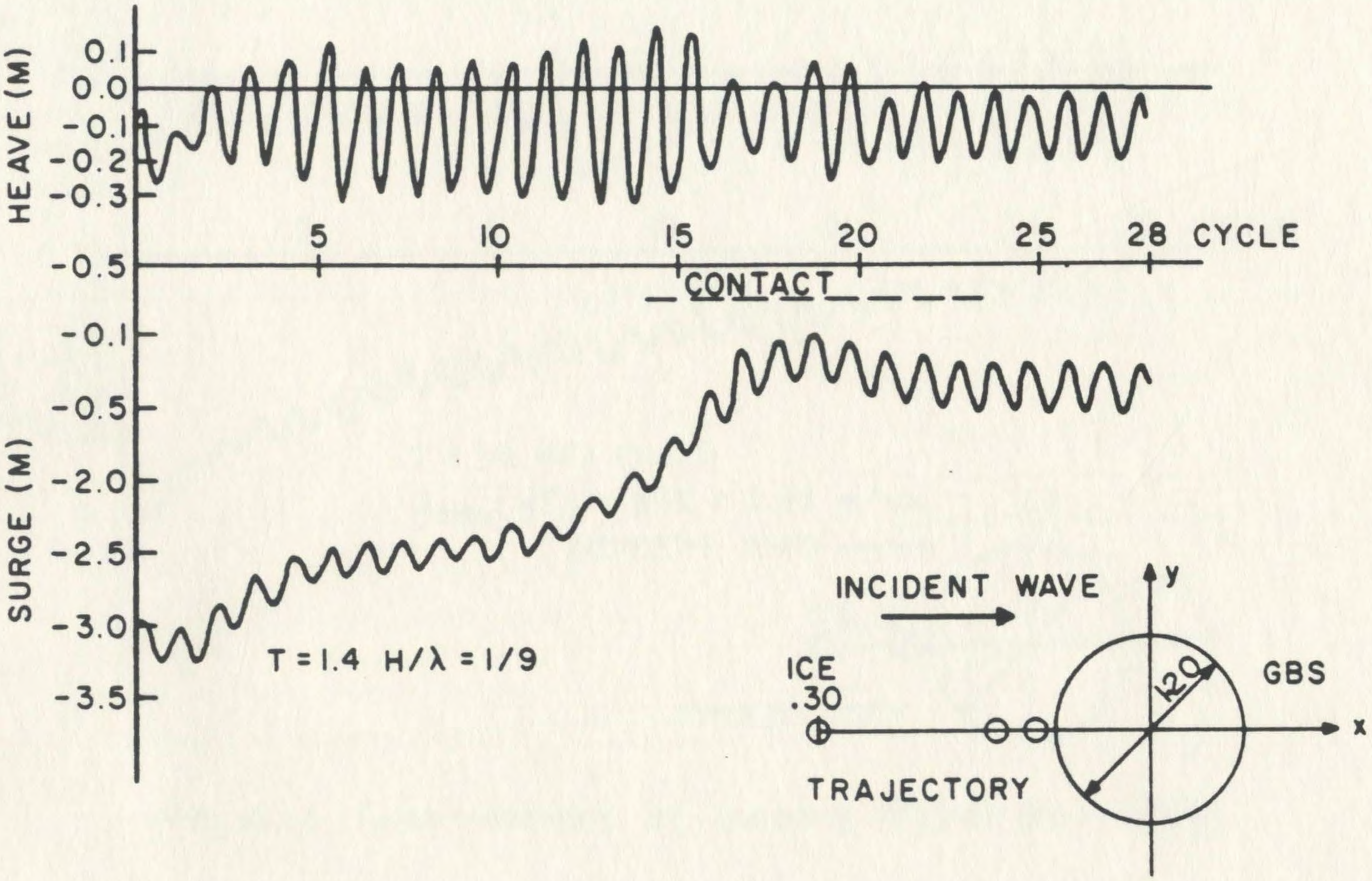

Fig. 4.14 Time-History of Iceberg Motion Near GBS.

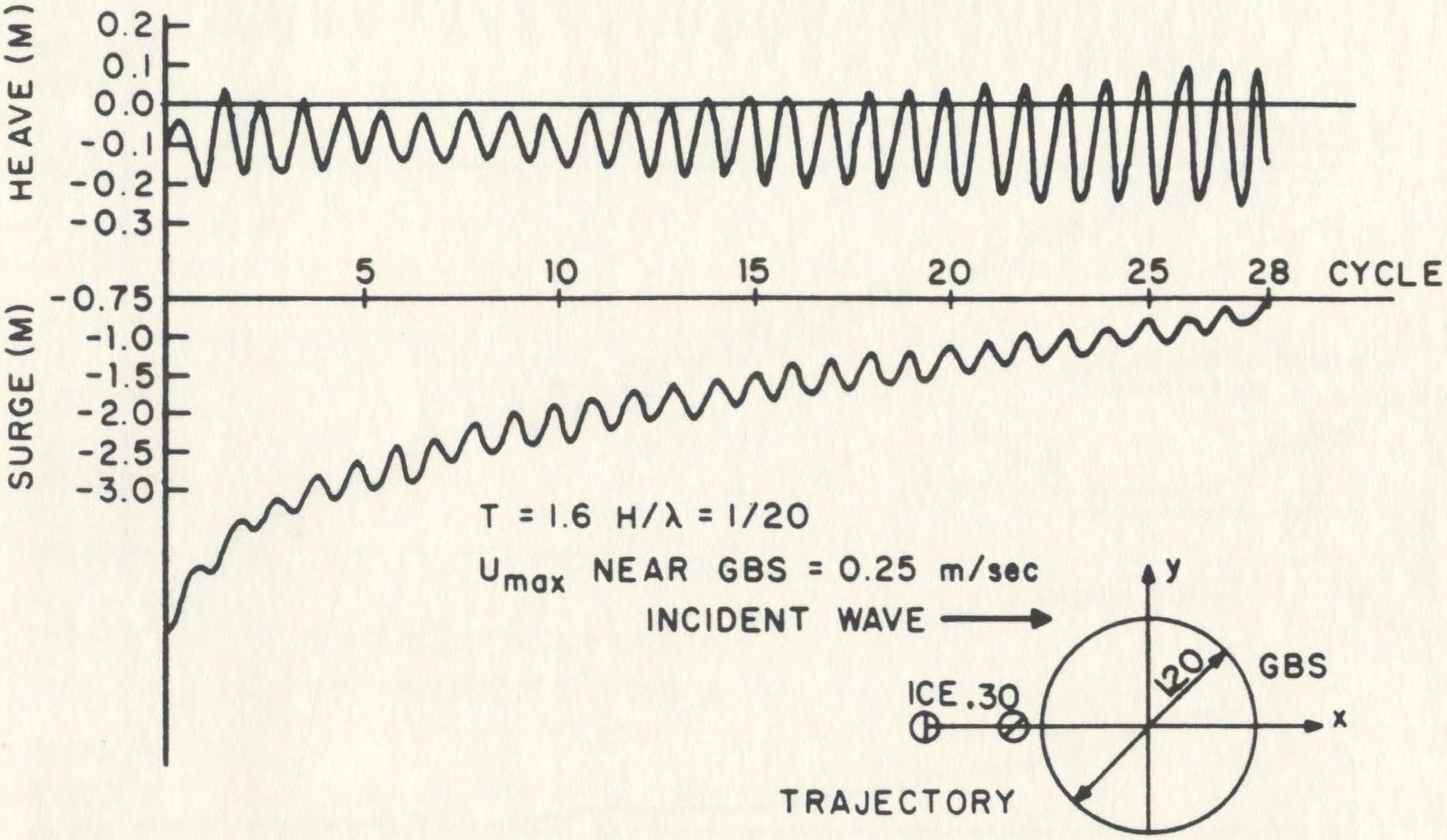

Fig. 4.15 Time-History of Iceberg Motion Near GBS.

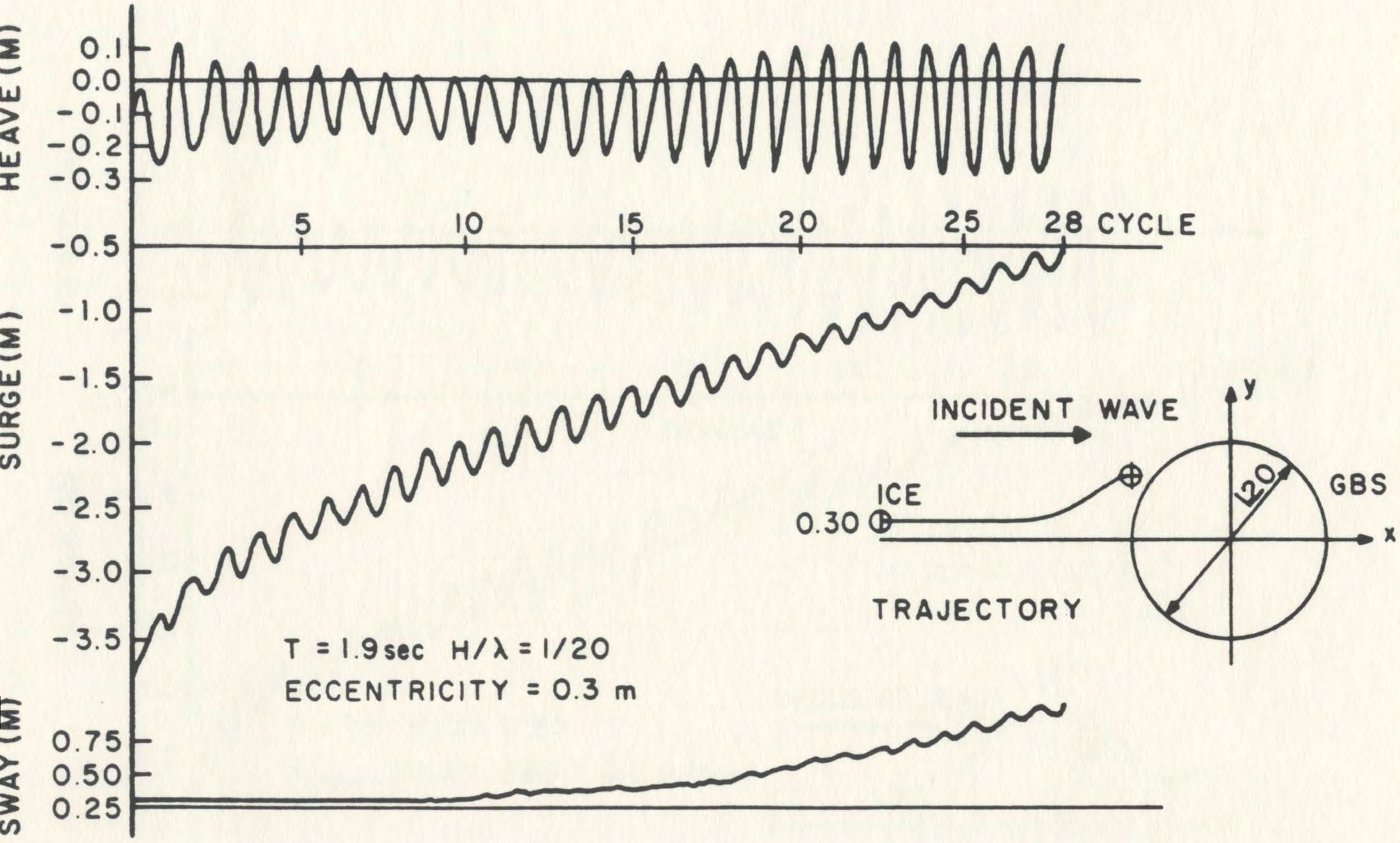

Fig. 4.16 Time-History of Iceberg Motion Near GBS.

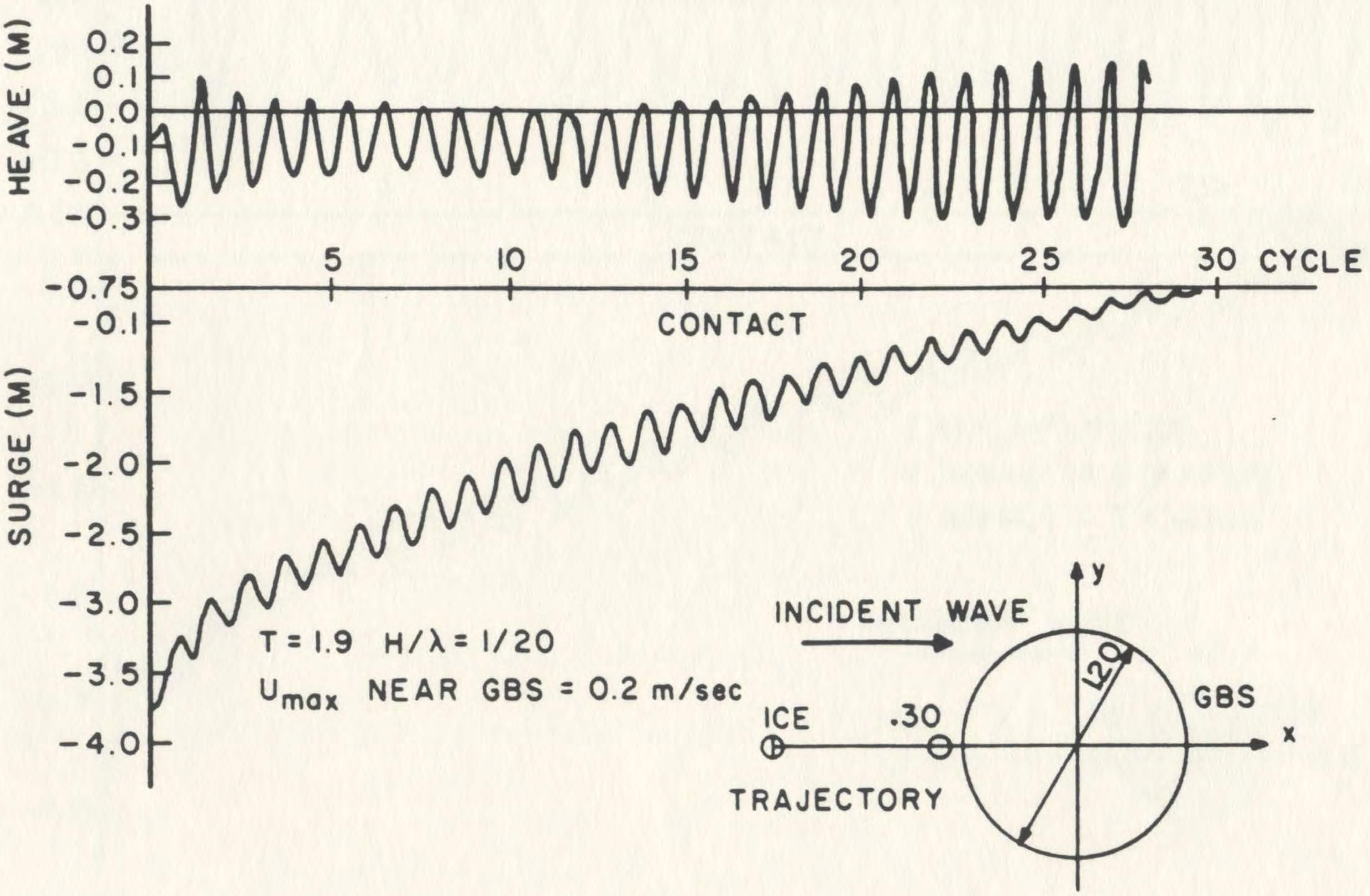

Fig. 4.17 Time-History of Iceberg Motion Near GBS.

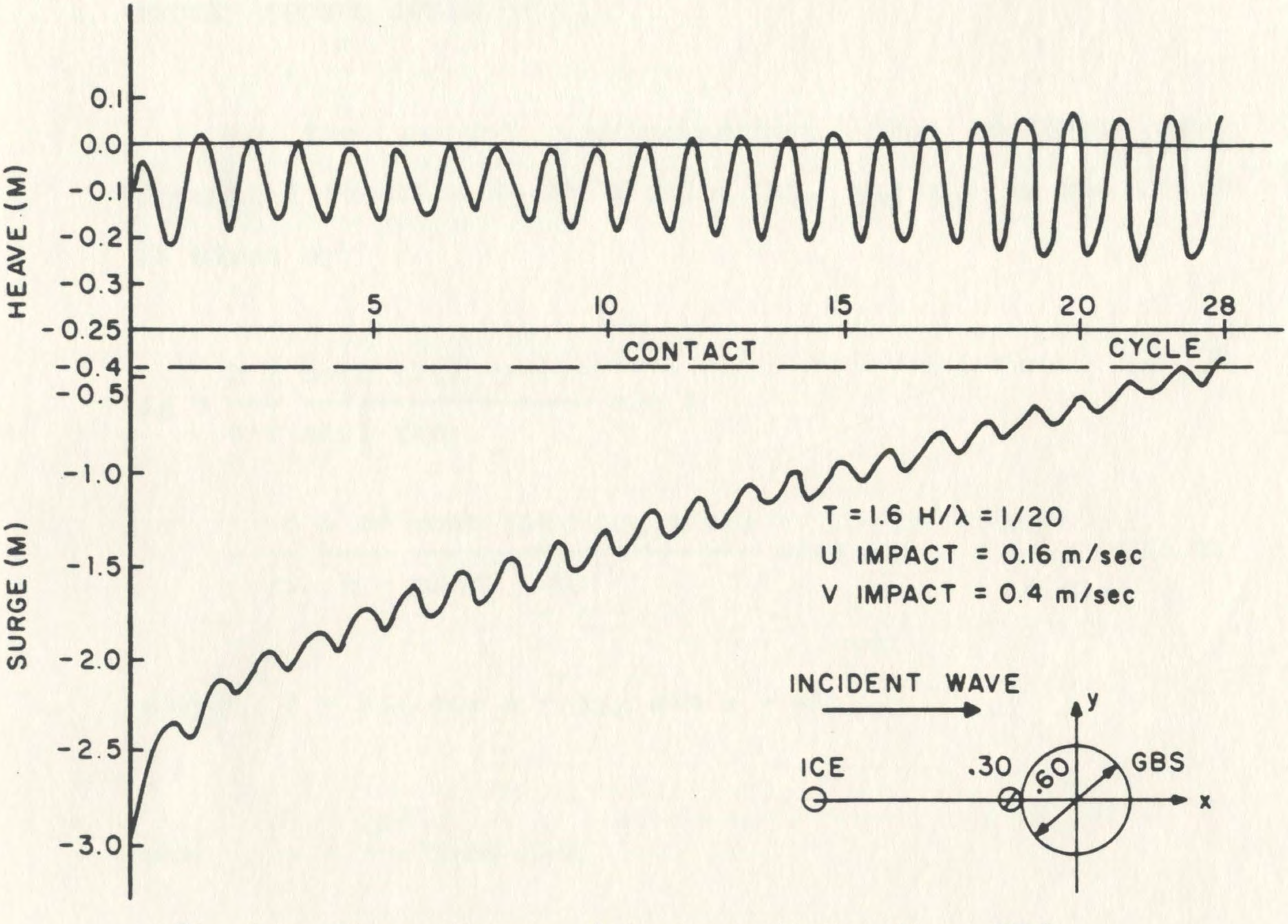

Fig. 4.18 Time-History of Iceberg Motion Near GBS.

APPENDIX A

STOKES SECOND ORDER WAVES

To the second approximation, the incident wave potential function ϕ_I at a point (x_o, y_o, z_o) in the fluid is given by:

$$\phi_I = \frac{H}{2}\frac{\lambda}{T}\frac{\cosh[k(z_o + d)]}{\sinh(kd)}\sin\theta$$

$$+ \frac{3}{16}\frac{\pi H^2}{T}\frac{\cosh[2k\ (z_o + d)]}{\sinh^4(kd)}\sin 2\theta \qquad (A.1)$$

where $\theta = kx_o \cos\alpha + ky_o \sin\alpha - \omega t$

and $\lambda = \frac{gT^2}{2\pi}\tanh(kd)$

where H, λ, T, k represent wave height, wave length, wave period and wave number, respectively. The water depth is denoted by d and α signifies the angle between the direction of propagation of the incident wave and the positive X_o axis as shown in Fig. 2.1.

The free surface η_I is expressed by

$$\eta_I = \frac{-1}{g} (\partial \phi_I / \partial t) \quad \text{at } z_o = 0 \tag{A.2}$$

$$= \frac{H}{2} \cos \theta$$

$$+ \frac{\pi H^2}{8\lambda} \frac{\cosh (kd)}{\sinh^3 (kd)} [2 + \cosh (2kd)] \cos 2\theta$$

and the subsurface pressure p_I at the point is given by:

$$p_I/\rho g = -z_o + \frac{H}{2} \frac{\cosh [k(z_o + d)]}{\cosh (kd)} \cos \theta$$

$$+ \frac{3}{8} \frac{\pi H^2}{\lambda} \frac{\tanh (kd)}{\sinh^2 (kd)} \left[\frac{\cosh [2k(z_o + d)]}{\sinh^2 (kd)} - \frac{1}{3}\right] \cos 2\theta$$

$$- \frac{1}{8} \frac{\pi H^2}{\lambda} \frac{\tanh (kd)}{\sinh^2 (kd)} \cosh [2k (z_o + d)] \tag{A.3}$$

The components of water particle velocities are given by:

$$(\partial\phi_I/\partial x_o)(1/\cos\alpha) = (\partial\phi_I/\partial y_o)(1/\sin\alpha) =$$

$$\frac{\pi H}{T}\,\frac{\cosh\,[k(z_o + d)]}{\sinh\,kd}\cos\theta$$

$$+\ \frac{3}{4}\,\frac{\pi H}{T}\,\frac{\pi H}{\lambda}\,\frac{\cosh\,[2k(z_o + d)]}{\sinh^4 kd}\cos 2\theta$$

$$(\partial\phi_I/\partial z_o) = \frac{\pi H}{T}\,\frac{\sinh\,[k(z_o + d)]}{\sinh\,(kd)}\sin\theta$$

$$+\ \frac{3}{4}\,\frac{\pi H}{T}\,\frac{\pi H}{\lambda}\,\frac{\sinh\,[2k(z_o + d)]}{\sinh^4\,(kd)}\sin\theta$$

APPENDIX B

BODY DISCRETIZATION AND NUMERICAL INTEGRATION

The method used in the numerical scheme to describe the body surface is explained and the Gauss-Legendre quadrature numerical integration technique is presented. This technique is used in the calculation of body characteristics such as surface area, volume, location of center of gravity, etc. and in the direct integration of the pressures over the submerged body surface.

B.1 BODY DISCRETIZATION

Eight-node isoparametric two-dimensional panels are used to represent the closed surface of the body. The nodal points are defined in the right hand coordinate system of axis oxyz, which will be referred to as local coordinate system. The basic procedure in the isoparametric finite element formulation is to express the element coordinates in the form of interpolations using the natural coordinate system r,s of the element (Fig. B.1).

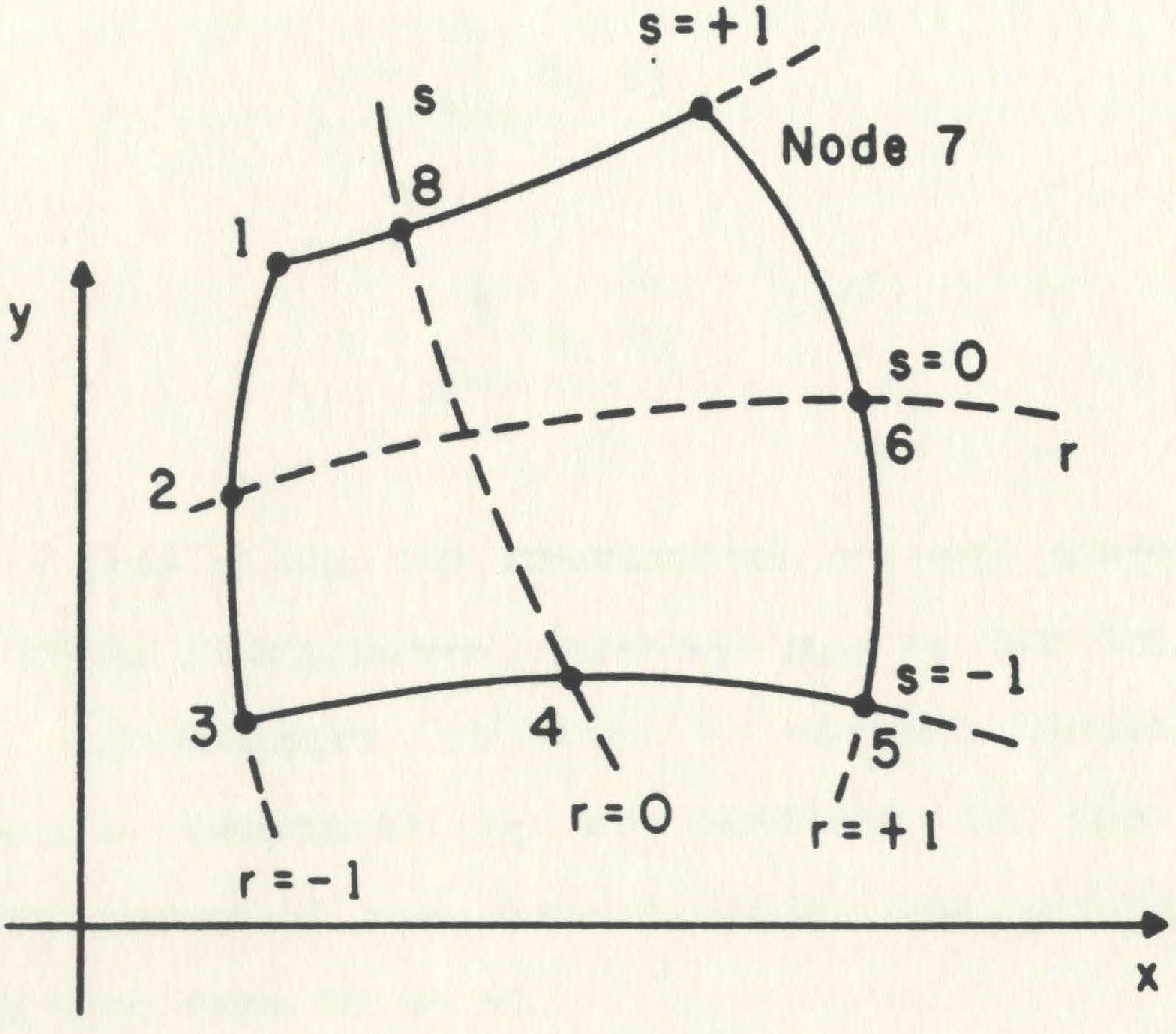

Fig. B.1. 8 variable-number-nodes two-dimensional element.

Considering a general two-dimensional element, the coordinate interpolations are:

$$x = \sum_{i=1}^{8} h_i \, x_i \quad ;$$

$$y = \sum_{i=1}^{8} h_i \, y_i \quad ;$$

$$z = \sum_{i=1}^{8} h_i \, z_i \qquad \text{(B.1.1)}$$

where x, y and z are the coordinates at any point of the element (local coordinates), and x_i, y_i, z_i for i=1,2,...,8 are the coordinates of the 8 element nodes. The interpolation functions h_i are defined in the natural coordinate system of the element, which has variables r, s that each vary from +1 to -1.

The fundamental property of the interpolation function h_i is that its value in the natural coordinate system is unity at node i and is zero at all other nodes. The interpolation functions can be expressed as:

$$\begin{aligned}
h_1 &= 0.25\ (1-r)\ (1+s) - 0.5\ h_2 - 0.5\ h_8\ ; \\
h_2 &= 0.5\ (1-s^2)\ (1-r)\ ; \\
h_3 &= 0.25\ (1-r)\ (1-s) - 0.5\ h_2 - 0.5\ h_4\ ; \\
h_4 &= 0.5\ (1-r^2)\ (1-s)\ ; \\
h_5 &= 0.25\ (1+r)\ (1-s) - 0.5\ h_4 - 0.5\ h_6\ ; \\
h_6 &= 0.5\ (1-s^2)\ (1+r)\ ; \\
h_7 &= 0.25\ (1+r)\ (1+s) - 0.5\ h_6 - 0.5\ h_8\ ; \\
h_8 &= 0.5\ (1-r^2)\ (1+s) \qquad \text{(B.1.2)}
\end{aligned}$$

where $-1 \leq (r \text{ and } s) \leq 1$ are the natural coordinates of a point within the panel.

Thus the local coordinates x, y and z of any point on the panel can be computed. However, to obtain maximum accuracy, the element should be as nearly rectangular as possible, and the intermediate side nodes should in general be located at the midpoints between the corner nodes. Considering the geometry of the two-dimensional element in Fig. (B.1), we note that by means of the coordinate interpolation in equation B.1.1, the element can have, without any difficulties, curved boundaries.

In order to calculate body characteristics and other applications, surface integrals frequently occur. Typical is the expression for evaluating the body surface area,

$$\text{Area} = \int_A |d\bar{A}| \qquad \text{(B.1.3)}$$

the element $d\bar{A}$ will generally lie on a surface where one of the coordinates (say r) is constant. The most convenient process of dealing with the above is to consider $d\bar{A}$ as a vector oriented in the direction normal to the surface. For three-dimensional problems we form a vector product.

$$d\bar{A} = \begin{Bmatrix} \partial x/\partial r \\ \partial y/\partial r \\ \partial z/\partial r \end{Bmatrix} \wedge \begin{Bmatrix} \partial x/\partial s \\ \partial y/\partial s \\ \partial z/\partial s \end{Bmatrix} \, dr\, ds \qquad \text{(B.1.4)}$$

or

$$\begin{aligned} d\bar{A} &= \{\bar{U}_r \wedge \bar{U}_s\}\, dr\, ds = \bar{U}\, dr\, ds \\ &= (u_i\, i + u_2\, j + u_3\, k)\, dr\, ds \qquad \text{(B.1.5)} \end{aligned}$$

where

$$\bar{U}_r = \begin{Bmatrix} \partial x/\partial r \\ \partial y/\partial r \\ \partial z/\partial r \end{Bmatrix} \qquad (B.1.6)$$

$$\bar{U}_s = \begin{Bmatrix} \partial x/\partial s \\ \partial y/\partial s \\ \partial z/\partial s \end{Bmatrix} \qquad (B.1.7)$$

and

$$\bar{U} = \det \begin{vmatrix} i & j & k \\ \partial x/\partial r & \partial y/\partial r & \partial z/\partial r \\ \partial x/\partial s & \partial y/\partial s & \partial z/\partial s \end{vmatrix}$$

$$\begin{aligned} &= [(\partial y/\partial r) \cdot (\partial z/\partial s) - (\partial y/\partial s) \cdot (\partial z/\partial r)]\ i \\ &- [(\partial x/\partial r) \cdot (\partial z/\partial s) - (\partial x/\partial s) \cdot (\partial z/\partial r)]\ j \\ &+ [(\partial x/\partial r) \cdot (\partial y/\partial s) - (\partial x/\partial s) \cdot (\partial y/\partial r)]\ k \qquad (B.1.8) \end{aligned}$$

with i, j and k denoting the unit vector in the direction x, y and z axes respectively, and on substitution integrate within a domain $1 \leq (r, s) \leq 1$ where:

$$\partial x/\partial r = \sum_{i=1}^{8} (\partial h_i/\partial r) \cdot x_i$$

$$\partial y/\partial r = \sum_{i=1}^{8} (\partial h_i/\partial r) \cdot y_i$$

$$\partial z/\partial r = \sum_{i=1}^{8} (\partial h_i/\partial r) \cdot z_i \qquad \text{(B.1.9)}$$

similarly,

$$\partial x/\partial s = \sum_{i=1} (\partial h_i/\partial s) \cdot x_i$$

$$\partial y/\partial s = \sum_{i=1}^{8} (\partial h_i/\partial s) \cdot y_i$$

$$\partial z/\partial s = \sum_{i=1}^{8} (\partial h_i/\partial s) \cdot z_i \qquad \text{(B.1.10)}$$

and $\partial h_i/\partial r$ for $i=1,\ldots,8$ can be expressed as:

$\partial h_1/\partial r = -0.25\ (1+s)\ - 0.5\ (\partial h_2/\partial r) - 0.5\ (\partial h_8/\partial r)$;

$\partial h_2/\partial r = -0.5\ \ (1-s^2)$;

$\partial h_3/\partial r = -0.25\ (1-s)\ - 0.5\ (\partial h_2/\partial r) - 0.5\ (\partial h_4/\partial r)$;

$\partial h_4/\partial r = -r\ (1-s)$;

$\partial h_5/\partial r = 0.25\ (1-s)\ - 0.5\ (\partial h_4/\partial r) - 0.5\ (\partial h_6/\partial r)$;

$\partial h_6/\partial r = 0.5\ \ (1-s^2)$;

$\partial h_7/\partial r = 0.25\ (1+s)\ - 0.5\ (\partial h_6/\partial r) - 0.5\ (\partial h_8/\partial r)$;

$\partial h_8/\partial r = -r\ (1+s)$ (B.1.11)

similarly

$\partial h_1/\partial s = 0.25\ (1-r)\ - 0.5\ (\partial h_2/\partial s) - 0.5\ (\partial h_8/\partial s)$;

$\partial h_2/\partial s = -s\ (1-r)$;

$\partial h_3/\partial s = -0.25\ (1-r)\ - 0.5\ (\partial h_2/\partial s) - 0.5\ (\partial h_4/\partial s)$;

$\partial h_4/\partial s = -0.5\ (1-r^2)$;

$\partial h_5/\partial s = -0.25\ (1+r)\ - 0.5\ (\partial h_4/\partial s) - 0.5\ (\partial h_6/\partial s)$;

$\partial h_6/\partial s = -s\ (1+r)$;

$\partial h_7/\partial s = 0.25\ (1+r)\ - 0.5\ (\partial h_6/\partial s) - 0.5\ (\partial h_8/\partial s)$;

$\partial h_8/\partial s = 0.5\ (1-r^2)$ (B.1.12)

Thus the surface integral (equation B.1.3) can be rewritten as:

$$\text{Area} = \int_{-1}^{1} \int_{-1}^{1} |\bar{U}\ dr\ ds| \qquad \text{(B.1.13)}$$

B.2 NUMERICAL INTEGRATION

The integral

$$I = \int_{-1}^{1} \int_{-1}^{1} f(r,s)\, dr\, ds \tag{B.2.1}$$

is evaluated using Gauss-Legendre quadrature numerical integration which states:

$$\int_{-1}^{1} f(x)\, dx = \sum_{j=1}^{n} \alpha_j\, f(aj) \tag{B.2.2}$$

where n is the number of sampling points = 3.

α_j is the integration weights

a_j is the position of sampling points (r,s)

and $\alpha_j = 0.5555556$ for $a_j = \pm .774597$

$\alpha_j = 0.8888889$ for $a_j = 0.0$

First evaluate the inner integral (equation B.2.1) keeping s constant, i.e.

$$\int_{-1}^{1} f(r,s)\ dr = \sum_{j=1}^{n} \alpha_j\, f(r_j,s) = \psi(s) \tag{B.2.3}$$

Then evaluate the outer integral in a similar manner, we get:

$$I = \int_{-1}^{1} \psi (s)\, ds = \sum_{i=1}^{n} \alpha_j \ \psi (s_i)$$

$$= \sum_{i=1}^{n} \alpha_i \sum_{j=1}^{n} \alpha_j \ f(rj, s_i)$$

$$= \sum_{i=1}^{n} \alpha_i \sum_{j=1}^{n} \alpha_i \alpha_j \ f(rj, s_i) \tag{B.2.4}$$

It is of interest to note that in fact the double summation can be readily interpreted as a single one over (n x n) points for a rectangle. When using n=3, the resulting integral is exact to the fifth order in each direction.

APPENDIX C

DIFFRACTED WAVES FROM A CYLINDRICAL STRUCTURE

An analytical solution to the linear diffraction problem is provided by MacCamy and Fuchs (1954) for an isolated vertical circular cylinder of radius a extending from the sea bottom and piercing the free surface. It is convenient to represent the solution in a cylindrical coordinate system (r, γ, z) as indicated in Fig. (C.1). The diffracted potential ϕ_d is given by:

$$\phi_d = \frac{-igH}{2\omega} \frac{\cosh[k(z + d)]}{\cosh\ (kd)} \{ \sum_{m=0}^{\infty} \beta_m B_m H_m^{(1)}(kr) \cos(m\gamma) \} e^{-i\omega t}$$

$$\text{for } r \geq a \qquad \text{(C.1)}$$

where H, ω, and k signify the wave height, wave frequency and wave number respectively and d represents the water depth and $H_m^{(1)}$ (kr) denotes the Hankel function of the first kind of order m and argument kr, with

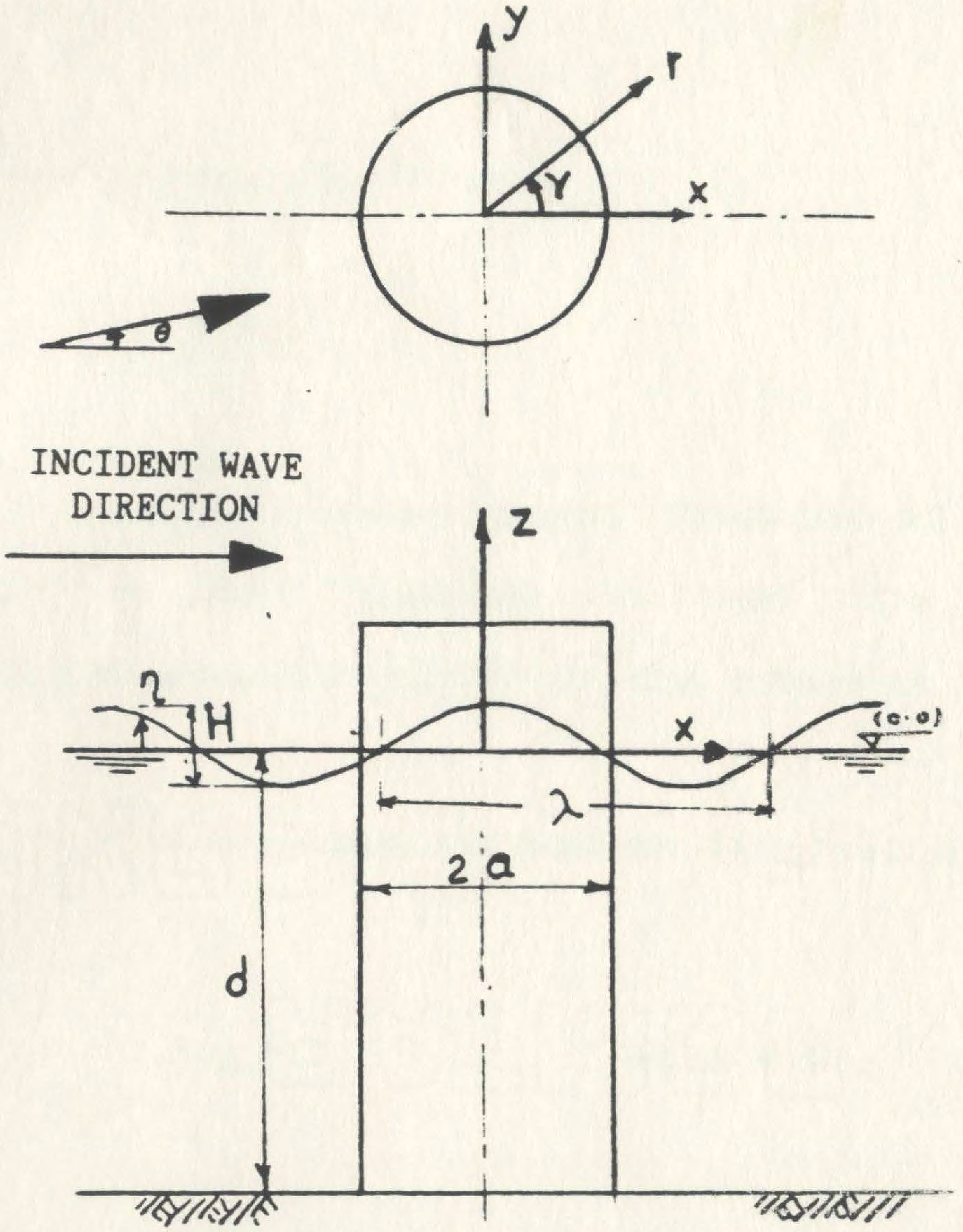

Figure C.1 Definition Sketch of Wave Diffraction Around Circular Cylinder

$\beta_m = 1$ for $m = 0$

$= 2i^m$ for $m \geq 1$

and $B_m = -J'_m(ka)/H_m^{(1)\prime}(ka)$

$i=(-1)^{1/2}$

where Jm (ka) represents Bessel function of the first kind of order m and argument ka and the prime denotes differentiation with respect to the argument.

The diffracted wave elevation is given by:

$$\eta_d = \frac{-1}{g} (\partial\phi_d/\partial t) \qquad \text{at } z = 0 \tag{C.2}$$

with $\partial\phi_d/\partial t = R\,(-i\omega\,\phi_d)$

where R denotes the real part of the complex function. Pressure due to the diffract waves p_d is given by:

$$p_d = -\rho(\partial\phi_d/\partial t) \tag{C.3}$$

The components of the water particle velocity due to the diffracted wave are:

$$\frac{\partial \phi_d}{\partial x} = R \left\{\frac{\partial \phi_d}{\partial r} \cos (\gamma - \theta) - \frac{1}{r} \frac{\partial \phi_d}{\partial \gamma} \sin(\gamma - \theta)\right\} \qquad (C.4.a)$$

$$\frac{\partial \phi_d}{\partial y} = R \left\{\frac{\partial \phi_d}{\partial r} \sin (\gamma - \theta) + \frac{\partial \phi_d}{\partial \gamma} \cos (\gamma - \theta)\right\} \qquad (C.4.b)$$

$$\frac{\partial \phi}{\partial z} = R \{\phi_d \cdot k \tanh (k (z + d))\} \qquad (C.4.c)$$

where

$$\frac{\partial \phi_d}{\partial r} = \frac{-igH}{2\omega} \frac{\cosh[k (z + d)]}{\cosh (kd)} \{ \sum_{m=0}^{\infty} \beta_m B_m k H_m^{(1)'}(kr) \cos(m\gamma)] . e^{-i\omega t}$$

$$\frac{\partial \phi_d}{\partial \gamma} = \frac{-igH}{2\omega} \frac{\cosh [k(z + d)]}{\cosh (kd)} \{ \sum_{m=0}^{\infty} \beta_m B_m k H_m^{(1)}(kr) (-m \sin m\gamma)] . e^{-i\omega t}$$